공학박사학위논문

Ion Transport Properties in Surface Films Generated on $LiNi_{0.5}Mn_{1.5}O_4$ Positive Electrode

$LiNi_{0.5}Mn_{1.5}O_4$ 양극 피막의 이온 전달 특성

2018년 2월

서울대학교 대학원

화학생물공학부

이 태 진

Ion Transport Properties in Surface Films Generated on $LiNi_{0.5}Mn_{1.5}O_4$ Positive Electrode

$LiNi_{0.5}Mn_{1.5}O_4$ 양극 피막의 이온 전달 특성

지도교수 오 승 모

이 논문을 공학박사 학위논문으로 제출함

2018년 2월

서울대학교 대학원

화학생물공학부

이 태 진

이 태 진의 박사학위논문을 인준함

2017년 12월

위 원 장 김 재 정 (인)

부위원장 오 승 모 (인)

위 원 이 규 태 (인)

위 원 문 준 영 (인)

위 원 임 태 은 (인)

ABSTRACT

Ion Transport Properties in Surface Films Generated on $LiNi_{0.5}Mn_{1.5}O_4$ Positive Electrode

Tae Jin Lee

Department of Chemical and Biological Engineering

The Graduate School

Seoul National University

A high-voltage positive electrode can increase both energy density and output, and thus commercialization is under consideration. However, the mainly used organic electrolytes at present are electrochemically decomposed in the high-voltage region (>4.3 V *vs.* Li/Li^+) to form a concomitant surface film on the positive electrodes, which cause to high resistance in the electrochemical cells. The interface of the electrode is an important key factor that determines not only the resistance itself, but also the reversibility and kinetics of the electrode. Therefore, it is important to understand the ion transport

property of the surface film and to study a strategy of overcoming a series of resistances at interfaces based on these studies.

At present, there has not been much studied on the physical properties of the positive electrode interface. On the other hand, a relatively large portion of the negative electrode interface is known about its characteristics. Therefore, in this study, it was tried to understand the characteristics of the surface film on positive electrodes, comparing with the properties for the negative electrodes. The surface film on negative electrodes, which is usually referred to “solid electrolyte interphase (SEI)”: it secures excellent passivating ability within initial cycling and transport Li^+ ion through its solid matrix to the active materials. Unlike the negative electrode surface film, however, the positive electrode interface has no excellent protecting ability and is rather permeable, so that lithium ions are not transferred through the solid phase, but delivered by the permeability of the liquid electrolyte. In addition, this permeability causes a continuous electrolyte side reaction when the positive electrodes are exposed to a high-voltage condition, because the electrolyte is easily accessible to the electrode surface due to passivating ability flaw of the surface film. It is one of the main deterioration for the high-voltage positive electrode.

Second, it was examined the some of fundamental reason for charge transfer resistance at the surface film/electrodes interfaces, and studied how to overcome this resistance. Unlike the SEI on negative electrodes, a phenomenon, in which lithium ions are not densely accumulated on the surface of the high-voltage positive electrode interface was observed. The concentration of redox species at the electrode surface is one of the factors that could determine the rate of charge transfer reaction. It is thus examined that Li^+ ion,

the redox mediator in lithium-ion batteries, whether it can also influence charge transfer reaction into electrode. It was ascertained that the lithium ion concentration on the electrode surface affects the charge transfer resistance, and the charge transfer reaction was improved by organizing a high concentrated electrolyte based on phenomenon and the permeability. A high concentration electrolyte using a low viscosity solvent improves the charge transfer resistance and improves the lithium insertion rate so that more lithium ions can be delivered from the electrolyte to the electrode active material even at high *C*-rates. It was further studied to realize this advantage in a real full-cell. It is should be significantly considered to select the counter electrode, which must show fast delithiation property. Considering this point, after positive and negative electrodes, a high-power property is also realized in a full-cell.

Keywords: Lithium-ion batteries, Solid electrolyte interphase (SEI), Solid Permeable Interface (SPI), Ion transport, Highly concentrated electrolyte, Ionic conductivity, Charge transfer

Student Number: 2014-30295

CONTENTS

LIST OF FIGURES

Figure 21. EQCM measurements and ac impedance spectra. EQCM results: (a); mass increase of SEI generated on the Cu-quartz electrode via linear sweep voltammetry to 0.005 V, (b) mass increase of films generated on the Pt-quartz electrode via linear sweep voltammetry to 5.2 V, reference and counter electrode; Li metal, scan rate = 1.0 mV s^{-1}. (c) (d); ac impedance spectra obtained from the Li/Li/Cu or Pt three electrode cells after one linear sweep at 1 mV s^{-1}. (c); the magnified spectra of (d).

Figure 22. The Li 1s depth-profiling XPS spectra obtained from the SEI-deposited graphite and the SPI-deposited LNMO electrodes. The samples were washed with DEC except for (c). (a) (b); graphite electrodes after the 1^{st} charging (0.005 V) and discharging (2.0 V), (c); LNMO electrode without washing after the 1^{st} charging, (d) (e); LNMO electrodes after the 1^{st} charging (4.9 V) and discharging (3.5 V), (f); LNMO electrode after the 200^{th} charging. The etching time (0 s and 300 s) is indicated in the inset.

Figure 23. Electrochemical charging situation for generating the two surface films on both negative and positive electrodes.

Figure 24. C 1s (a, b), O 1s (c, d), F 1s (e, f), and P 2p (g, h) depth-profiling XPS spectra obtained from the SEI-deposited-graphite (0.005 V) and SPI-deposited-LNMO (4.9 V) electrodes. All samples were washed with DEC after being charged once. The etching time is indicated in each panel. The spectra were fitted using the binding energy values listed in Table 7.[63,94-101]

Figure 25. Electrochemical reduction and oxidation mechanisms of carbonates. (a); electrochemical reduction of carbonate, (b); electrochemical oxidation of carbonate.

Figure 26. Diagrams of solid structures for the two surface films. (a); SEI on graphite electrode, (b); solid film on LNMO electrode.

Figure 27. The galvanostatic charging/discharging voltage profiles for LNMO electrode. The cycles are indicated in the inset.

Figure 28. TOF-SIMS depth profiles for the surface film derived from the film-generating electrolyte (1.3 *M* $LiPF_6$ in EC:EMC:DEC = 3:2:5 (*v/v/v*)) on LNMO electrode by wetting the film-wetting electrolyte (1.3 *M* $LiClO_4$ in EC-D_4:DEC =3:7 (*v/v*)). (a); Mn^+ of LNMO electrode and PF_6^- from the film-forming electrolyte, and (b); $^6Li^+$ ions and solvent (EC-D_4) from the wetting electrolyte. All intensities are for the final re-wetted LNMO electrode except for the washed one (green inverse triangle in (b)) by DEC.

Figure 29. Cyclic voltammograms obtained from 0.01 *M* nickel(II)-1,4,8,11-tetraazacyclotetradecane tetrafluoroborate (Ni(cyclam)$[BF_4]_2$, Ni(II)-cy) dissolved in 1.3 *M* $LiPF_6$ in 3:2:5 (*v/v/v*) EC:EMC:DEC at a scan rate of 50 mV s^{-1} in a three-electrode cell (counter and reference electrodes are Li metal) on the following electrodes: (a) glassy carbon, (b) graphite, and (c) LNMO. The structure of Ni(II)-cy is shown in panel (a).

Figure 30. Schematic drawing for accessibility of the Ni(Ⅱ)-cy redox probe in the two surface films: (a) SEI and (b) SPI.

Figure 31. Coulombic efficiency of active materials and films growth of LNMO

electrode. (a) Coulombic efficiency of graphite, LCO, and LNMO electrodes at 25℃. (b) (c) (d) (f); films growth of the LNMO electrodes during cycling at 25℃. The cycle numbers are in the inset.

Figure 32. Ac impedance spectra and their fitting results for the SEI and SPI obtained as a function of $LiPF_6$ concentration in the electrolyte solution. (a), (c), and (e); Nyquist plots for SEI on graphite electrodes, (b), (d), and (f); Nyquist plots for SPI on LNMO electrodes. (g); Ionic conductivities of the electrolyte solutions as a function of $LiPF_6$ concentration in EC:DMC = 5:5 (*v/v*). (h); The film resistances for SEI and SPI as a function of $LiPF_6$ concentration in EC:DMC = 5:5 (*v/v*).

Figure 33. The $^6Li^+$ intensities for the two surface films. The SPI is generated on LNMO electrode to 4.9 V, and the SEI is formed on graphite electrode to 0.005 V by galvanostatic charging.

Figure 34. TOF-SIMS depth-profiling data for $^6Li^+$ ions in the SEI on a Cu electrode, and the SPI on a Pt electrode.

Figure 35. Diagram of energy barrier for charge transfer reaction into LNMO electrodes.

Figure 36. The ac impedance spectra for the SPI-generated LNMO electrode with $LiPF_6$ concentrations. After charging to 4.9 V and discharging to SOC 50 (QOCV 4.71 V), the SPI-deposited LNMO electrodes washed with DEC and followed to be re-assembled with various $LiPF_6$ concentrations in EC:DMC = 5:5 (*v/v*). The wetted electrolytes are 1.0 *M*; (a), low concentration; (b), high concentration; (c), and the fitted charge transfer

5:5 (*v/v*)), (b); 1.0 M LiPF6 in DMC, and (c); the highly concentrated electrolyte (2.5 *M* $LiPF_6$ in DMC). Electrodes were completely Li^+-extracted before testing lithiation rates.

Figure 44. Rate performances of LNMO electrode for the 1.0 *M* $LiPF_6$ in EC:DMC = 5:5 (*v/v*)), 1.0 *M* $LiPF_6$ in DMC, and the highly concentrated electrolyte (2.5 *M* $LiPF_6$ in DMC). All Li^+ ions are extracted before testing lithiation rates.

Figure 45. Arrhenius plots for LNMO electrode (LNMO/LNMO symmetric cell) derived from the fitted charge transfer resistances of Ac impedances with temperatures. The correlation between the log scale of the reciprocal charge transfer resistances and the inverse form of temperature are estimated by a linear equation. The used electrolytes, and their corresponding activation energies are indicated in the inset.

Figure 46. Nyquist plot (ac impedance) for symmetric LTO/LTO electrodes cells, assembled with a conventional electrolyte (1.0 *M* $LiPF_6$ in EC:DMC = 5:5 (*v/v*)), 1.0 *M* $LiPF_6$ in DMC, and the highly concentrated electrolyte (2.5 *M* $LiPF_6$ in DMC). The LTO electrodes were charged to SOC 10 (QOCV; 1.56 V). Each equivalent circuit is indicated in the inset.

Figure 47. The galvanostatic lithiation voltage profiles for LTO electrodes with electrolytes compositions. (a); a conventional composition (1.0 *M* $LiPF_6$ in EC:DMC = 5:5 (*v/v*)), (b); 1.0 *M* $LiPF_6$ in DMC, and (c); the highly concentrated electrolyte (2.5 *M* $LiPF_6$ in DMC). Electrodes were completely Li^+-extracted before testing lithiation rates.

Figure 48. Rate performances of LTO electrode for the 1.0 *M* $LiPF_6$ in EC:DMC = 5:5 (*v/v*)), 1.0 *M* $LiPF_6$ in DMC, and the highly concentrated electrolyte (2.5 *M* $LiPF_6$ in DMC). All Li^+ ions are extracted before testing lithiation rates.

Figure 49. Diagram of the usual 1.0 *M* of composition and a highly concentrated electrolyte.

Figure 50. Arrhenius plots for LTO electrode (LTO/LTO symmetric cell) derived from the fitted charge transfer resistances of Ac impedances with temperatures. The correlation between the log scale of the reciprocal charge transfer resistances and the inverse form of temperature are estimated by a linear equation. The used electrolytes, and their corresponding activation energies are indicated in the inset.

Figure 51. The galvanostatic delithiation voltage profiles for Li/LNMO and Li/LTO cells with electrolytes compositions. (a) (b); a conventional composition (1.0 *M* $LiPF_6$ in EC:DMC = 5:5 (*v/v*)), (c) (d); 1.0 *M* $LiPF_6$ in DMC, and (e) (f); the highly concentrated electrolyte (2.5 *M* $LiPF_6$ in DMC). Electrodes were completely Li^+-inserted before testing delithiation rates. The left data are for the Li/LNMO cells and the right one are for the Li/LTO cells.

Figure 52. Rate performances of Li/LNMO and Li/LTO cells for the 1.0 *M* $LiPF_6$ in EC:DMC = 5:5 (*v/v*)), 1.0 *M* $LiPF_6$ in DMC, and the highly concentrated electrolyte (2.5 *M* $LiPF_6$ in DMC). All Li^+ ions are inserted before testing delithiation rates. (a); Li/LNMO cells, (b); Li/LTO cells.

Figure 53. The charging and discharging voltage profiles and its resulting rate

performances for LTO/LNMO full-cells with 1.0 *M* $LiPF_6$ in EC:DMC = 5:5 (*v/v*) and 2.5 *M* $LiPF_6$ in DMC. Before testing rate performances, SOC of each full-cell was controlled to 0 (a, b) or 100 (c, d).

LIST OF TABLES

1. INTRODUCTION

At present, lithium-ion batteries (LIBs) begin to be applied to electric vehicles (EVs) and energy storage system going beyond small electronic devices, and has thus attracted much attention. For these applications, much improved cell, which have high energy density and power, need to be developed. Energy density is defined as the integral form of capacity multiplying voltage: $E = \int Q \times V$,[1] and power is expressed in voltage times currents: $P = V \times I$. A high-voltage positive electrode should thus be employed in a commercial LIBs, which is due that voltage is significantly correlated with energy density and high-power properties. Among these materials, the Ni-doped manganese spinel ($LiNi_{0.5}Mn_{1.5}O_4$, hereafter LNMO) has a much higher working voltage (>4.6 V *vs.* Li/Li^+) than the commercially available positive electrodes (for example, 4.0 V for $LiCoO_2$ and $LiMn_2O_4$).[2-6] The advantageous high-voltage characteristic, however, confronts the LNMO electrode to be in an abuse condition, when the high-voltage positive electrode is applied in electrochemical cells in practical.

Electrolytes play a role in lithium ion transport channel between the negative and positive electrodes in lithium-ion batteries (LIBs), and thus they are always exposed to chaotic electron transfer near at electrode surface. The electrochemical stability windows of the commonly used carbonates-based electrolytes are between 1.0 and 4.3 V.[1,7] The LNMO electrodes reversibly react over 4.6 V, and thus the electrolytes are oxidatively decomposed to cause the concomitant film deposition on the LNMO electrodes.[8,9]

According to previous reports, film evolves on positive electrodes from various routes as well as electrochemical oxidation. In detail, when positive electrodes are exposed to highly oxidative condition, electrolytes are electrochemically oxidized to form a polymeric species.[8,9] Moreover, semicarbonates are generated by nucleophilic attack of reactive oxides or oxygen evolved from metal oxide surface,[10-12] and LiF is deposited by degradation of lithium salt or HF attack against lithated metal oxides.[12-15] Also, Li^+ ion-solvating solvents are adsorbed on positive electrodes even without electron transfer.[16,17] Whatever path produces films on positive electrodes, the interphase also participates in migration path of Li^+ ions as well as electrolytes ionic conductor to determine kinetics for positive electrodes.[18] Up to date, there are still questions whether films on positive electrodes indeed show high passivation ability and same Li^+ ion transport behavior such as solid electrolyte interphase (SEI) evolved on negative electrodes.

The surface film properties on negative electrodes were relatively more unveiled than that on positive electrodes. For negative electrodes, for example graphite electrodes, their working voltage (< 0.25 V *vs.* Li/Li^+) is below electrochemical stability windows of the commonly used carbonate-based electrolytes (< 1.0 V),[7,19-21] which is electrochemically reduced to form a film on the graphite electrode. Such films are electronically insulating and passivating for electrolytes to be segregated from negative electrodes to prevent further decomposition of electrolytes. Nevertheless, the interphase carries Li^+ ions through its solid phase not to induce a concentration polarization of Li^+ ions between electrolytes and negative electrodes. Due to this behavior, this interphase

was named for solid electrolyte interphase (SEI) by E. Peled.[22,23] This model suggests that all SEI components are deposited in a mosaic type structure, in which the carbonates solvents-derived inorganic components such as Li_2CO_3 and Li_2O are densely packed to just above on the graphite or Li metal electrodes. In detail, SEI consists of the outer organic layer and the inner inorganic layer,[24,25] in which electrolytes diffuse in pore region of organic layer (porous layer) and are limited to pass into the inorganic compact layer.[26] When electrolytes arrive at this compact layer, only Li^+ ions conduct in the lattice Li^+ sites of inorganic components like Li_2CO_3 by a knock-off mechanism.[27]

In order to comprehend Li^+ ion transport behavior of films on positive electrodes, it was compared to that of SEI on negative electrodes in this study. This comparative study was previously tried by Kristina Edström and her colleagues.[28,29] In detail, they observed through X-ray photoelectron spectroscopy (XPS) that the surface film on positive electrodes grows continually at high temperature, while SEI on graphite negative electrodes first had been broke down and followed repairing processes in some abuse condition. Based on this observation, they referred the term, solid permeable interface (SPI) in their reports. In this study, it was examined whether the surface film on LNMO electrodes is indeed passivating and solid conduction in its own matrix as same as SEI on graphite electrodes. First, the film components are quite different for the SEI on graphite electrodes and the film on LNMO electrodes. XPS displays that the upper organic components (e.g, lithium alkyl carbonate, $ROCO_2Li$) and the bottom inorganic components such as lithium fluoride (LiF), lithium carbonates (Li_2CO_3), and lithium oxide (Li_2O) are grown on graphite electrode thickly enough to discourage

electron tunneling. In contrast, thin organic layers are generated on LNMO electrode. This is similar with the upper porous organic layer in SEI. This raises suspicion whether the surface film on LNMO electrode is passivating as SEI. In was observed that Li^+ ions with solvated state by ethylene carbonate (EC) are immersed into this organic layer and easily accessible just above the top of LNMO surface. Unlike SEI, the surface film on positive electrodes are poorly passivating and allow to approach of electrolyte molecules. That is to say, film on positive electrodes is permeable, and thus the term, SPI, was also adopted in this work. After all, Li^+ transport is influenced by this film permeability. It was ascertained that ionic conductivity of electrolytes could lead to change that of the surface film on LNMO electrode even for the same solid components, while it does not cause that of SEI to change once SEI is formed on graphite electrode.

Second, another feature was observed for the two surface films. For SEI, high population of Li^+-involved species ($ROCO_2Li$, LiF, Li_2CO_3, Li_2O) are embedded, while salt anion-contained organic components are deposited and Li^+-ions are easily leached out in the SPI. It was thus suspected that less population of Li^+ ions in SPI than SEI could lead to poor ionic conductivity per unit thickness. This was confirmed by ac impedance measurement. The SPI shows larger film and charge transfer resistances than SEI. Based on the film permeability and less Li^+ ion concentrations in the SPI, a highly concentrated electrolyte was introduced, if it can improve a series of these interface resistances for LNMO electrodes. Usually in cyclic and linear carbonates with 5:5 or 3:7 (*v/v*), when lithium salt concentration is over at 1.0 ~ 1.3 *M*, viscosity of the corresponding composition increases and the resulting ionic conductivity becomes to low. Such a

viscosity problem could be mitigated by adding more less-viscous linear carbonates at the expense of more viscous cyclic carbonates without significantly losing ionic conductivity. The optimized composition was 2.5 *M* of lithium hexafluorophosphate ($LiPF_6$) in dimethyl carbonate (DMC). Even though DMC solvent has much lower dielectric constant than EC, DMC could provide larger Li^+ ion concentrations with involving all free Li^+ ion, ion pair, and aggregates over triple ion than the usual 1.0 *M* of composition. Additionally, the less coordinating toward to Li^+ ion of DMC than EC, which also helps desolvation process from electrolytes into electrodes. Due to more Li^+ ions, charge transfer resistances decrease to lead to fast lithiation of LNMO electrode even at 20 *C* of rate. The ultimate purpose of this work is to understand Li^+ ion transport behavior and the concomitant factors for a series of interface resistances to improve positive electrodes kinetics.

2. BACKGROUND

2.1. Basic electrochemistry

2.1.1. Ionic conductivity

Ionic conductivity (κ) is defined as current density (I) per electric field (E) between the two symmetric electrodes, in which all free ions participate in ion conduction, and thus ionic conductivity is determined by total sum of contributions for the each ion conductivity.[30,31]

$$\kappa \equiv \frac{\mathrm{I}}{\mathrm{E}} = \frac{\mathrm{i/A}}{\mathrm{V/l}} = \frac{1}{\mathrm{R}} \cdot \frac{\mathrm{l}}{\mathrm{A}} = \sum_{\mathrm{j}} |\mathrm{z_j}| \mathrm{F C_j u_j}$$

,where z_j: ion charge, F: Faraday constant, C_j: free ion concentration, u_j: ion mobility. In the equation, $\frac{l}{A}$, usually referred by cell parameter, which is determined experimentally by standard solution such as KCl having the reported ionic conductivity. Specially, free ion concentration and ion mobility are major determining factors for the ionic conductivity.

Generally, in the low salt concentrated regions, as salt concentration increases, the resulting free ion concentration increases to ionic conductivity increases. After that, a maximum point appears at a

concentration point, the ionic conductivity decreases as salt is concentrated (Fig. 1). This can be explained by relaxation effect and electrophoretic effect. When salt is highly concentrated, if electric field is applied to the electrochemical cell, positive ion and negative ion migrate toward to opposite direction, in which neighbor positive/negative ion complexes generate opposite electric filed to hinder migration of each ion. This is “relaxation effect”. In addition, when salt is concentrated highly, viscosity of electrolyte solution increases, and thus ions suffer from frictional drag force by $u_i = \frac{|z_i|e}{6\pi\eta r}$ (η; viscosity, r; ion radius). This is referred to “electrophoretic effect”.

In LIBs, high dielectric solvent such as cyclic carbonates is employed to increase free ion, which contributes ionic conductivity. Usually, this high dielectric solvent also show high viscosity. In order to mitigate this viscosity upsurge, less viscous linear carbonates are also added in the solution.

2.1.2. Solvation states in low dissociable solution medium

When the dielectric constant of the nonaqueous solvent goes below about 15, ions can associate not only in ion pairs but also in ion triplets. We call the ion, which are fully solvated by solvent and completely

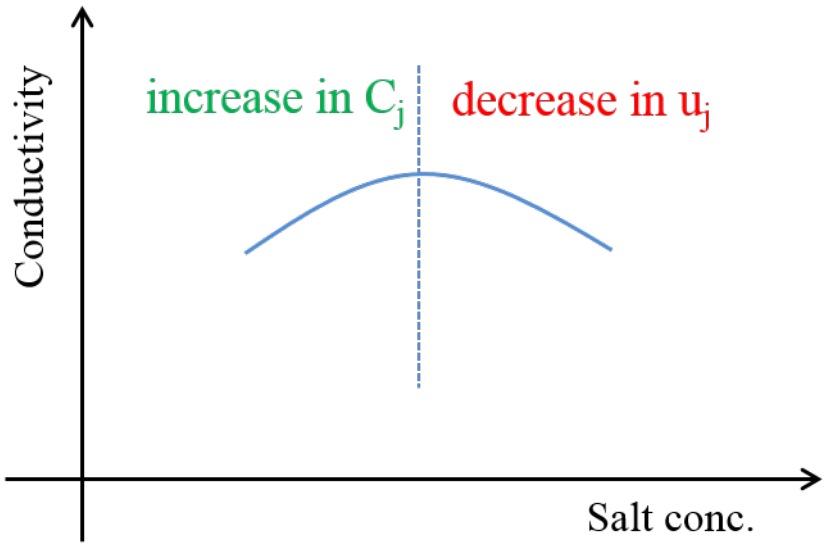

Figure 1. Ionic conductivity changes with salt concentrations in electrolyte solution.

spaced with the opposite ion, to “free ion”. Based on anion, interacting positive and negative ions with one to one ratio, which is called to “ion pair”. Interactions between cations and anions with 2:1 ratio, which is referred “triple ion”, and the further coordination is named to “aggregates”.[32,33]

Free ion; A^-

Ion pair; $\mathrm{B}^+ \cdots A^-$

Ion triplet (aggregate); $\mathrm{B}^+ \cdots A^- \cdots \mathrm{B}^+$

They all exist in an equilibrium state: $\mathrm{B}^+ + A^- \rightleftharpoons \mathrm{B}^+ \cdots A^- \rightleftharpoons \mathrm{B}^+ \cdots A^- \cdots \mathrm{B}^+$. Raman spectroscopy is available to ascertain their existence in a solution medium.

Ionic conductivity is also defined by the equation.by Debye-H*ü*ckel-Onsager equation.[32] A low dielectric constant-owned solution does not

Debye-H*ü*ckel-Onsager equation: $\Lambda = \Lambda^0 - (\mathrm{A} + \mathrm{B}\Lambda^0)\sqrt{\mathrm{C}}$

$\mathrm{A} \propto \frac{1}{\varepsilon^{1/2}} \quad \mathrm{B} \propto \frac{1}{\varepsilon^{3/2}}$

$\kappa = \mathrm{C}\Lambda$ (Λ; molar conductivity, C; total concentration)

dissociate positive and negative ions well, and thus the concomitant molar conductivity is much lower than a high dielectric constant-owned solution medium. As a result, a low dissociable solution media show

their maximum ionic conductivity at much higher concentration than a high dissociable solution, as absolute free ion concentration significantly increase.

2.1.3. Electrochemical charge transfer kinetics

If charge transfer process is rate-determining step for an electrochemical reaction, the forward and reverse reaction rates are expressed as the following equations.[30,31] Therefore, concentration of surface reactant influences current densities for the electrochemical reaction.

$$O + ne^- \rightleftharpoons R$$

$$v_f = k_f C_O(o,t) = \frac{i_c}{nFA},\ v_b = k_b C_R(o,t) = \frac{i_a}{nFA},\ \text{(where x=0; from electrode)}$$

$$i_{net} = nFA[k_f C_O(o,t) - k_b C_R(o,t)]$$

2.1.4. Cyclic voltammetry

The currents are measured by changing voltages at a constant rate: $E = E_i - vt$, where v is scan rate. The applied voltage is changed with time, and thus surface reactant concentration, $C_O(o,t)$, decreases with time

and the diffusion layer expands to the bulk of electrolytes by $l = \sqrt{2D_O t}$ of rate. Therefore, the concentration slope gradually increase at initial scanned time, the maximum slope occurs and re-decrease with time. As a result, peak current appear at the maximum slope and it re-decrease by depletion of surface reactant. The peak current i_p is proportional to $v^{1/2}$,[30,31] which is diffusion control and analogous to the variation of i_d with $t^{-1/2}$ in chronoamperometry. During negative potential sweep, the evolved R diffuses toward to the bulk electrolyte, and thus the reverse anodic current is a little lower than the forward cathodic current. This becomes more significant as the potential sweep becomes slower, which is due that the R species diffuse out more with time. The typical cyclic voltammogram is shown in Fig. 2.[34]

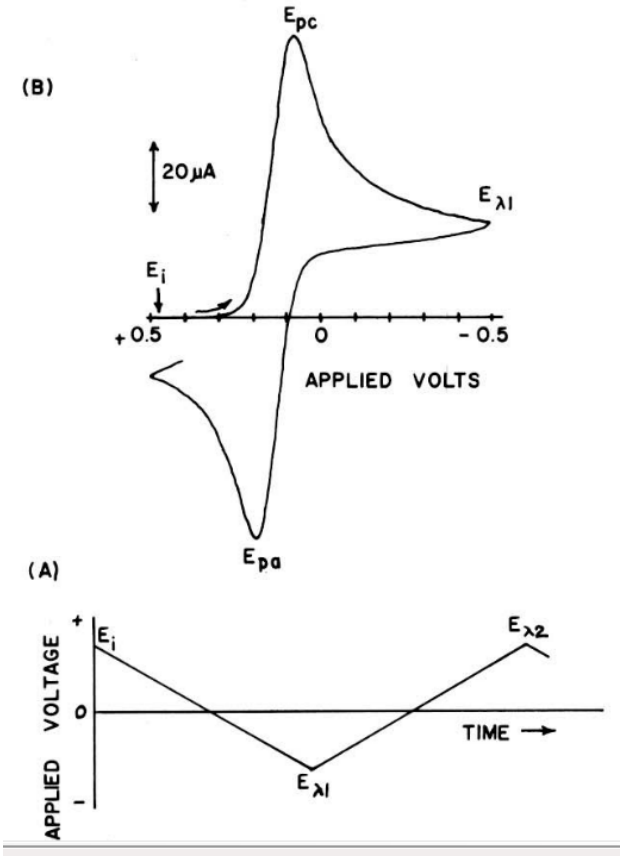

Figure 2. A typical Nernstian cyclic voltammogram.[34]

2.2. Electrolytes: Aprotic liquid organic electrolytes

2.2.1. Li salts

The dissociation tendency becomes larger, as electrons are delocalized, and thus a larger diameter of anion is preferred. Generally, the dissociation increases by the following order.[35-37]

$LiN(SO_2CF_3)_2 > LiAsF_6 > LiPF_6 > LiClO_4 > LiBF_4 > LiCF_3SO_3$

However, anion mobility decrease, as anion radius increase by the Stoke's law: $\mu = \frac{ze}{6\pi\eta r}$. An appropriate radius of anion needs to be employed to guarantee a high ionic conductivity. Resultantly, the average ionic conductivity order is are followings.[35-37]

$LiPF_6 > LiClO_4 > LiN(SO_2CF_3)_2 > LiN(SO_2C_2F_5)_2 > LiBF_4 > LiSO_3CF_3$

The features for each Li salt are summarized as follows.

(1) $LiClO_4$: The Cl^- atom makes the anion a strong oxidant to cause explosion.[38]

(2) $LiAsF_6$: As (Ⅴ) is not toxic, however, the electro-reduced forms of As (Ⅲ) or As (0) states are highly toxic.

(3) $LiPF_6$: The P-F bond is labile, and the salt thus readily undergoes hydrolysis to generate acid such as HF or PF_5, which cause

relatively low thermal stability.[14,39]

(4) $LiSO_3CF_3$: This salt show high thermal stability due to its strong C-F bond, however, also exhibit poor ionic conductivity than others.[40]

(5) $LiN(SO_2CF_3)_2$: This salt hardly suffers from hydrolysis due to the strong C-F bond, but, it does not generate passivating layer on Al current collector to cause Al corrosion at oxidative condition.[41]

The key features for the usually used lithium salts are summarized as in table 1.[36]

2.2.2. Organic solvents

Basically, in LIBs, solvents should not react with lithium ion, and thus aprotic organic solvent must be employed. Usually, these aprotic organic solvents show less dielectric constant than water. Therefore, organic solvents with high dielectric constant such as cyclic carbonates are used to provide high dissociable medium in electrolytes. These features, however, are largely offset by their relatively high viscosity; the higher dielectric constant, the higher polarity and thus the viscosity increase. Based on this tendency, a composition obtained by mixing a high dielectric constant-owned solvent and a low viscous solvent is used. In

LiBs, some mixed compositions are used: cyclic carbonates with high dielectric constant like ethylene carbonate (EC) and linear carbonates with low viscosity such as dimethyl carbonate (DMC). The physical properties of some typical carbonate organic solvents are summarized in table 2.[35,37]

Table 1. The features for lithium salts as electrolyte solutes.[36]

Salt	Structure	M. Wt	T_m/ °C	$T_{decomp.}$, / °C in solution	Al-corrosion	σ /mScm^{-1} (1.0 M, 25 ° C) in PC	in EC/DMC
$LiBF_4$	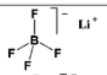	93.9	293 (d)	> 100	N	3.4 [a]	4.9 [c]
$LiPF_6$	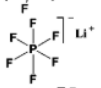	151.9	200 (d)	~ 80 (EC/DMC)	N	5.8 [a]	10.7 [d]
$LiAsF_6$	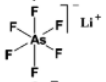	195.9	340	> 100	N	5.7 [a]	11.1 [e]
$LiClO_4$	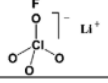	106.4	236	>100	N	5.6 [a]	8.4 [d]
Li Triflate	$Li^+ CF_3SO_3^-$	155.9	>300	>100	Y	1.7 [a]	
Li Imide	$Li^+ [N(SO_2CF_3)_2]^-$	286.9	234 [b]	>100	Y	5.1 [a]	9.0 [e]
Li Beti	$Li^+ [N(SO_2CF_2CF_3)_2]^-$				N		

Table 2. The physical properties of typical organic solvents.[35,37]

	FW	density /g cm^{-3}	ϵ	η/cP	E_{HOMO}/eV	E_{LUMO}/eV
EC	88	1.32	90	1.9	-12.86	1.51
PC	102	1.20	65	2.5	-12.72	1.52
DMC	90	1.06	3.1	0.59	-12.85	1.88
EMC	104	1.01	3.0	0.65	-12.71	1.91
DEC	118	0.97	2.8	0.75	-12.59	1.93

2.3. Active materials

2.3.1. Nickel doped lithium manganese spinel ($LiNi_{0.5}Mn_{1.5}O_4$)

$LiNi_{0.5}Mn_{1.5}O_4$ (LNMO) is a nickel doped one of lithium manganese spinel ($LiMn_2O_4$, LMO), in which trivalent manganese ion is substituted with divalent nickel ion. In LMO, the manganese ion reversibly reacts from +3 to +4 during charging/discharging, while in $LiNi_{0.5}Mn_{1.5}O_4$, the nickel ion reversibly reacts from +2 to +4 with two electron reaction.[42] The higher operating voltage characteristic of LNMO than LMO, which is originated from the lower electron energy state of the divalent nickel ion than trivalent manganese ion. Their corresponding redox reaction (Ni^{2+}/Ni^{4+}) occurs at the lower electron energy level than Mn^{3+}/Mn^{4+}, and thus the reaction voltage of LNMO is much higher than LMO electrode.[2-4,6] The theoretical capacity of LNMO electrode is calculated to 147.7 mA h g^{-1}, and the practical capacity is usually reported to 120 ~ 130 mA h g^{-1}.[43-46] The reaction mechanism is as follow.[47]

$$Li^{+}Ni(\text{II})_{0.5}Mn(\text{IV})_{1.5}O_4 \rightleftharpoons Ni(\text{IV})_{0.5}Mn(\text{IV})_{1.5}O_4 + Li^{+} + e^{-}$$

(> 4.7 V *vs.* Li/Li^{+})

As is seen in Fig. 3, there are two types of the nickel doped lithium manganese spinel (LNMO) structures. The structures are drawn by the VESTA (Visualization for Electronic and Structural Analysis) software

Table 3. Structural parameters for the two types of the $Fd\bar{3}m$, $P4_332$ LNMO structures.

Space group	Atom	Wyckoff position	Lattice parameter / Å	Coordinates x	y	z	Site occupancy	Thermal parameter B / Å^2
$Fd\bar{3}m$	Li	8a	8.172	1/8	1/8	1/8	1	0.55
	Ni	16d		1/2	1/2	1/2	0.5	0.43
	Mn	16d		1/2	1/2	1/2	1.5	0.43
	O	32e		0.263	0.263	0.263	4	1.31
$P4_332$	Li	8c	8.166	0.0129	0.0129	0.0129	1	1.44
	Ni	4b		5/8	5/8	5/8	0.5	2.34
	Mn	12d		1/8	0.3791	-0.1291	1.5	2.34
	O1	8c		0.3863	0.3863	0.3863	2	2.55
	O2	24e		0.1492	-0.1467	0.1313	2	2.55

Table 4. Cation-Oxygen bond distances for the two LNMO structures.

Space group	Li-O / Å	Ni/Mn-O / Å
$Fd\bar{3}m$	1.96	1.94
$P4_332$	Li-O1: 2.02	Ni(4b)-O2: 2.05
	Li-O2: 1.93	Mn(12d)-O1: 1.91
		Mn(12d)-O2: 1.91

(a) $Fd\bar{3}m$

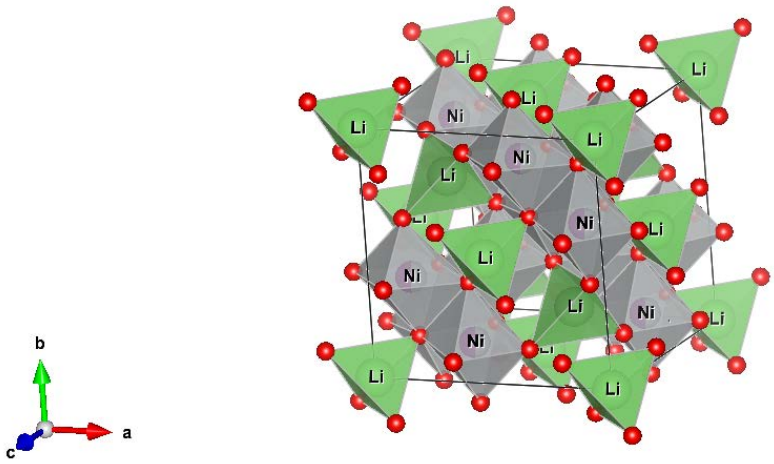

(b) $P4_332$

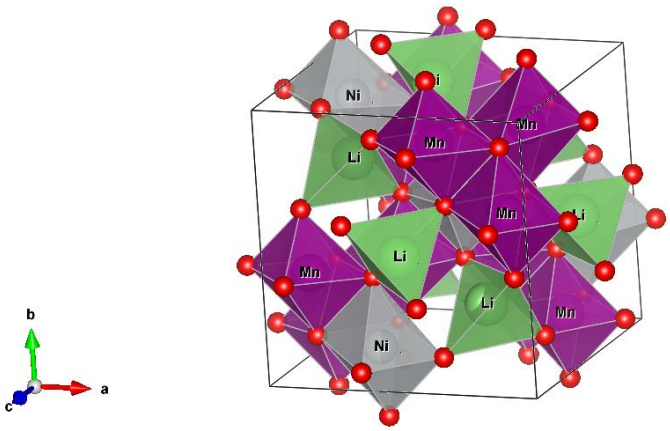

Figure 3. Two types of the LNMO structures illustrated from VESTA software program. (a); $Fd\bar{3}m$, (b); $P4_332$.

program. All the structures are based on face-centered cubic Bravais lattice. The disordered structure, $Fd\bar{3}m$ space group, is generated by Mn^{3+} impurity or oxygen deficiency, and the ordered structure, $P4_332$ space group, in which all manganese ions are tetravalent oxidation state (Mn^{4+}). The two structures are determined by synthesis temperatures and annealing process.[47-50] Table 3 and 4 show structural parameters and bond distances for two types of LNMO structures,[48-52] which were used for the software program to illustrate their structures. In $Fd\bar{3}m$ (Fig. 3a), note that Ni^{2+} and Mn^{4+} metal cations occupy in the same Wyckoff position (Table 3), only Ni^{2+} cation is illustrated in this Fig. 3a.

In spinel structure, described in AB_2O_4, A cation is in tetrahedral site of neighboring oxygen atoms and B cation is in octahedral site of the oxygen atoms: Li^+ cation is in tetrahedral site and Ni^{2+} or Mn ions in octahedral site. Generally, there is a consensus that the disordered spinel ($Fd\bar{3}m$) structure exhibits a little more improved cycle life and rate performances than the ordered spinel ($P4_332$) structure.[2,42,51,53,54] It is likely due that $P4_332$ get stress from noticeable lattice parameters changes two times, while $Fd\bar{3}m$ does one time during lithiation or delithiation.[2] That is to say, abrupt phase transition more occurs in $P4_332$ than $Fd\bar{3}m$.

2.3.2. Graphite

Graphite crystal structures are constructed in z-axis direction by ABAB stacking of graphene layers, in which sp^2 hybridization of carbon atoms are covalently combined in a form of hexagonal planar. π electrons provide Van der Waals force between graphene layers to form hexagonal based crystal structure ($P6_3/mmc$).[37,55] Some graphites are often stacked by ABCABC manner to form rhombohedral structure ($R\bar{3}m$).[56]

When Li^+ ions are intercalated into graphite electrode, Li^+ ions begin to be intercalated at edge plane. At initial lithiation period, Li^+ ions are intercalated into one Li^+ layer between graphene sheets. Graphites are converted from ABAB to AAAA stacking, and Li^+ intercalated layers and not intercalated layers are periodically aligned. According to periodicity of the Li^+-intercalated layer, the lithiated graphite layers are referred to stage 3, stage 2, and stage 1. For example, when the gap between the Li^+ intercalated layers is three, the intercalated state is called to stage 3 (LiC_{18}).[19,57] Hence, during lithiation, Li^+ intercalated graphite changes from stage 3 to stage 1 (Fig. 4). This lithiation reactions show three plateau regions, which means that two phases co-exist during the reaction stage. All the Li^+ intercalations into graphite electrodes occur below 0.25 V (*vs.* Li/Li^+).[20]

$$C_6 + Li^+ + e^- \rightleftarrows LiC_6 \quad (< 0.25\ V\ vs.\ Li/Li^+)$$

Commercially, graphites are provided from natural graphites and

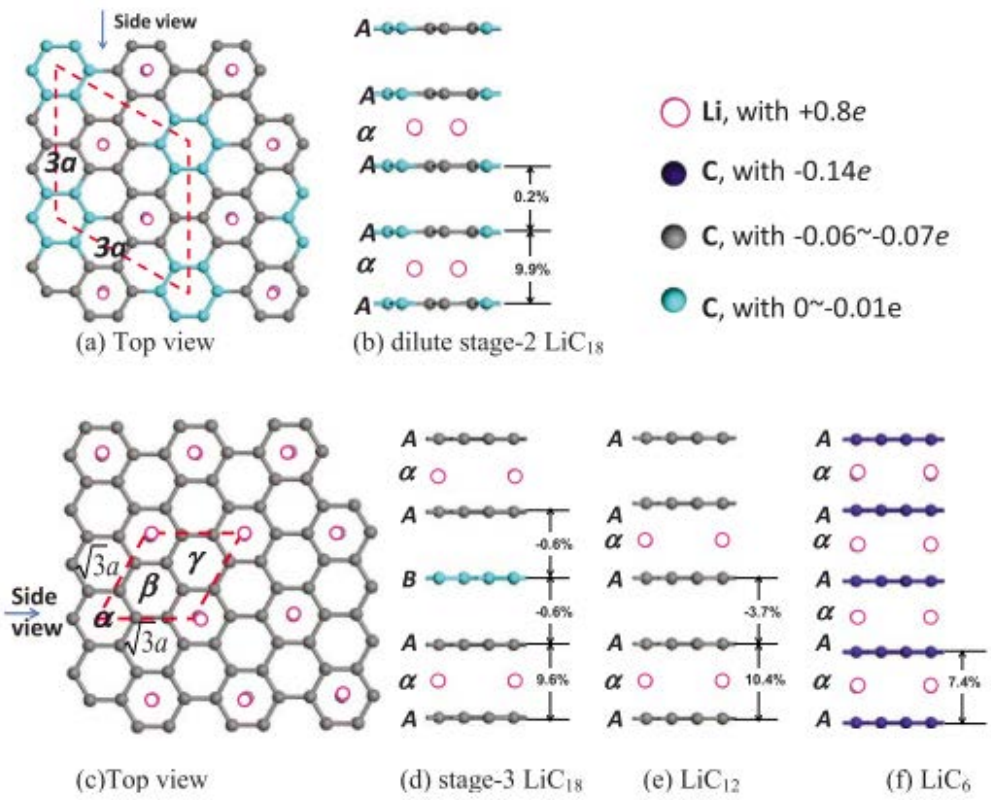

Figure 4. Staging phenomena during Li^+ intercalation into graphite electrodes.[57]

artificial graphites. Natural graphites, naturally mined from nature, exhibit 365 mA h g^{-1} of capacity,[58-61] close to theoretical capacity 372 mA h g^{-1}, however, expose edge planes a lot to allow considerable electrolyte decomposition.[37] Note that electrolyte decomposition occurs more at edge plane than basal plane due to high population of electron density at edge plane in the first cycle.[62] In order to decrease this irreversible electrolyte decomposition, natural graphites are usually post-processed in the form of a smooth surface morphology.

In addition, artificial graphites are obtained by carbonizing from carbon of coal or petroleum pitch. By heat treatment, the carbon that easily converted to graphite, which is named to soft carbon. On the other hand, even over at 2500 ℃, the carbon that hardly converted to graphite, which is called to hard carbon. The soft carbon, included in amorphous carbon, grows graphitization by heat treatment. During heat treatment, growing from pitch to semi-cokes, the stabilized small sphere grows in lamella form, which is mesophase with anisotropy and liquidity. The meseophases are referred to MCMB (Mesophase Carbon Microbeads).[37] For example, the commercially used MCMB-25-28 means that average diameter is 25 μm and heat treatment temperature is 2800 ℃. These MCMB series still involve a lot of amorphous phase at graphite surface to allow comparatively less exposure of graphite layer to electrolytes. This also permits less practical capacity (320 mA h g^{-1}) than

natural graphite (365 mA h g^{-1}),[63] however, if the amorphous phase are significantly eliminated at the graphite surface, the practical capacity of MCMB could enhance to 340 mA h g^{-1}.

2.3.3. Lithium titanate spinel ($Li_4Ti_5O_{12}$)

Lithium titanate spinel ($Li_4Ti_5O_{12}$, hereafter LTO) theoretically has 175 mA h g^{-1} of capacity, and does not show change of crystal lattice (zero strain) during charging/discharging to deliver capacity close to theoretical value and exhibit nearly 100 % of Coulombic efficiency.[64] Li^+ ions are intercalated by two phase reaction, which shows plateau in its voltage profile. This lithiation reaction occurs by the following reaction equation at about 1.5 V (*vs.* Li/Li^+),[65-67] which operates within electrochemical stability of the conventional carbonates-based electrolytes (1.0 ~ 4.3 V).[7] Due to their reaction potential, solid electrolyte interphase does not evolve on electrolyte/electrode interface unlike graphite electrode, and thus this material does not often show film resistance at the beginning of cycles.[68]

$$Li^{8a}[Li_{1/3}Ti_{5/3}]^{16d}O_4^{32e} + Li^+ + e^- \rightleftarrows Li_2^{16c}[Li_{1/3}Ti_{5/3}]^{16d}O_4^{32e}$$

(1.5 V *vs.* Li/Li^+)

Table 5. Structural parameters for the LTO structures ($Fd\bar{3}m$).

Phase	Atom	Wyckoff position	Lattice parameter / Å	Coordinates x	y	z	Site occupancy	Thermal parameter B / Å^2
$Li_4Ti_5O_{12}$	Li1	8a	8.3636	0	0	0	1	0.32
	Li2	16d		0.625	0.625	0.625	0.16	0.74
	Ti	16d		0.625	0.625	0.625	0.84	0.74
	O	32e		0.3878	0.3878	0.3878	1	0.77
$Li_7Ti_5O_{12}$	Li1	16c	8.3581	0.125	0.125	0.125	2	0.32*
	Li2	16d		0.625	0.625	0.625	0.16	0.74*
	Ti	16d		0.625	0.625	0.625	0.84	0.74*
	O	32e		0.3878	0.3878	0.3878	1	0.77*

*The thermal parameters for $Li_7Ti_5O_{12}$ were borrowed from that for $Li_4Ti_5O_{12}$.

Table 6. Cation-Oxygen bond distances for the LTO structures.

Phase	Li-O / Å	Ti-O / Å
$Li_4Ti_5O_{12}$	Li1-O: 1.98 Li2-O: 1.99	Ti-O: 1.99
$Li_7Ti_5O_{12}$	The bond distances for $Li_7Ti_5O_{12}$ were approximately entered in VESTA software program to the maximum value of 2.2 Å.	

(a) $Li[Li_{1/3}Ti_{5/3}]O_4$ (delithiated)

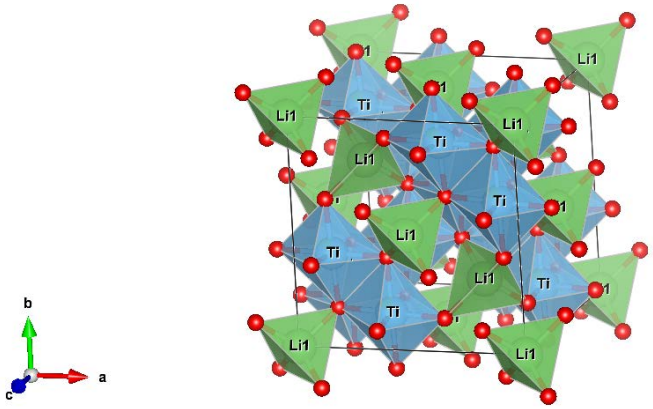

(b) $Li_2[Li_{1/3}Ti_{5/3}]O_4$ (lithiated)

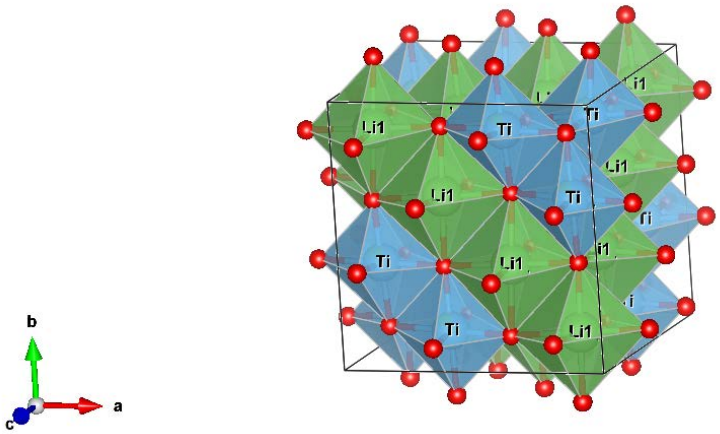

Figure 5. The LTO structures ($Fd\bar{3}m$) illustrated from VESTA software program. (a); delithiated $Li[Li_{1/3}Ti_{5/3}]O_4$, (b); lithiated $Li_2[Li_{1/3}Ti_{5/3}]O_4$.

$Li_4Ti_5O_{12}$ is based on face-centered cubic Bravais lattice, and its corresponding space group is $Fd\bar{3}m$. The structural parameters and bond distances are summarized in table 5 and 6,[69-72] which were used for illustrating LTO structure (Fig. 5). Note that Li^+ and Ti^{4+} cation are in the same Wyckoff position, only Ti^{4+} cation is illustrated in Fig. 5. 1 mol of Li^+ ions in tetrahedral site, and one third mol of Li^+ and Ti^{4+} ions are octahedral site before lithiation (Fig. 5a). When Li^+ ions are intercalated, all Li^+ ions are inserted in octahedral site in LTO structure (Fig. 5b).[65,67,72] The lithiated $Li_2[Li_{1/3}Ti_{5/3}]O_4$ was confirmed XRD pattern from previous report due to absence of pdf card in JCPDS.[65] During charging/discharging, the lattice parameter almost does not change ($\Delta V = 0.0682$ %), and thus LTO shows nearly zero strain property.

The initial Ti^{4+} ion is poor electron-conducting to show low electron conductivity of LTO electrode.[37]

2.3.4. Two-phase reaction

In two components system, electrochemical reaction potential was accounted for by Gibbs phase rule: F = C – P + 2, in which F: degree of freedom, C: number of components, and P: number of phase. When electrochemical Li^+ insertion reaction occurs in host materials, if the two

components react with one phase, the resulting degree of freedom F is determined to 3. Even though temperature and pressure are fixed, the final degree of freedom F, number of values are free to change, is considered to 1. Hence, the Gibbs energy or electrochemical reaction potential changes with regard to mol of Li^+ ions in the host material. This reaction is referred to “one phase reaction” or “solid solution reaction”.[73] The “solid solution” means a single homogeneous phase, in this case, Li^+ ions as a solutes are randomly distributed in the host material as solvent. Of course, temporal Li^+ gradients would appear. On the other hand, if the two components react with two phases, the resulting degree of freedom F is determined to 2. When temperature and pressure are fixed, the final degree of freedom is determined to 0. Resultantly, any thermodynamical intensive property such as Gibbs energy does not vary during this insertion reaction to exhibit plateau in electrochemical reaction voltage profile.[73]

Fig. 6 shows Gibbs free energy and electrochemical cell voltage for two-phase reaction with regard to Li^+ compositions. Electrochemical potential is defined by differential Gibbs free energy for charge quantity: $E = -\frac{\Delta G}{zF}$. [73] Note that Li^+ ions always move with electrons in LIBs. In two-phase reaction (Fig. 6), the summed Gibbs free energies in phase Ⅰ and Ⅱ-crossed region linearly increase or decrease, and thus the differentiated value, electrochemical potential, are constantly preserved to exhibit

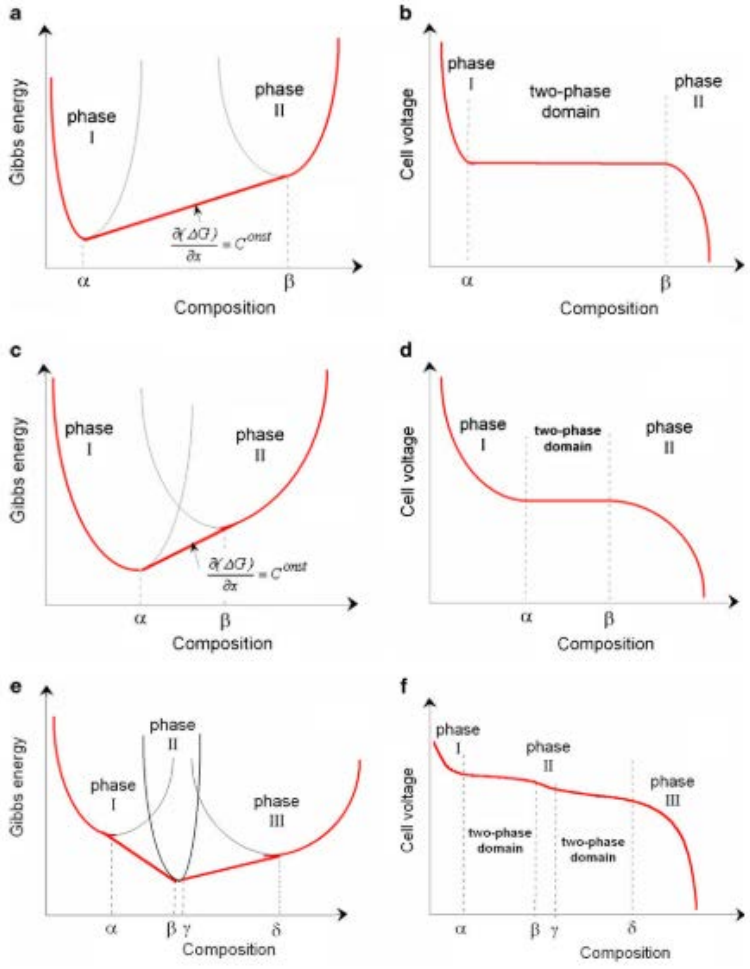

Figure 6. Gibbs diagram and electrochemical reaction potential for two-phase reaction.

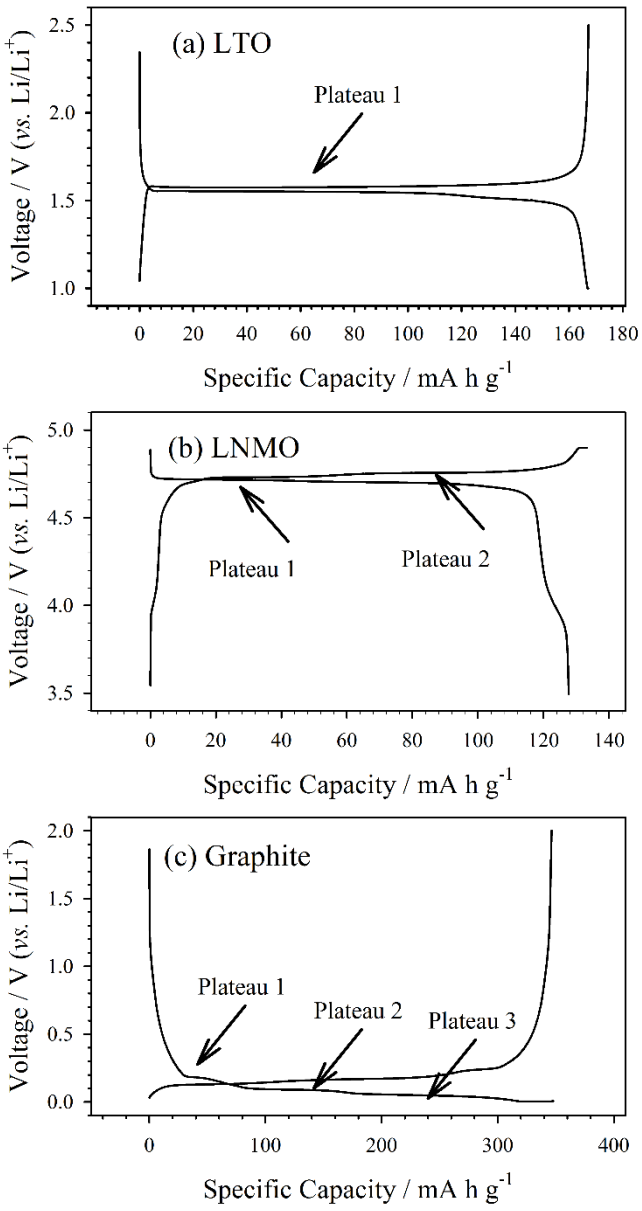

Figure 7. Plateaus in voltage profiles. (a) LTO, (b); LNMO, and (c); graphite electrodes.

plateau in voltage profiles.[2] This can be accounted for by that electrons are consumed to convert phases associated with the two-phase reaction. The length of plateau depends on the Li^+ composition length for two phases co-existance (Fig. 6 abcd). Additionally, one-phase reaction appears at initial or latter period for the two-phase reaction (terminal period for charging/discharging) to exhibit slope in voltage profile. In this Li^+ composition, only Gibbs free energy for one phase determines electrochemical reaction voltage.

For LTO electrodes, the two-phase reaction for $Li_4Ti_5O_{12}$ and $Li_7Ti_5O_{12}$ phases occurs for most Li^+ reaction period. A pretty long plateau thus are shown in their voltage profiles like in Fig. 6b and 7a.[74] For LNMO electrodes, the two-phase reactions for $LiNi_{0.5}Mn_{1.5}O_4$ (phase Ⅰ), $Li_{0.5}Ni_{0.5}Mn_{1.5}O_4$ (phase Ⅱ), and $Ni_{0.5}Mn_{1.5}O_4$ (phase Ⅲ) occurs two times during charging/discharging. Below 0.5 mol of Li^+, phase Ⅰ and phase Ⅱ co-exist, and over 0.5 mol of Li^+, phase Ⅱ and phase Ⅲ co-exist.[75,76] The two plateaus reactions are thus exhibited in their voltage profiles (Fig. 6ef and 7b). For graphite electrodes, the two-phase reaction occurs three times during charging/discharging. When Li^+ ions are inserted, two-phase reaction consecutively occurs in the following order: staging 3/2L → staging 2L/1 → staging 2/1 (Fig. 7c).[19] All electrodes materials used in this work react by two-phase reaction.

Gibbs phase rule on electrochemical potential is discussed for the two components system in this initial part. However, regardless of how many components are in the electrochemical system, the pseudobinary (two-phase) system also follows this plateau reaction potential.[73] Most of insertion materials such as LTO and LNMO electrodes follow this behavior. When Li^+ ions are inserted in the host material, if another phase with different Li^+ composition evolve in the host material, it is called to reconstruction reaction. That is to say, two-phase reaction is reconstruction reaction. This reconstruction reaction has phase boundary, which is interface between the different two phases. Unlike one-phase reaction, randomly distributed guest ion (Li^+) in the host material, this phase boundary moves to or out from core of electrode particles in two-phase reaction.[74]

2.4. Solid Electrolyte Interphase (SEI)

Graphite electrodes reacts reversibly during a long-term cycling, even though they operates beyond the electro-reduction limit of the conventional carbonates-based electrolytes.[7] Carbonates-based electrolytes are electro-reductively decomposed to form a surface film on graphite electrode. This layer is highly passivating to prevent electrolyte solvents and discourages electron tunneling in negligible, but Li^+ ions translocate through some lattice sites in the solid matrix with knock-off mechanism such as solid electrolyte.[26,27] Based on these observations, E. Peled referred this surface layer to “solid electrolyte interphase (SEI)”.[22] In this section, SEI-forming process, Li^+ ion migration, and completion of passivating ability are ascertained by some experiments.

In first cycles, electrolytes are electro-reduced to be decomposed and the concomitant surface film is deposited on graphite electrodes. The reaction occurs irreversibly to show 28.7 mA h $^{-1}$ of the irreversible capacity in the first cycle (Fig. 8a). Typically, carbonates-based electrolytes are electrochemically reduced at 0.65 V (vs. Li/Li^+) to generate SEI on graphite electrode as seen in Fig. 8b.[77,78] The irreversible capacity at 0.65 V, however, does not explain total irreversible capacity: the irreversible capacity to 0.5 V is 17.8 mA h g^{-1}, and the total irreversible capacity is 28.7 mA h g^{-1}. The residual capacity, 10.9 mA h g^{-1} indicates that SEI-forming process is further progressed at the lower

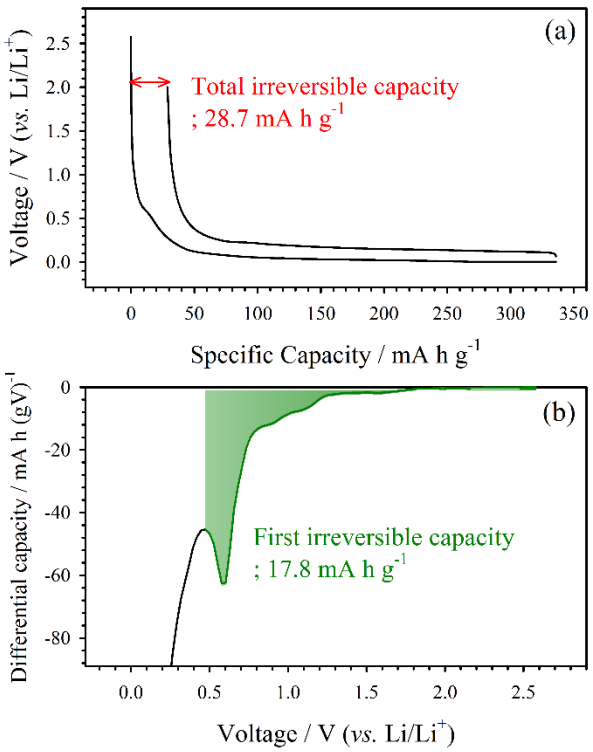

Figure 8. The galvanostatic charging/discharging for graphite electrode in the first cycle. Voltage profiles; (a), differential capacity plot; (b). The irreversible capacities are indicated in the inset.

voltage region below 0.25 V, even after passing this typical electrolyte decomposition voltage at 0.65 V. It needs thus to be ascertain what electrochemical reactions occur at highly electro-reductive potential below 0.25 V.

In order to understand the SEI-forming reaction on graphite electrodes, the graphite surface was analyzed by XPS with step charging process. When electrode voltage reaches to about 1.0 V, SEI begins to be generated as seen in the 1.0 V spectra of Fig. 9. If the first irreversible reaction (0.65 V) is progressed up to 0.35 V, organic components such as lithium alkyl carbonate ($ROCO_2Li$) and lithium fluoride (LiF) are generated as the primary products. At the graphite charging cut-off voltage at 0.005 V, which is highly electro-reductive atmosphere, lithium carbonate (Li_2CO_3) and lithium oxide (Li_2O) becomes richer than at the 0.35 V. After complete charging (at 0.005 V), the carbonate solvents-derived inorganic components (Li_2CO_3 and Li_2O) and the salt anion-derived inorganic component (LiF) are significantly deposited even to the deepest bottom region of SEI in high population (Fig. 10; XPS depth profile). The carbonate derived inorganic components are additionally generated, which is obvious. The SEI becomes thicker from 0.35 V to 0.005 V. In detail, not lithiated graphite sp^2 signal for the 0.35 V spectra reveals noticeably after Ar^+-etching for 1800 s. For the 0.005 V spectra, the lithiated graphite Li_xC_6 signal is observed after Ar^+-etching for 3600 s. This depth profiles ascertains that the Li_2CO_3 and Li_2O are generated and thus the

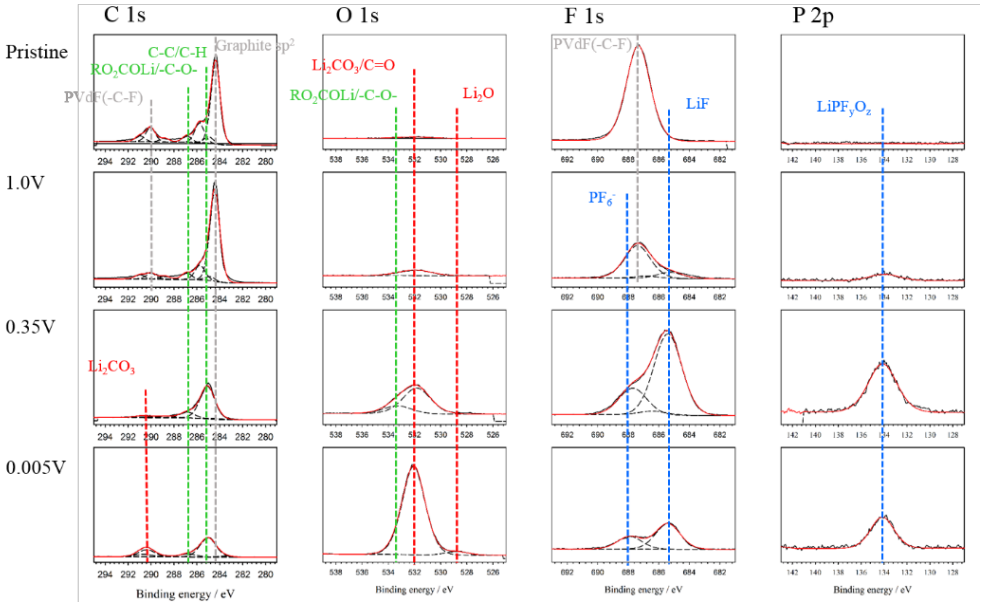

Figure 9. The topmost graphite electrode surface observed from XPS with step charging process after washing with DEC.

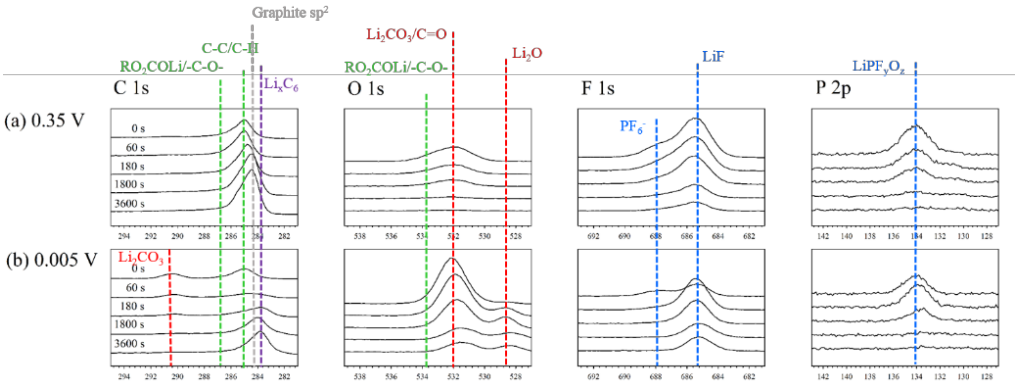

Figure 10. The XPS depth profiling of the SEI after the first (a; 0.35 V) and second (b; 0.005 V) irreversible reaction.

interphases are thickened. As a result, organic components are in the upper region, and the inorganic components constitute SEI to the deepest region. The SEI-forming process is summarized in Fig. 11.

This SEI-forming process is also understood from the suggested mechanism of SEI components. When carbonates are electro-reduced with one electron, they are polymerized to a some degree to be terminated with lithium ion, and thus form organic layer. When salt anion is electro-reduced, it receives two electron from graphite electrodes to generate LiF and PF_3. If carbonates are electrochemically reduced with two electrons, the evolved anion combines two Li^+ to be precipitated in a form of Li_2CO_3, which could be further reduced by two electrons to generate Li_2O. The latter two reactions are more electron consuming reaction than the generation of organic layer, and thus they occurs at more highly reductive atmosphere, lower voltage.[36,79]

Now let's look at lithium ion migration when each phase is created (Fig. 12). After the first irreversible reaction of green, organic matter and LiF are formed, resulting in a semi-circle showing resistance. After the second irreversible reaction of red, an additional two semicircles are created, resulting in a total of three semicircles. Looking closely at the Bode plot, one phase angle change is shown in the high frequency region for the first semicircle, and another phase angle change is observed in the lower frequency (medium frequency) region. The orange one at the end can be regarded as the charge transfer resistance, and the second change of the phase angle (blue) prior to the charge transfer

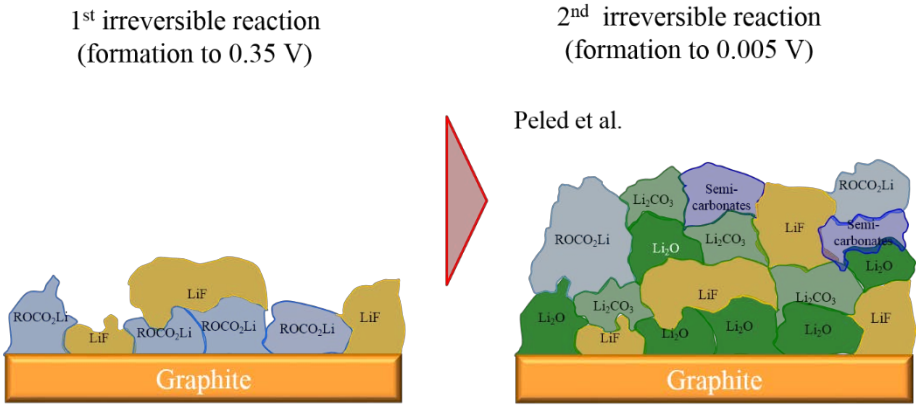

Figure 11. SEI-forming process during electrochemical charging.[23]

reaction, it is obviously observed for that the lithium ion movement in the lithium carbonate and the lithium oxide produced by the second irreversible reaction of SEI-forming reaction. Since, the lithium ion migration in these phases is observed in the lower frequency region than the organic matter in the upper part, Li^+ ion migration becomes somewhat slower in this bottom region. Practically, Peng Lu et. al proved by TOF-SIMS technique that Li^+ ion diffuses with electrolyte components like salt anion in the upper porous organic layer and the migration rate becomes slower during passing through these inorganic components.[26,27] These multilayer components were also observed by ac impedance from the previous literature.[23,80,81] The Li^+ ion diagram is sketched in Fig. 13.

This Li^+ ion migration property supports that SEI consists of two part macroscopically: it is generally accepted that the upper organic layer is porous to allow electrolytes diffusion in them, while the bottom of inorganic layer is densely packed to allow for only Li^+ ion translocation conduction in its solid matrix with knock-off mechanism.[27] This macroscopic bilayer property is also observed in image by TEM. Fig. 14 displays SEI morphology after charging graphite electrode to 0.005 V. The image certainly exhibits that the upper and the bottom of regions are different. Considering with the previous XPS spectra, the upper region is the organic layer such as lithium alkyl carbonate, and the deepest region is the inorganic layers, which is densely packed to be responsible for the high passivating characteristic of SEI.

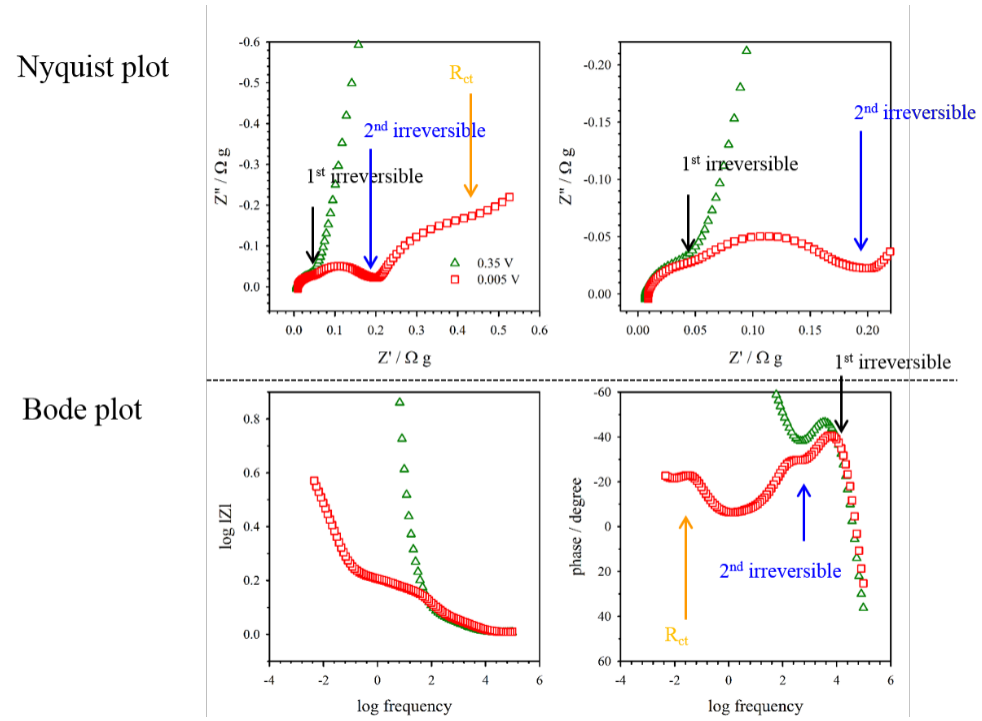

Figure 12. Ac impedance for the graphite electrodes during electrochemical charging. The spectra were obtained from the graphite/graphite symmetric cells after charging in Li/graphite cells. (a); Nyquist plot, (b); Bode plot.

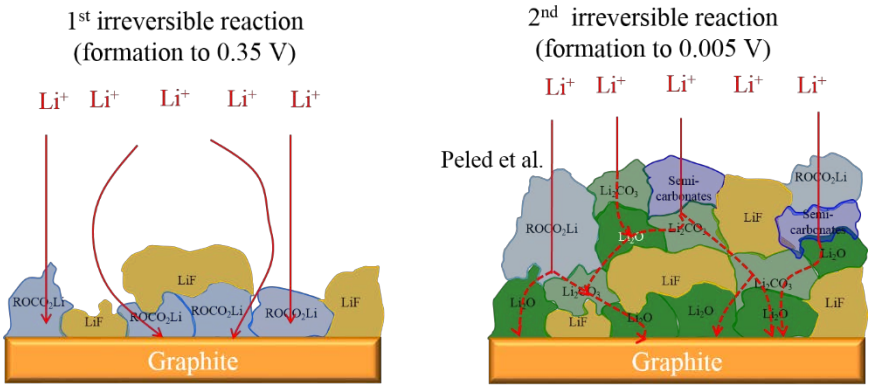

Figure 13. Li^+ migration kinetics in SEI on graphite electrodes.

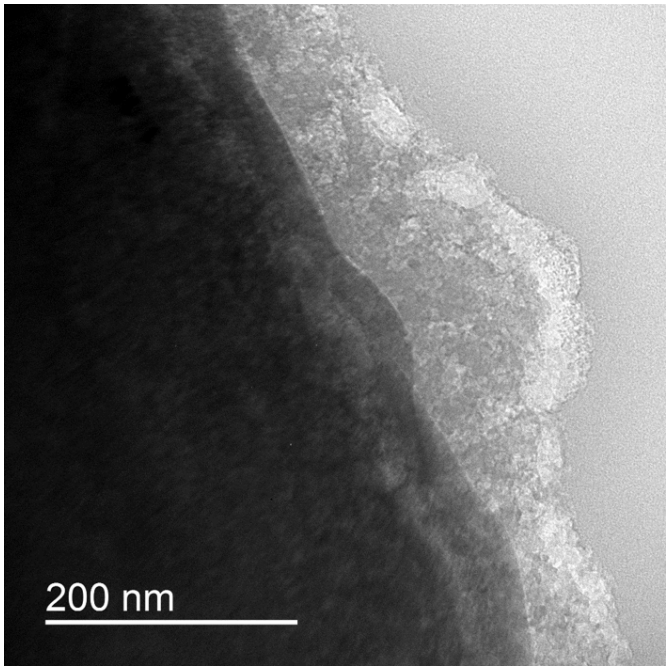

Figure 14. SEI morphology on graphite electrode obtained from TEM after the charging once to 0.005 V.

3. EXPERIMENTAL

3.1. Preparation of electrodes, electrolytes, and electrochemical cells

3.1.1. Electrolytes preparation

The basically used background electrolyte is 1.3 molar (*M*) lithium hexafluorophophate ($LiPF_6$) in ethylene carbonate (EC):ethyl methyl carbonate (EMC):diethyl carbonate (DEC) with 3:2:5 of volume ratio (*v/v/v*), which was purchased from Panaxetec Corp. This basic electrolyte was used to generate the two surface film: SEI and SPI on each negative and positive electrode.

In order to change ionic conductivity, the Li salt: $LiPF_6$, was dissolved and concentrated in the various electrolyte composition. In the first part, the $LiPF_6$ was concentrated from 0.05 to 4.0 *M* in EC:dimethyl carbonate (DMC) = 5:5 (*v/v*) composition. In the second part, the $LiPF_6$ Li salt was concentrated from 0.75 to 2.5 *M* in various composition. The used solvents composition were from EC:DMC = 5:5, 3:7, 1:9 (*v/v*), and DMC alone.

For ascertaining permeable property through spectrometrical tool, the wetting electrolyte and the film-generating electrolyte were discriminated. The basic background electrolyte was used to generate surface films on LNMO electrode. The wetting electrolyte was newly prepared with the following composition: 1.3 *M* lithium perchlorate ($LiClO_4$) in four deuterated EC (EC-D_4):DEC = 3:7 (*v/v*).

When examining permeability for the two surface films through redox couple, the nickel (Ⅱ)-cyclam$[BF_4]_2$ redox couple was previously synthesized and followed to be added into the background electrolyte at 0.01 or 0.1 *M* of concentration.

3.1.2. Synthesis of Ni(cyclam)$[BF_4]_2$ (Ni(Ⅱ)-cy)

Cyclam (Alfa Aesar, MA, USA 98%) and Nickel(Ⅱ) tetrafluoroborate hexahydrate ($Ni[(BF_4)]_2 \cdot (H_2O)_6$, Alfa aesar) were dissolved into each 10 mL of ethanol in one equivalent. The two dissolved solutions were mixed and stirred at 25℃ for 5h. The reacted mixture were heated at 45℃ until 5mL of the residual is left. The precipitated solution was dissolved in 10 mL of acetone and followed to dissolved in 100 mL of diethyl ether. The re-dissolved solution was centrifuged at 5000 rpm for 5 min and the resulting supernatant was extracted. These re-dissolution and

centrifugation were repeated in three times. The final supernatant was dried in vacuum at 80℃ overnight. The synthesized Ni(Ⅱ)-cyclam$[BF_4]_2$, as shown in Fig. 15, is dissolved in 1.3 *M* $LiPF_6$ in EC:EMC:DEC = 3:2:5 (*v/v/v*) at a concentration of 0.01 *M* and stirred overnight.

3.1.3. Electrodes preparation

The two $LiNi_{0.5}MnO_{4-\delta}$ (LNMO, $Fd\bar{3}m$ crystal structure, JCPDS #: 802162) powders were used for the preparation of positive electrodes. When examining the surface film properties on positive electrodes, the Brunauer-Emmett-Teller (BET) surface area = 3.20 $m^2\ g^{-1}$ of one (Tanaka Corp., Japan) was employed, and the BET surface area = 0.43 $m^2\ g^{-1}$ (LG chem. Corp., South Korea) of one was introduced to test rate properties. For negative electrodes, artificial graphite ($P6_3/mmc$, JCPDS #: 080415, LG chem. Corp., South Korea, BET surface area = 3.17 $m^2\ g^{-1}$) was introduced to examine the surface film properties on graphite electrodes and $Li_4Ti_5O_{12}$ ($Fd\bar{3}m$, JCPDS # 490207, LG chem. Corp., South Korea, BET surface area = 0.24 $m^2\ g^{-1}$) was employed to test rate properties.

The composite electrodes were prepared from mixture of LNMO, LTO, or artificial graphite, conducting carbon (Super-P), and

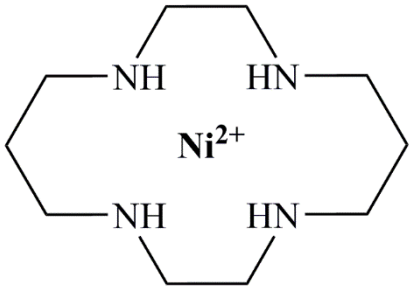

Figure 15. The synthesized Ni(Ⅱ)-cyclam[BF_4]$_2$

poly(vinylidenefluoride) (PVdF, KF 1300) (94:3:3 in wt.%). These mixtures were dispersed in *N*-methyl-2-pyrrolidone, and the resulting slurries were coated on Al foil (LNMO, LTO) or Cu foil (graphite). These coated foils were dried at 120℃ for 20 min, and followed by pressing to reinforce the adhesion and electric contact between the electrode constituents. The loaded foils were punched with a diameter of 11 mm (area; 0.95 cm^2), and then they were dried in vacuum at 120℃ overnight. Their loading mass and thickness were 2.5 mg (Al; 5.56 mg, Cu; 8.45 mg) and 25 μm (Al; 21 μm, Cu; 10 μm), respectively.

In order to obtain surface film components without non-surface film components: carbon conducting agent or binder when measuring X-ray photoelectron spectroscopy (XPS), the LNMO powder was embedded on gold (Au) plate and graphite powder was pressed in a nickel (0)-foam. The carbon and binder-free electrodes were prepared with same manner in the above paragraph.

3.1.4. Fabrication of electrochemical cells

These electrodes were assembled with a Li metal counter, a Li metal reference, a PP/PE/PP (polypropylene, polyethylene) separator, and electrolytes in forms of two-electrode coin-type cells (CR2032), three-

electrode polyether ether ketone (PEEK)-type cells, or three-electrode beaker-type cells depending on experiments. In order to scrutinize only interfacial properties, some inert electrodes were introduced to be assembled with a Li counter, and a Li reference in the forms of PEEK-type cells or vial-type cells. Pt electrodes were for generating films, Cu electrodes were for generating SEI, and glassy carbon electrodes were for confirming reversible reaction of redox couples after generating the two interphases. In order to confirm electron tunneling, the Li/Li/glassy carbon rod three electrode vial-type cells were additionally introduced to ascertain reversible reaction of a redox probe molecules. When measuring ac impedance, three-electrodes PEEK type cells, or symmetric cells were assembled: LNMO/LNMO, graphite/graphite, LTO/LTO symmetric cells. The LTO/LNMO full-cells were assembled as same manner in the previous Li half-cells. In full-cells, diameter of the LTO and LNMO electrodes was each 12 and 11 μm, and the N/P ratio was controlled to 1.1 per unit area.

3.2. Electrochemical analysis

3.2.1. The galvanostatic charging and discharging cycling

In part one, for generating the two interphases on LNMO and graphite electrodes, the galvanostatic charge/discharge cycling was conducted

with Wonatech WBCS 3000 at 3.0~4.9 V (for LNMO electrodes) or 3.0~0.005 V (for graphite electrodes) at a current density of 0.1 *C* (LNMO; 12 mA g^{-1}, graphite; 30 mA g^{-1}).

In part two, 0.1 *C* of charging and discharging current was applied to Li/LTO (16 mA g^{-1}), Li/LNMO (13 mA g^{-1}), and LTO/LNMO full-cells (13 mA g^{-1}; based LNMO positive electrode) in three times for initial formation. The cut-off voltages of electrodes were 1.0 ~ 2.5 V; Li/LTO half-cells, 3.5 ~ 4.9 V (*vs.* Li/Li^+); Li/LNMO half-cells, and 1.5 ~ 3.5 V; LTO/LNMO full-cells. After initial formation, currents between 0.5 and 20 *C* (Li half-cells; based on working electrodes, full-cells; based on LNMO positive electrode) were applied to each electrochemical cell. Before examining rate performances, all working electrodes were controlled to state of charge (SOC) 0 or 100 by applying constant voltage at each cut-off voltage for 1 hour to eliminate or insert all Li^+ ions in the target electrodes.

3.2.2. Alternating current (Ac) impedance

3.2.2.1. Surface film and charge transfer resistances

In the first part, ac impedance spectroscopy (CHI 660B instruments) was performed at a frequency range of 0.005~100

kHz with an amplitude of 5 mV on three-types of cells. First, LNMO and graphite electrodes having similar BET surface area and loading mass were introduced to observe the two resistances of film and SEI because resistance depends on area and loading mass. To observe resistance of the two interphases, the Li/Li/LNMO PEEK cells charged up to 4.9 V (*vs.* Li/Li^+) and the Li/Li/graphite PEEK cells charged to 0.005 V. To compare these resistances of the two interphases at the same voltage, the previous two PEEK-type cells discharged to 3.0 V, and followed to be measured equally at 3.0 V. Second, a three-electrode Li/Li/platinum (Pt) and Li/Li/copper (Cu) PEEK-type cells (diameter of Pt and Cu; 5.0 mm) were introduced to monitor resistance per unit mass for the two interphases. Additionally, LNMO/LNMO and graphite/graphite symmetric coin-type cells were assembled with various $LiPF_6$-concentrated in EC:DMC = 5:5 (*v/v*) composition after charging each electrode once to each cut-off voltage.

In the second part, after first charging in Li half-cells, the LTO (SOC 10, quasi-open circuit voltage (QOCV) 1.56 V) and LNMO (SOC 100, QOCV 4.73 V) electrodes had been disassembled and re-assembled in each symmetric type cells, and which were scanned by ac impedance method. The used electrolytes were as

same as the previous charged one. All Nyquist plots are fitted via Z-view software program.

3.2.2.2. Ionic conductivity

Ionic conductivities of electrolyte compositions were examined through ac impedance method. Electrolytes were assembled in platinum(Pt)/Pt symmetric cell, which was scanned from 1 MHz to 1 Hz of frequency with 5 mV of amplitude by CHI 660B instrument. The real part of the nearest point to the real axis was converted to ionic conductivity by the equation: $\kappa = \frac{l}{A} \cdot \frac{1}{R}$ (κ; ionic conductivity, l; distance between electrodes, A; area of electrodes, R; resistance).[31,82] The constant *l/A*, usually referred to cell parameter, was calibrated by potassium chloride (KCl) standard solution (1 mS cm^{-1} at 25 ℃) purchased from Sigma-aldrich.

3.2.3. Electrochemical quart crystal microbalance (EQCM)

The deposited mass for the two interphases was measured using a quartz crystal microbalance (QCM, SEIKO Corp., quartz crystal analyzer 922) and linear sweep voltammetry (CHI instruments) simultaneously. The cells were assembled in a two-electrode cell with an AT-cut Pt or Cu quartz

crystal mirror finish disk (working electrode, diameter = 5.0 mm) and Li metal (counter and reference electrode). The scan rate was 1 mV s^{-1} to positively sweep up to 5.2 V (Pt quartz electrode) and negatively sweep down to 0.005 V (Cu quartz electrode). The oscillation frequency changes are converted to the mass change (Δm) by the Sauerbrey equation.[31,83,84]

$$\Delta m = -\frac{S\sqrt{\rho\mu}}{2{f_0}^2 n}\cdot\Delta f = -\frac{1}{C_f}\cdot\Delta f$$

where S is the surface area (S = $\pi \times 0.25 \times 0.25$ cm^2), ρ is the density of quartz (2.648 g cm^{-3}), μ is the shear modulus of quartz (2.947×10^{11} g cm^{-1} s^{-2}), f_0s are the basic frequencies for the Pt quartz (9.00×10^6 MHz) or Cu quartz (9.04×10^6 MHz), n = 1 is the harmonic number of the oscillation. The finally calculated sensitivity factors are $C_f = 933.977$ Hz μg^{-1} for Pt quartz and $C_f = 942.297$ Hz μg^{-1} for Cu quartz electrode.

3.2.4. Cyclic voltammetry

Cyclic voltammetry was performed by CHI instruments. For investigate reversible redox reaction of the Ni(Ⅱ)-cy after interphase-formation, the Li/Li/glassy carbon rod three electrode vial-type cells were introduced. SEI was generated on the glassy carbon rod by cyclic

voltammetry to 0.005 V at a scan rate of 1 mV s^{-1} with 1.3 *M* $LiPF_6$ in EC:EMC:DEC = 3:2:5 (*v/v/v*), and films were generated up to 5.2 V and 7.0 V (*vs.* Li/Li^+) at a same scan rate. After withdrawing the two interphases-generated glassy carbon electrodes from the interphases-generated vial cells and re-soaked with 0.01 *M* Ni(Ⅱ)-cyclam$[BF_4]_2$ dissolved in 1.3 *M* $LiPF_6$ in EC:EMC:DEC = 3:2:5 (*v/v/v*) in new vial cells. The re-soaked glassy carbon electrodes were cyclic sweep at various scan rates.

In addition, the Li/Li/LNMO or graphite three electrode beaker-type cells were introduced to investigate reversible redox reaction of the Ni(Ⅱ)-cy after the two interphases generation on the active materials. The cells were assembled with 9 mL of 1.3 *M* $LiPF_6$ in EC:EMC:DEC = 3:2:5 (*v/v/v*) and followed to be charged to each cut-off voltage and discharged to 3.0 V. After generating the two interphases on each electrode, 1 mL of 0.1 *M* Ni(Ⅱ)-cyclam$[BF_4]_2$ dissolved in 1.3 *M* $LiPF_6$ in EC:EMC:DEC = 3:2:5 (*v/v/v*) was re-added in the two cells to tune concentration of the Ni(Ⅱ)-cy as same as the previous glassy carbon vial cells. The cyclic sweep was performed at a scan rate of 50 mV s^{-1}.

3.3. Surface analysis

3.3.1. X-ray photoelectron spectroscopy (XPS)

Components for the two interphases were compared by using X-ray photoelectron spectroscopy (XPS). To this end, LNMO powder was emebedded on Au plates and graphite powder was pressed in nickel foams to prepare conducting agents and binder-free electrodes. The LNMO electrodes were charged up to 4.9 V, discharged to 3.5 V. The graphite electrodes were charged down to 0.005 V, and discharged to 2.0 V. The cells were disassembled and washed with DEC or not in an argon-filled glove box to obtain the electrodes, which were delivered to XPS instruments by sealing in vials without air exposure. Al Kα (1486.6 eV) X-ray source was radiated on the electrodes (a spot diameter 400 μm) and depth profiles were obtained with Ar^+ sputtering. All binding energies were calibrated by C 1s peak of hydrocarbon (285.0 eV).

3.3.2. Time of flight-secondary ion mass spectrometry (TOF-SIMS)

TOF-SIMS was introduced to quantify Li^+ ion concentration for the two interphase and observe the wetted electrolytes in the SPI. The Li/Li/Pt or Cu three electrode PEEK-type cells assembled with 1.3 *M* $LiPF_6$ in EC:EMC:DEC = 3:2:5 (*v/v/v*). The Pt electrodes were positively sweep to 5.2 V and the Cu electrodes were negatively sweep to 0.005 V at a scan rate

of 1 mV s^{-1}. The cells were disassembled in Ar-filled glove box and washed with DEC or not to collect the interphases-generated electrodes. The obtained Pt and Cu electrodes were sealed in vials without air exposure and delivered to the TOF-SIMS instruments (ION-TOF, Germany, TOF.SIMS 5). Cesium ion (Cs^+) was radiated on the electrodes (spot size; 50 μm × 50 μm) and the etched ion fragments were detected by time of flight method. The etching time was converted from sputtering time to distance by 0.4 nm s^{-1} based on etching rate of SiO_2 substrate. The ^6Li (natural ratio; 7.6%) was shown rather than the much richer isotope ^7Li (natural ratio; 92.4%) because intensities of ^7Li were saturated for both two electrodes not to discriminate their difference.

For observing the immersed electrolytes in films on LNMO electrode, TOF-SIMS was also performed on the film-generated LNMO electrodes. The Li/LNMO cells were charged up to 4.9 V with 1.3 *M* $LiPF_6$ in EC:EMC:DEC = 3:2:5 (*v/v/v*) and disassembled to collect the LNMO electrodes. The obtained LNMO electrodes were washed with DEC and re-wetted with 1.3 *M* $LiClO_4$ in four deuterated EC (EC-D_4):DEC = 3:7 (*v/v*) for 5 min. The film components, the re-wetted components, and active materials were detected by TOF-SIMS.

In the second part, the adsorbed Li intensities were measured on Al plate electrode. After Li/Al cells were assembled with the usual 1.0 *M* $LiPF_6$ of composition and 2.5 *M* $LiPF_6$ in DMC for 24 hour, the $^6Li^+$ intensities are

monitored on the Al plate electrode to confirm whether the highly concentrated electrolyte provide high Li^+ ion population on electrodes.

3.3.3. Transmission electron microscopy (TEM)

Transmission electron microscopy (TEM, JEOL LTD., JEM-2100F) was used to obtain images for the two interphases on the LNMO or graphite electrodes after 1st charging.

3.4. Physical properties characterization

3.4.1. Viscosity measurement

Viscosities of electrolyte compositions were measured by Cannon-Fenske Routine viscometer (Fig. 16). The migration time of fluids is converted to viscosity by the equation: $\eta = K\rho t$ (η; viscosity, K; constant for a viscometer, ρ; density of fluid, t; migration time of fluid).[85] The constant for the used viscometer was determined by being based on the viscosity of distilled water (0.890 cP at 25 ℃).

3.4.2. Raman spectroscopy

Interaction between solvents and lithium salt was observed by a raman

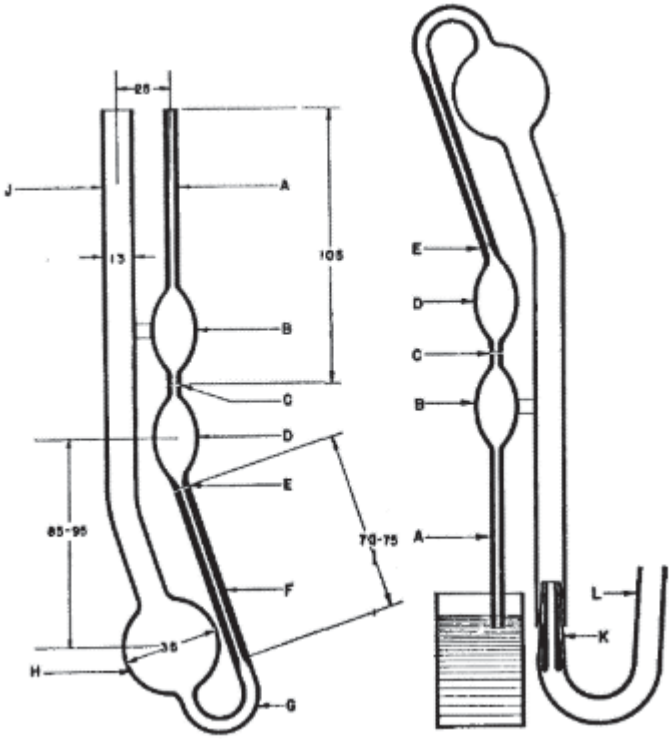

Figure 16. Cannon-Fenske Routine viscometer.[85]

spectroscopy (LabRAM HV evolution, HORIBA Co., Japan) with 532 nm of exciting laser. All electrolytes samples were sealed in Ar-filled glove box and delivered to the instrument without air exposure. Liquid electrolytes samples were soaked up by capillary tubes and loaded in the instrument.

3.4.3. Ion coupled plasma-atomic emission spectroscopy (ICP-AES)

Solubility of $LiPF_6$ was titrated by ICP-AES. Concentration of Phophorous (P) was measured instead of that of Li, which is due that Li atom is unable to be analyzed by ICP and the P atom corresponds to one to one molar ratio with Li. The 2.5 *M* $LiPF_6$ in DMC solution was poured into a syringe filter with 0.45 μm of pore size, and the P atoms of the resulting solution were titrated by ICP-Atomic emission spectrometer (730ES, VARIAN, Austrailia).

3.4.4. X-ray diffraction (XRD)

The crystal structures for LNMO, LTO, and graphite electrodes were determined by X-ray diffractometer (Brucker Corp., German.) The XRD results and its crystal structures of the used electrodes powder were displayed in Fig. 17.

3.4.5. Field emission-scanning electron microscopy (FE-SEM)

The morphology and particle size for LNMO, LTO, and graphite electrodes were observed by field emission-scanning electron microscopy (FE-SEM). The morphologies of the used electrodes powders were captured as seen in Fig. 18.

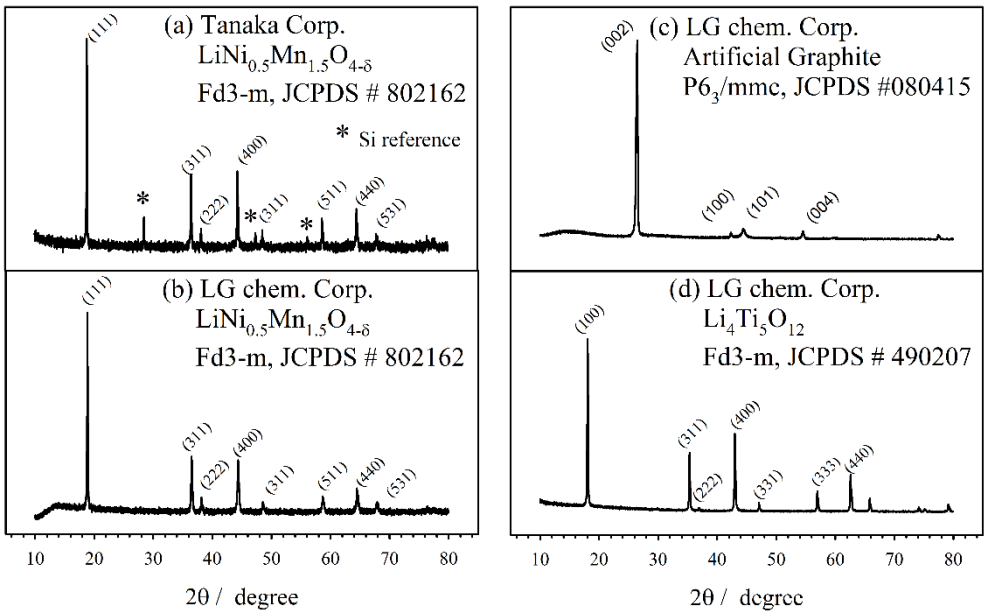

Figure 17. The XRD patterns of the used electrodes in this work. The crystal structures and JCPDS numbers are indicated in the inset. (a) Tanaka LNMO, (b) LG chem. LNMO (c) LG chem. artificial graphite, and (d) LG chem. LTO powders.

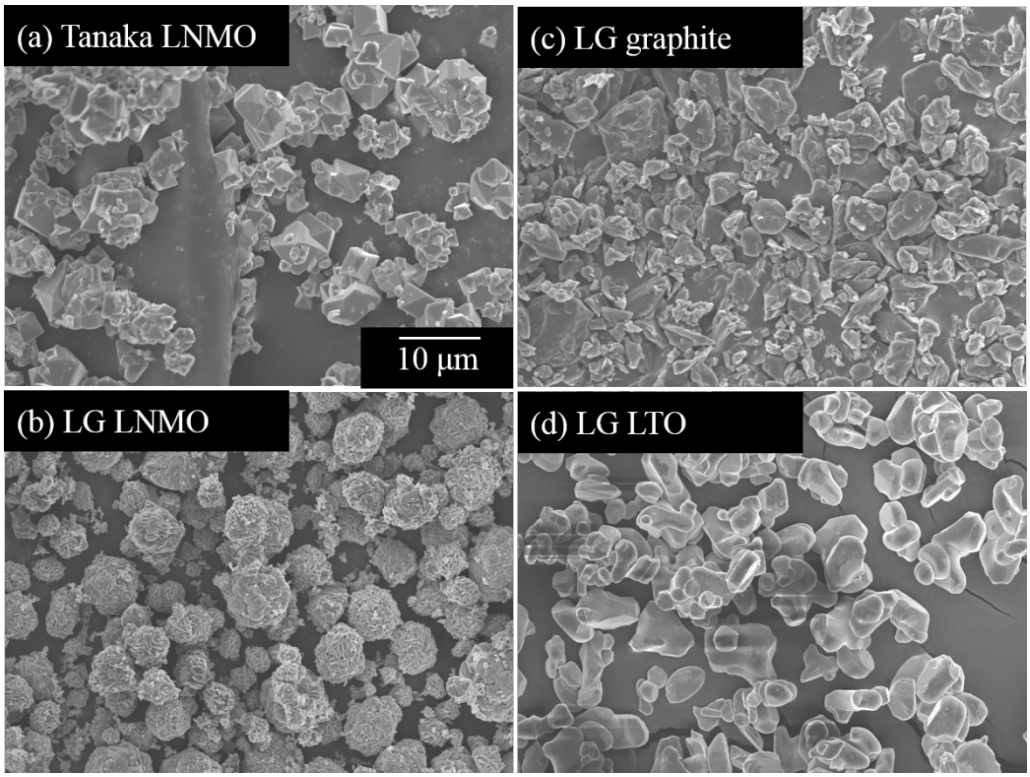

Figure 18. The FE-SEM images of the used electrodes in this work. (a) Tanaka LNMO, (b) LG chem. LNMO, (c) LG chem. artificial graphite, (d) LG chem. LTO powders.

4. RESULTS

AND DISCUSSION

4.1. Ion Transport Properties in Surface Films

4.1.1. Ionic conductivities of surface films

For investigating Li^+ ion conductivities of SEI and films, ac impedance spectroscopy was performed on graphite and LNMO electrodes after generating each interphase (Fig. 19). Fig. 19ab and 19cd show the impedance spectra obtained after 1^{st} charging and discharging, respectively. All the spectra show semi-circles, of which time constants are denoted in the spectra. Each of semi-circles have their usual meaning.[80,86,87] Because resistance depends on surface area and loading mass,[31,87] graphite and LNMO with similar BET (graphite; 3.17 $m^2 g^{-1}$, LNMO; 3.2 $m^2 g^{-1}$) were used and their loading mass on each current collector was regulated equally at 2.5 mg. After generating each interphase (after first charging), the impedance spectra show that the

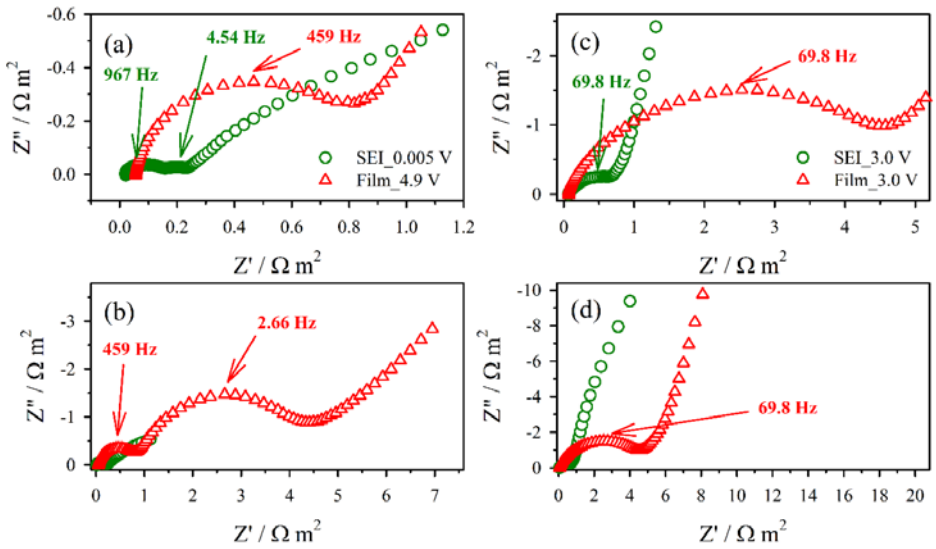

Figure 19. Ac impedance spectra (Nyquist plot) obtained from the graphite or LNMO/Li/Li three electrode cells: (a) (b); after the 1st charging, (c) (d); after the 1st discharging, (a)/(c); the magnified spectra of each (b)/(d).

interphase and charge transfer resistance for films are much larger than that for SEI (Fig. 19a and 19b). In addition, resistance depends on measured voltages,[46,88] and thus theresistances were measured equally same at 3.0 V (*vs.* Li/Li^+) after discharging. Even same at 3.0 V, the film resistance is much larger than that of SEI (Fig. 19c and 19d). Note that the charge transfer resistance is not observed at 3.0 V because Li^+ ion intercalation into both electrodes could not occurred. Ionic conductivity is inversely proportional to resistance,[31] and thus ionic conductivity of films is larger than that of SEI. This result is also observed from some previous reports.[89,90]

This results are not easily comprehensible well that thickness of films is estimated to be much thinner than that of SEI from some previous reports.[25,26,29,62,91] In order to estimate thickness of SEI and films, the deposited interphases on LNMO and graphite electrodes (after 1^{st} charging) were observed via the TEM images (Fig. 20). The carbonate-based electrolytes generate SEI on graphite electrode, which is much thicker than the deposited films on LNMO electrode (Fig. 20ad). Their thickness difference is also confirmed from elemental mapping, in which the position of interphase components and active materials can be identified more clearly. From this elemental mapping and scale bar, the thickness of SEI is estimated to be from 100 to 125 nm whereas that of film is estimated to be 15 nm on each electrode. The TEM images show

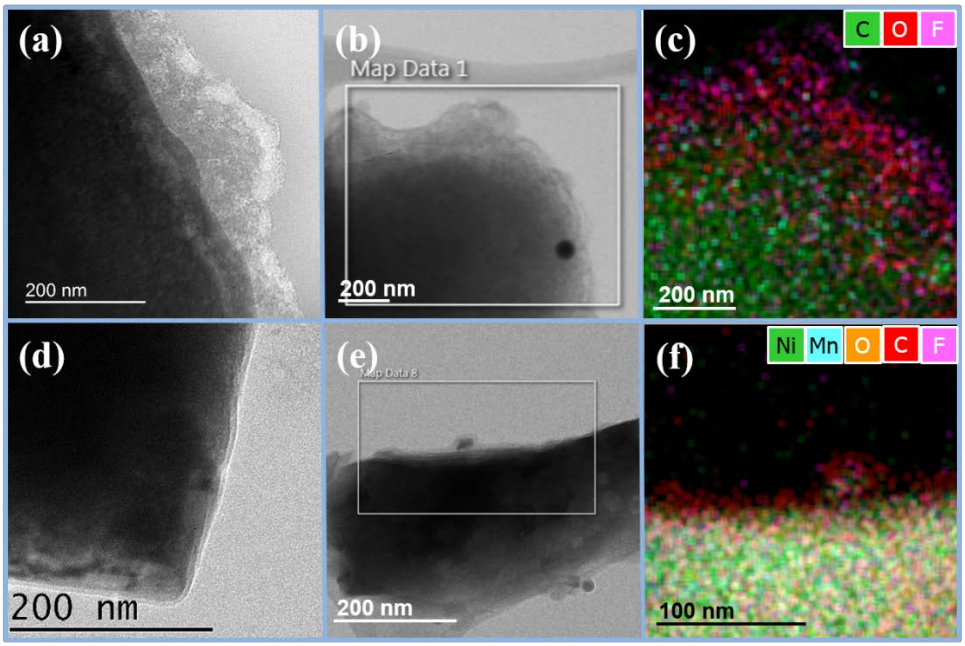

Figure 20. TEM images for interphases on lithium-ion battery electrodes after the 1st charging. (a-c); graphite electrode, (d-f); LNMO electrode, (c) (f); EDS mapping of (b) (e). The red, pink dots represent atoms of interphases and the green, blue dots represent active materials, respectively.

that film is much thinner than SEI. Note that the measured thickness depends on many factors like instruments, position of the surface, or electrode.[25,26,29,62,91] For example, thickness of the upper organic layer in SEI was measured at 480 nm on HOPG (Highly oriented pyrolytic graphite) electrode with variation whereas the same layer was measured even at 5 nm on Cu electrode from previous reports.[25,26]

The interphases-deposited amounts and their impedance were quantitatively scrutinized by using EQCM and ac impedance spectroscopy (Fig. 21). In order to monitor the two interphases deposition only, the inert metal electrodes with Li (Cu for electrochemical reduction, Pt for electrochemical oxidation) were introduced to be assembled with Li counter and Li reference. When Cu-quartz electrode is linearly sweep from OCV (3.2 V) to 0.005 V, the deposited mass of SEI is 3.17 μg cm^{-2} (Fig. 21a). On the other hand, when Pt-quartz electrode is linearly sweep to 5.2 V, the deposited mass of films is 0.55 μg cm^{-2} (Fig. 21b). This results ascertain that the amount of the generated SEI is larger than that of films in same charging condition. Interestingly, however, the obtained impedance spectra and the fitted resistances confirm that films have larger resistance compared to SEI (Fig. 21cd). Ac impedance was measured after generating the interphases by linear sweep and following to rest for 30 min for the electrodes to reach quasi-open circuit voltage (QOCV). The spectra show one semi-circle, such that they are fitted by using the

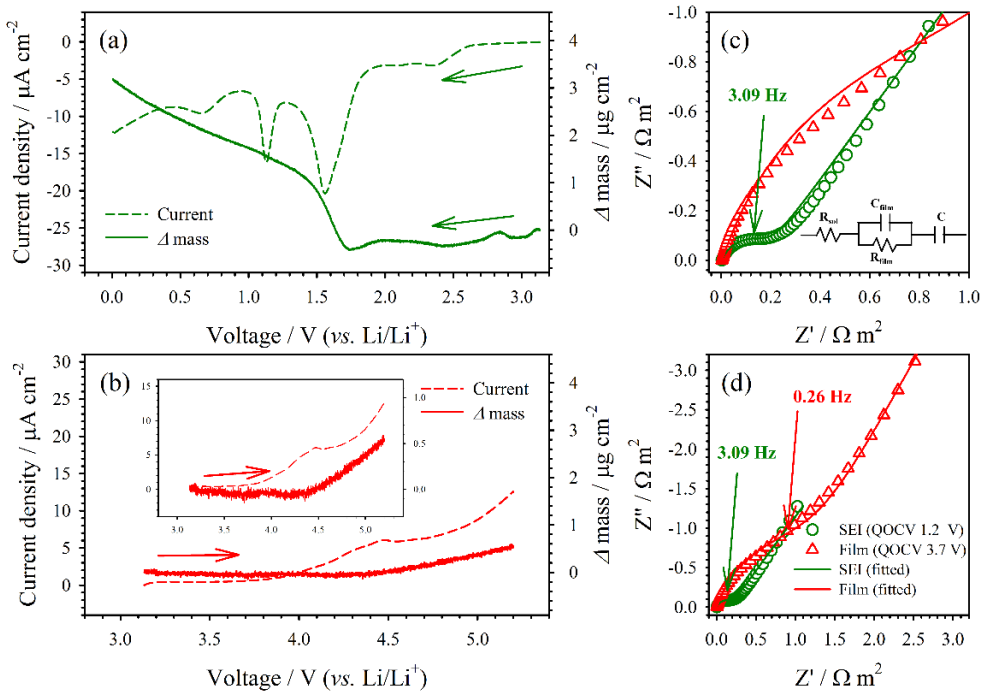

Figure 21. EQCM measurements and ac impedance spectra. EQCM results: (a); mass increase of SEI generated on the Cu-quartz electrode via linear sweep voltammetry to 0.005 V, (b) mass increase of films generated on the Pt-quartz electrode via linear sweep voltammetry to 5.2 V, reference and counter electrode; Li metal, scan rate = 1.0 mV s^{-1}. (c) (d); ac impedance spectra obtained from the Li/Li/Cu or Pt three electrode cells after one linear sweep at 1 mV s^{-1}. (c); the magnified spectra of (d).

equivalent circuit shown in the inset (Fig. 21c). Note that the final capacitance term is added after interphase resistance rather than charge transfer and Warburg, because the inert metal electrodes with Li were introduced.[92] The fitted resistances are 0.34 Ω m^2 for SEI, and 2.2 Ω m^2 for films. Ionic conductivity is inversely proportional to resistance,[31] films have poorer ionic conductivity than SEI. Interphase resistances per the deposited mass for the two interphases are 0.11 Ω m^2 $g_{interphase}^{-1}$for SEI and 4.0 Ω m^2 $g_{interphase}^{-1}$for films. It shows more noticeably that ionic conductivity of films is much poorer compared to that of SEI.

4.1.2. Surface films components

These results are a little bit confusing and chaotic. If the components of the two interphases are same, their ionic conductivities should be proportional to each their thickness. It can thus be assumed that components for the two interphases are different, and thus Li^+ ion transport behaviors are different between the two interphases. In order to unravel the origins for the property difference between SEI surface films on negative electrodes and surface films on LNMO positive electrode, the chemical compositions were compared for the two films. Fig. 22 compares the depth-profiling Li 1s XPS data for the two surface films. Fig. 11 illustrates that a surface film deposits on the graphite surface

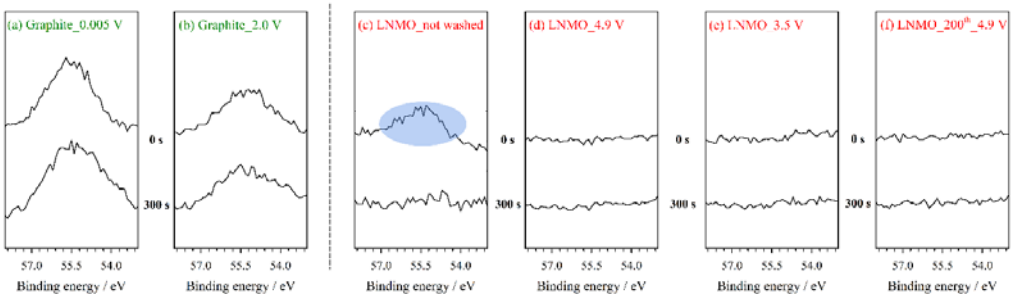

Figure 22. The Li 1s depth-profiling XPS spectra obtained from the SEI-deposited graphite and the SPI-deposited LNMO electrodes. The samples were washed with DEC except for (c). (a) (b); graphite electrodes after the 1st charging (0.005 V) and discharging (2.0 V), (c); LNMO electrode without washing after the 1st charging, (d) (e); LNMO electrodes after the 1st charging (4.9 V) and discharging (3.5 V), (f); LNMO electrode after the 200th charging. The etching time (0 s and 300 s) is indicated in the inset.

during the first lithiation period, and Li species are populated evenly across the film depth. These Li species remain in the film even after de-lithiation up to 2.0 V (Fig. 22b). Given that the samples for Figs. 22a and 22b were washed with DEC, one can assume that the Li species are so strongly bound to the film matrix that they are not leached out during the washing period. Li species are also detected in the surface film deposited on the LNMO electrode by oxidative electrolyte decomposition (Fig. 22c), but they are easily removed from the surface film (Figs 22d and 22e) with washing. Such an easy removal is also observed from a thicker surface film, which was prepared by cycling 200 times (Fig. 22f). Either SEI or films, the two interphases are significantly generated when each electrode is electrochemically charged. Fig.23 shows what situations occur in electrochemical cells during charging. When electrochemical cells are charged, electrons leave from positive electrode to negative electrode through external circuits. During charging, electrons are accumulated on negative electrodes, and depleted on positive electrodes. Solvents of electrolytes are electrochemically reduced to generate anions on negative electrodes, whereas solvents are electrochemically oxidized to generate cations on positive electrodes. In order for these charged intermediates to be precipitated on each electrode in the forms of insoluble solid phase, each charged ion should meet the charge balance with their counter charge to be deposited in the insoluble salt forms (neutral species). If they don’t

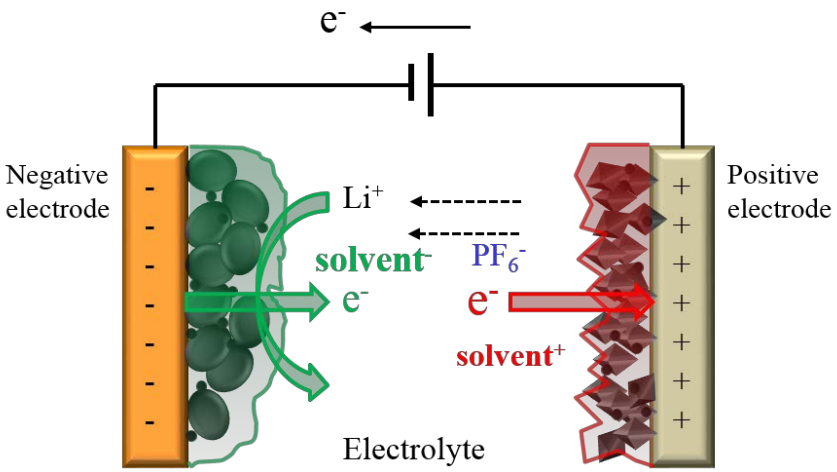

Figure 23. Electrochemical charging situation for generating the two surface films on both negative and positive electrodes.

satisfy the charge balance, the charged intermediates would be re-dissolved into electrolytes. In detail, anions evolved on negative electrodes are precipitated with their counter positive charge Li^+ ions, and thus which are embedded in the solid structure of SEI. In contrast, cations derived from positive electrodes cannot be precipitated with their same charge Li^+ ions due to their charge repulsion. In this respect, it can thus be assumed that the counter charge of cations would be salt anions in electrolytes. This will be discussed in the next XPS spectra (Fig. 24).

The C 1s, O 1s, F 1s, and P 2p XPS spectra were investigated to compare which components are different between the two interphases (Fig. 24). The electrodes were prepared without conducting agents and binder. The LNMO powders were embedded on gold (Au) plates, and the graphite powders were pressed in nickel (Ni) foams. The fitted binding energies for films or SEI components are summarized in the table 7.[63,93-99] When carbonates are electrochemically decomposed, single or double carbon-oxygen bonds (Fig. 24 blue line) are generated on both electrodes. As previous mentioned, anions evolved on negative electrodes combine with their counter charge Li^+ ions, and thus lithium alkyl carbonates ($ROCO_2Li$) are deposited. In contrast, cations evolved on positive electrodes cannot combine with the same charge Li^+ ions so that lithium alkyl carbonates are not deposited, but polyethylene oxides (-C-O-) are generated. All the two interphases have organic layers, however, SEI

Table 7. Binding energies (in eV) for fitting XPS spectra.[63,93-99]

C 1s		O 1s		F 1s		P 2p	
Li_xC_6	283.6	Li_2O	528.8	LiF /metal-F	685.1	$OP(OR)_3$	134.0
Hydrocarbon	285.0	Lattice O	530.3	PF_yO_z	686.6	PF_yO_z	136.0
C-O / $ROCO_2Li$	287.0	Li_2CO_3	531.8	PF_6^-	688	PF_6^-	137.8
O-C=O	287.8	C=O	532.0				
C=O	289.1	C-O	533.5				
Li_2CO_3	290.3						

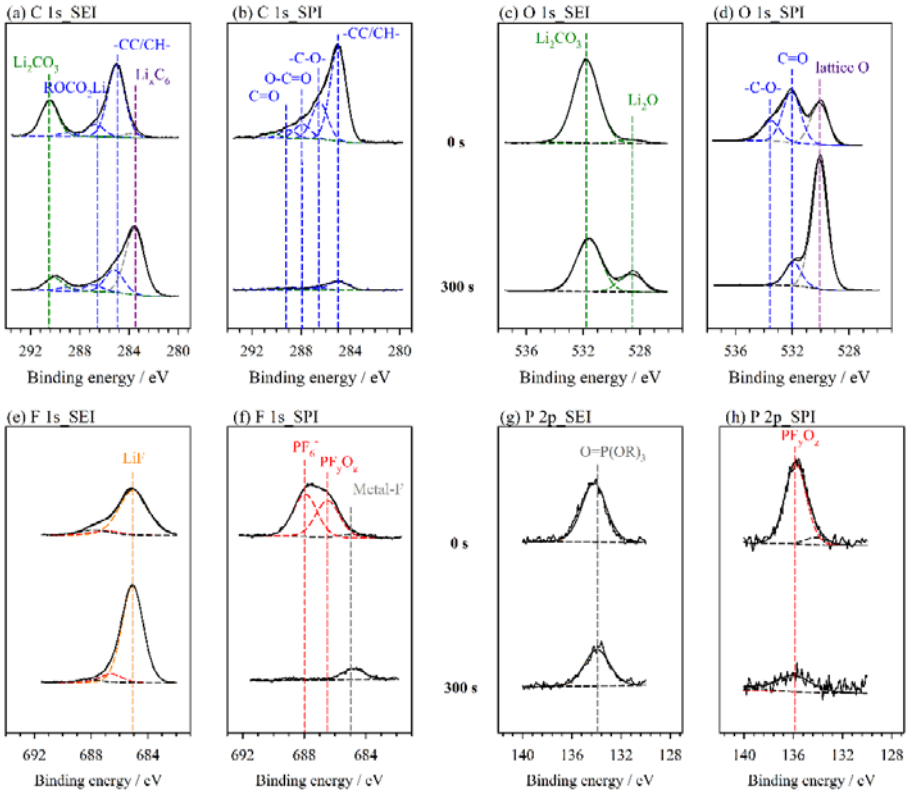

Figure 24. C 1s (a, b), O 1s (c, d), F 1s (e, f), and P 2p (g, h) depth-profiling XPS spectra obtained from the SEI-deposited-graphite (0.005 V) and SPI-deposited-LNMO (4.9 V) electrodes. All samples were washed with DEC after being charged once. The etching time is indicated in each panel. The spectra were fitted using the binding energy values listed in Table 7.[63,93-100]

consists of lithium terminated organic structures, whereas films are composed of cationic polyethylene oxides (organic components). Next, it should be considered what component is the counter charge for the cations generated on positive electrodes. If these cations don't satisfy charge balance with anions, they would be re-dissolved into electrolytes. In order to deposit in the insoluble solid forms, only the neutral salt-formed solids should deposit on electrodes.

The counter anions must be salt anions in electrolytes, which are confirmed by the F 1s, and P 2p XPS spectra. The salt anion-involved species, hexafluorophosphate anion (PF_6^-) or PF_yO_z, are observed much richer in films than SEI (Fig. 24 red line). The polymerized cation intermediates are combined with this salt anion by ionic interaction. Resultantly, films were composed of the anion contained cationic organic layers (Fig. 24c). Note that lithium fluoride (LiF) are usually observed at the relatively high-voltage (> 0.25 V) on graphite electrodes, while it does not populated in the films on LNMO electrode.[92] In addition, SEI also consists of the solvent-derived inorganic species, Li_2CO_3 and Li_2O usually in bottom layer of SEI,[24,26,27] which are significantly observed in the XPS spectra of SEI (Fig. 24 green line). Interestingly, these carbonate-derived inorganic species are not confirmed at all in films. The peak at 532.0 eV (O 1s) in films was assigned to organic carbonyl group (-C=O) rather than carbonate anion (CO_3^{2-}), which is closely near

at 531.8 eV (O 1s) of in SEI. Because the peak at 290.3 eV (C 1s) of carbonate anions ($\underline{C}O_3^{2-}$) are not observed at all in films, whereas that are significantly confirmed in the SEI. Accordingly, it is more reasonable that the 532.0 eV (O 1s) in films are synchronized with the organic carbonyl group (-O-$\underline{C}$=O or -$\underline{C}$=O) at 278.8 and 289.1 eV of the C 1s spectra.

These two interphases generations could be also understood from the previous suggested mechanisms for electrochemical reactions of carbonates.[18,36,79,101] When carbonates are electrochemically reduced with one electron, minus one valance of anions polymerize by themselves with one Li^+ ion to generate lithium alkyl carbonates ($ROCO_2Li$) (Fig. 25). When carbonates are electrochemically reduced with two electrons, minus two valences of anions are precipitated with two Li^+ ions to form lithium carbonate (Li_2CO_3) (Fig. 25). Lithium carbonate (Li_2CO_3) could be further reduced to be lithium oxide (Li_2O): $Li_2CO_3 + 2Li^+ + 2e^- \rightarrow 2Li_2O + CO$.[29] Lithium fluoride (LiF) is generated as a result of the two-electron reduction of lithium hexafluorophosphate ($LiPF_6$): $2Li^+ + 2e^- + LiPF_6 \rightarrow 3LiF + PF_3$.[29] In short, the formation of the SEI components can be explained by the electrochemical reductions of the solvent and the Li salt. Peled suggested that these SEI components are deposited in a heterogeneous mosaic-type structure on the graphite or lithium metal electrode.[23] Resultantly, SEI consists of the bottom of inorganic layer (Li_2CO_3, Li_2O, and LiF) and the

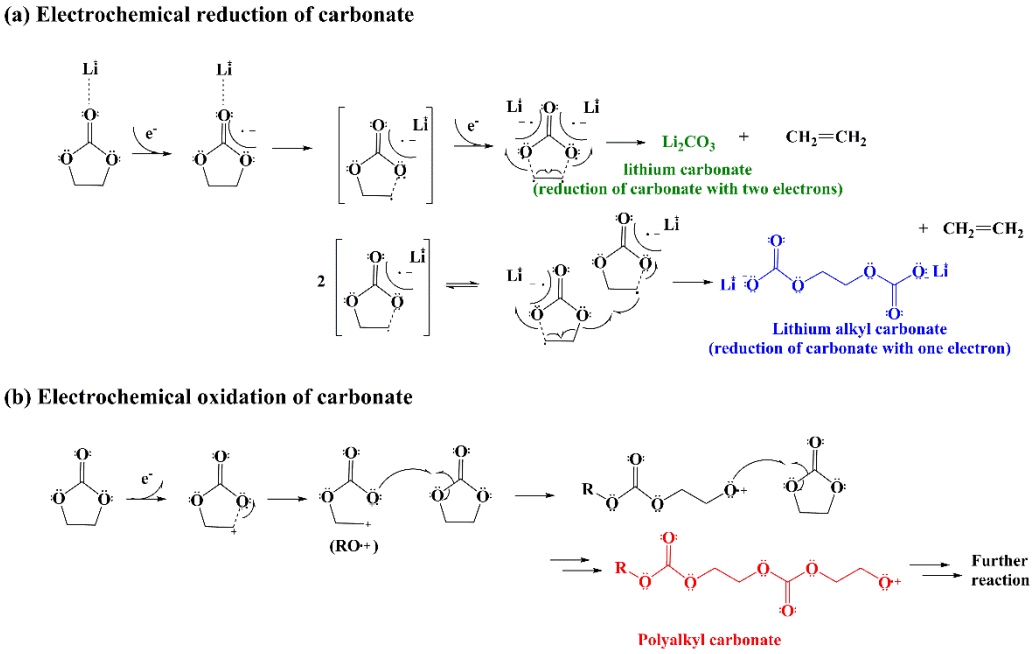

Figure 25. Electrochemical reduction and oxidation mechanisms of carbonates. (a); electrochemical reduction of carbonate, (b); electrochemical oxidation of carbonate.

upper of organic layer ($ROCO_2Li$). In contrast, when carbonates are electrochemically oxidized, the oxygen-terminated radical cations are generated to polymerize with adjacent carbonates, and thus only organic components evolves on positive electrodes (Fig. 25). Unfortunately, the accurate termination reaction mechanisms for the radical cation have not been suggested yet, however, it seems very likely that the organic layer on LNMO electrode carries positive charge. This is because the high population of salt anion and absence of positive Li^+ ions are confirmed from the XPS spectra. Unlike SEI, cationic organic layer evolves on LNMO electrodes. As a result, it is suggested that the films structure as the salt anion-contained cationic organic structures.

The XPS data (Figs. 24a and 24d) also inform the thicknesses of the SEI on graphite and the film on LNMO electrode. The spectra obtained without etching (0 s) provide information on the top-most surface region. Fig. 24a reveals that the C 1s photoelectrons emitted from graphite (Li_xC_6) are negligible, but are appreciable after etching for 300 s (purple line). This means that the surface film on the graphite is so thick that C 1s photoelectrons are hardly emitted from the graphite (Li_xC_6). However, the O 1s spectra shown in Fig. 24d illustrate that the film on the LNMO electrode is much thinner than the SEI. In particular, the signal from the O 1s photoelectrons emitted from the lattice oxygen of LNMO is substantial even before etching (etching time = 0 s, purple line). All these

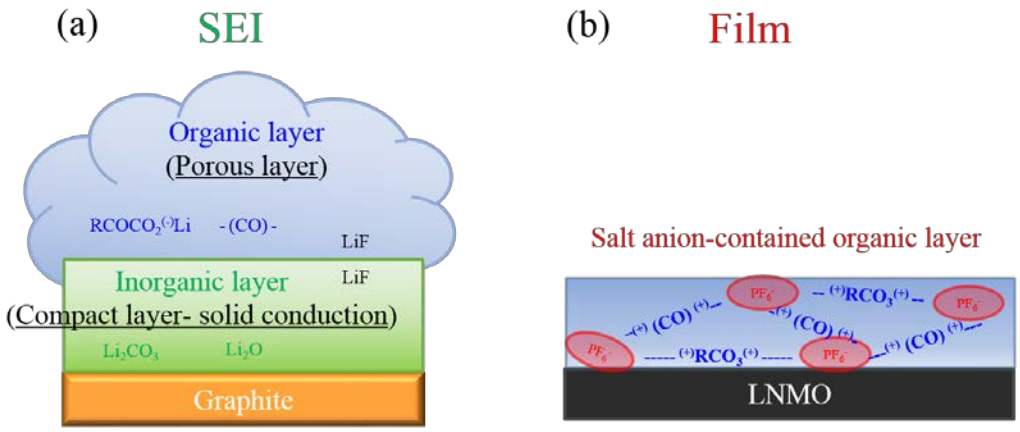

Figure 26. Diagrams of solid structures for the two surface films. (a); SEI on graphite electrode, (b); solid film on LNMO electrode.

components are structures results are summarized in Fig. 26. SEI consists of the upper organic layer and the bottom of inorganic layer, whereas film on LNMO electrode is formed in anion-contained organic layer. In short, the film layer does not contain solid Li salt-like components (Li_2CO_3 and Li_2O), which is densely packed onto the nearest surface of graphite electrode.[26] The absence of these components and existence of thin polymer chains similar with the upper porous organic layer in SEI: these two features, raise suspicion, whether the surface film deposited on LNMO electrode is indeed passivating or allows permeability, unlike SEI on graphite electrode. Hence, it is suspected that Li^+ ions reside inside the film layer in solvated forms along with solvation components such as EC. This is reasonable, because Li^+ ions migrate in this non Li^+-solid structure to access to the LNMO electrode which reversibly reacts after the solid film deposition for long-term cycles as seen in Fig. 27.

4.1.3. Permeability of surface film on LNMO electrode

In order to observe permeable property, it is performed on depth analysis through time of flight-secondary ion mass spectrometry (TOF-SIMS) by separating the film-generating electrolyte and wetted electrolyte in the solid film on LNMO electrode. First, LNMO electrode was charged to 4.9 V (*vs.* Li/Li^+) with 1.3 *M* $LiPF_6$ in EC:EMC:DEC = 3:2:5 (*v/v/v*) (film-

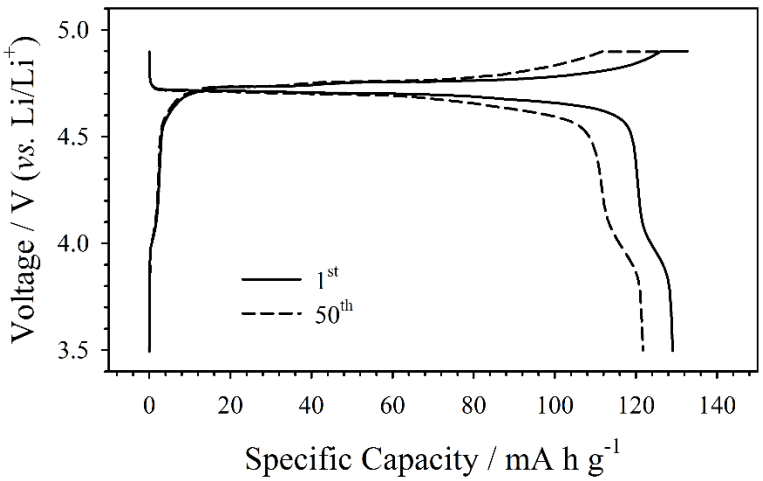

Figure 27. The galvanostatic charging/discharging voltage profiles for LNMO electrode. The cycles are indicated in the inset.

forming electrolyte). The charged LNMO electrode washed with DEC and re-wetted in 1.3 *M* $LiClO_4$ in four-deuterated EC (EC-D_4):DEC = 3:7 (*v/v*) (wetted electrolyte in the pre-generated solid film) for 5 min. The wetted LNMO electrode is analyzed by time of flight-secondary ion mass spectrometry. Except for the empty inverse triangles in Fig. 28b: the washed LNMO electrode, all intensities are for the final re-wetted LNMO electrode. The PF_6^- (from film-forming electrolyte) is noticeably observed at initial etching time (Fig. 28a inverse blue triangle), which represents the pre-generated solid film on the LNMO electrode, because the wetting electrolyte does not include PF_6^-. After washing with DEC, the $^6Li^+$ intensity is not observed at all as seen in Fig. 28c and 4d of the previous XPS spectra. After wetting by 1.3 *M* $LiClO_4$ in four-deuterated EC (EC-D_4):DEC = 3:7 (*v/v*), Li^+ ion and solvation molecule (deuterium of EC-D_4) are observed in the pre-generated film (Fig. 28b green square and red triangle). This supports that Li^+ ions reside inside the film layer in solvated forms along with solvation components such as EC; consequently, Li^+ ions are not strongly bound to the film matrix and are easily removed by washing as seen in Fig. 22c and 22d. This is because electrolyte oxidation generates cations, which does not provide ionic interaction toward Li^+ ions. Due to the solid film components and wetted electrolyte, the LNMO electrode is exposed in the latter etching time (Fig. 28a black circle). Notably, it was reported in the literature that non-Li^+

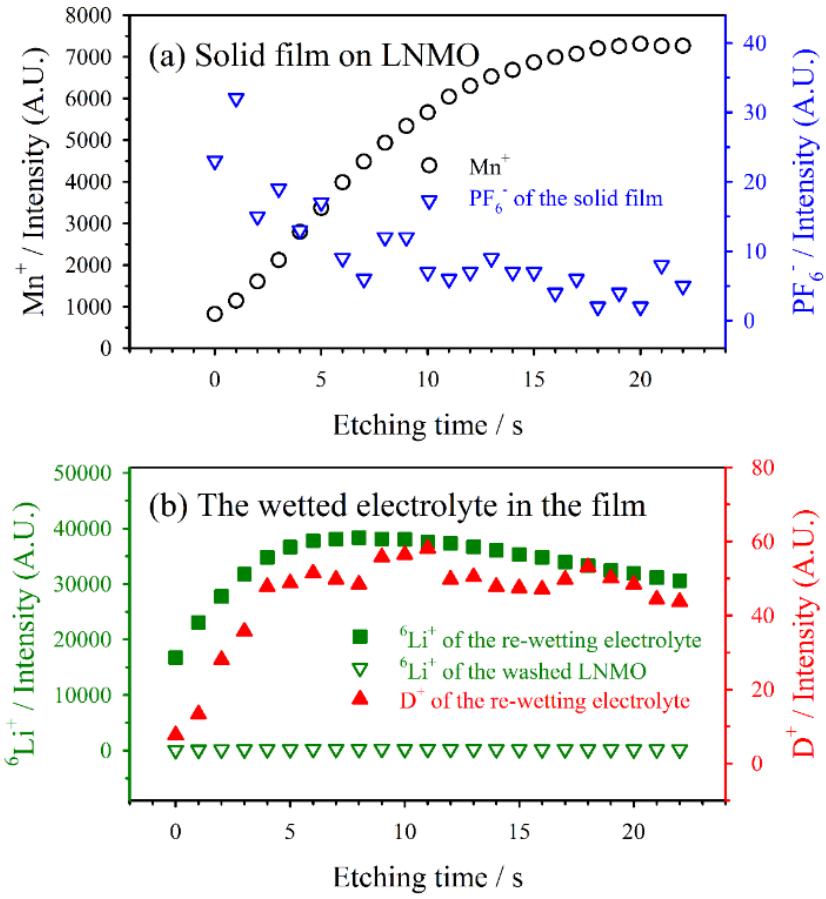

Figure 28. TOF-SIMS depth profiles for the surface film derived from the film-generating electrolyte (1.3 *M* $LiPF_6$ in EC:EMC:DEC = 3:2:5 (*v/v/v*)) on LNMO electrode by wetting the film-wetting electrolyte (1.3 *M* $LiClO_4$ in EC-D_4:DEC =3:7 (*v/v*)). (a); Mn^+ of LNMO electrode and PF_6^- from the film-forming electrolyte, and (b); $^6Li^+$ ions and solvent (EC-D_4) from the wetting electrolyte. All intensities are for the final re-wetted LNMO electrode except for the washed one (green inverse triangle in (b)) by DEC.

component like salt anion are not allowed to be immersed into the deeper region of SEI through TOF-SIMS techinique.[26,27] The permeable property of film on LNMO electrode is consistent with those of the solid permeable interface (SPI) referred to by Edström and her colleagues.[28,29] Hence, in this report, we refer to the surface films on the positive electrodes as 'SPI', whereas those on the negative electrode are conventional SEI.

In order to investigate permeable depth, the nickel(Ⅱ)-1,4,8,11-tetraazacyclotetradecane tetrafluoroborate (Ni(cyclam)$[BF4]_2$, Ni(Ⅱ)-cy, inset of Fig. 15) was introduced to confirm its reversible reaction on the two interphases-deposited electrodes. The Ni(Ⅱ)-cy in a Li^+-supporting electrolyte (1.3 *M* $LiPF_6$ in EC:EMC:DEC=3:2:5 (*v/v/v*)) reacts reversibly at 1.5 V (*vs.* Li/Li^+, within cut-off range of negative electrodes) and 4.1 V (within cut-off rage of positive electrodes) on the clean glassy carbon rod electrodes (Fig. 29a black line). Thus, this redox couple could be indicator for verifying penetration of electrolyte components into the both interphases. SEI and SPI had been pre-generated on glassy carbon electrode by cyclic voltage sweep to each cut-off voltage with the Ni(Ⅱ)-cy-free electrolyte and the interphases-generated glassy carbon electrodes were followed to re-soaked in the 0.01 *M* Ni(Ⅱ)-cy-added electrolyte. On the clean glassy carbon electrode, the Ni(Ⅱ)-cy reacts reversibly both at

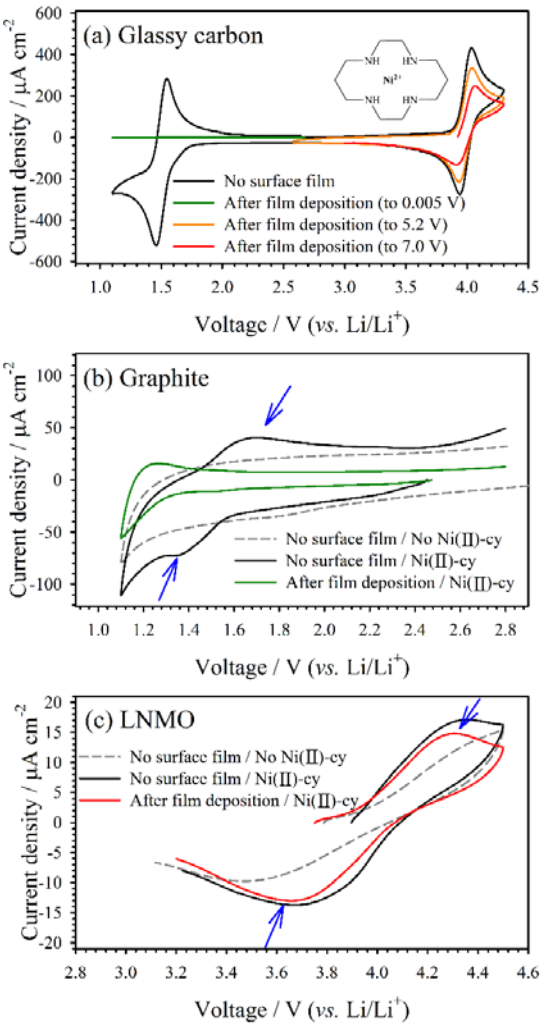

Figure 29. Cyclic voltammograms obtained from 0.01 *M* nickel(II)-1,4,8,11-tetraazacyclotetradecane tetrafluoroborate (Ni(cyclam)[BF_4]$_2$, Ni(II)-cy) dissolved in 1.3 *M* $LiPF_6$ in 3:2:5 (*v/v/v*) EC:EMC:DEC at a scan rate of 50 mV s^{-1} in a three-electrode cell (counter and reference electrodes are Li metal) on the following electrodes: (a) glassy carbon, (b) graphite, and (c) LNMO. The structure of Ni(II)-cy is shown in panel (a).

low an high-voltage region (1.5 and 4.1 V). After generating SEI to 0.005 V, the Ni(Ⅱ)-cy does not react at all on the SEI-deposited glassy carbon electrode (Fig. 29a green line). Hence, SEI is significantly passivating. Interestingly, however, after forming SPI to 5.2 V, the peak currents do slightly decrease, but the Ni(Ⅱ)-cy still reacts reversibly at 4.1 V (Fig. 29a orange line). In order to convince the permeability of SPI more clearly, SPI were generated to 7.0 V even for the much thicker SPI than the 5.2 V formation. Even when the surface film is deposited up to the extremely high-voltage 7.0 V, the resulting surface film still allows permeation of the redox indicator. The decreased current density and slight over-potential for the SPI generated to 7.0 V than 5.2 V are due to decreased porosity or increased thickness. Electron tunneling probability exponentially decays to distance from electrodes by the following equation: $\text{electron tunnueling} \propto e^{-\beta d}$ (d: distance from electrode),[31] and thus electron tunneling is significant at just above the nearest surface of the electrodes. These results strongly supports that the Ni(Ⅱ)-cy redox indicator easily approaches near at the glassy carbon electrode surface with passing into the electro-oxidatively decomposed surface film.

The permeabilitiy of the two surface films is also confirmed in the active materials (Fig. 29b and 29c). The three electrode (Li-counter, Li-reference) beaker type cells were assembled, and graphite or LNMO

electrodes were charged and discharged to 3.0 V with 9 mL of the Ni(Ⅱ)-cy-free electrolyte. After generating the two interphases, 1 mL of the 0.1 *M* Ni(Ⅱ)-cy-added electrolyte is added in the beaker cells to tune the same concentration (the 0.01 *M* Ni(Ⅱ)-cy-added electrolyte) of the previous glassy carbon electrode vial cells. The beaker cells are followed to cyclic voltage sweep with 50 mV s^{-1} scan rate. In addition, some cyclic voltage sweeps on the clean active materials were monitored for the Ni(Ⅱ)-cy-added or not to calibrate the current scale of the Ni(Ⅱ)-cy reversible reaction. The Ni(Ⅱ)-cy reacts reversibly on the clean graphite electrode at 1.5 V (Fig. 29a black line) whereas it does not react at all after generating SEI on the graphite electrode (Fig. 29b green line). In contrast, the Ni(Ⅱ)-cy reacts not only reversibly on the clean LNMO electrode (Fig. 29c black line), but still on the SPI-deposited LNMO electrode (Fig. 29b red line). It is certainly confirmed that SEI is significantly generated to be densely packed in the initial cycling, but SPI is loosely deposited to allow penetration of electrolyte components. Considering the structures of the two surface films, the summary is as the follows (Fig. 30). The Ni(Ⅱ)-cy redox couple could pass only into the upper organic porous layer of SEI on graphite electrode, which is not appreciable for electron tunneling. In contrast, the redox indicator easily

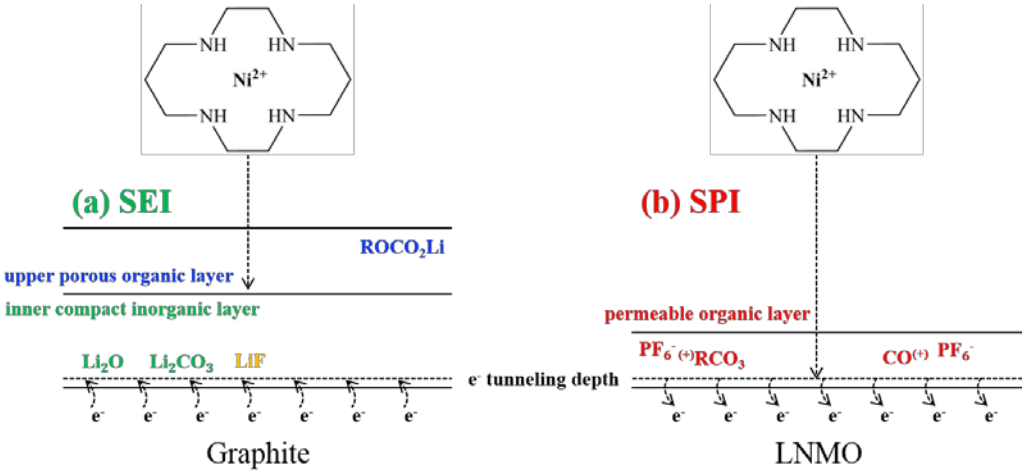

Figure 30. Schematic drawing for accessibility of the Ni(Ⅱ)-cy redox probe in the two surface films: (a) SEI and (b) SPI.

access to the nearest surface on LNMO electrode, which is electron tunneling is considerable, by high permeability of organic layer in SPI.

This strongly supports why the Coulombic efficiency of LNMO electrode is lower than that of graphite electrode. The permeability of surface film and easy accessibility of electrolytes are one of major factors for the low Coulombic efficiency of LNMO electrodes. Even though graphite electrodes react with Li^+ ions (<0.25 V *vs.* Li/Li^+) below the electrochemical stability windows of the carbonate-based electrolytes (<1.0 V),[7] the initially deposited-SEI in the first cycle is significantly electron insulating and passivating to prevent further electrolyte decomposition. Thus, its Coulombic efficiency reaches about 99.8 % after the 1^{st} cycle (88.0 %) (Fig. 31a). The LNMO high-voltage positive electrode of which working potential (>4.6 V) is beyond electro-oxidation limit (<4.3 V) of the carbonate-based electrolytes,[7] however, represents that its Coulombic efficiency is maintained at about 98.0 % even at 25℃ (Fig. 31a). The XPS spectra confirms that LNMO electrodes suffer from further electrochemical oxidation of electrolytes (Fig. 13bcde). In initial cycling, the lattice oxygen (530.3 eV) of the LNMO electrode is remarkably observed without Ar^+ sputtering (Fig. 31c). During cycling, the lattice oxygen peak becomes blurred at the top-most level, and it must be etched to reveal it noticeably (Fig. 31de). Even at the 100^{th} cycle that films are significantly generated, the films still grows continually to the

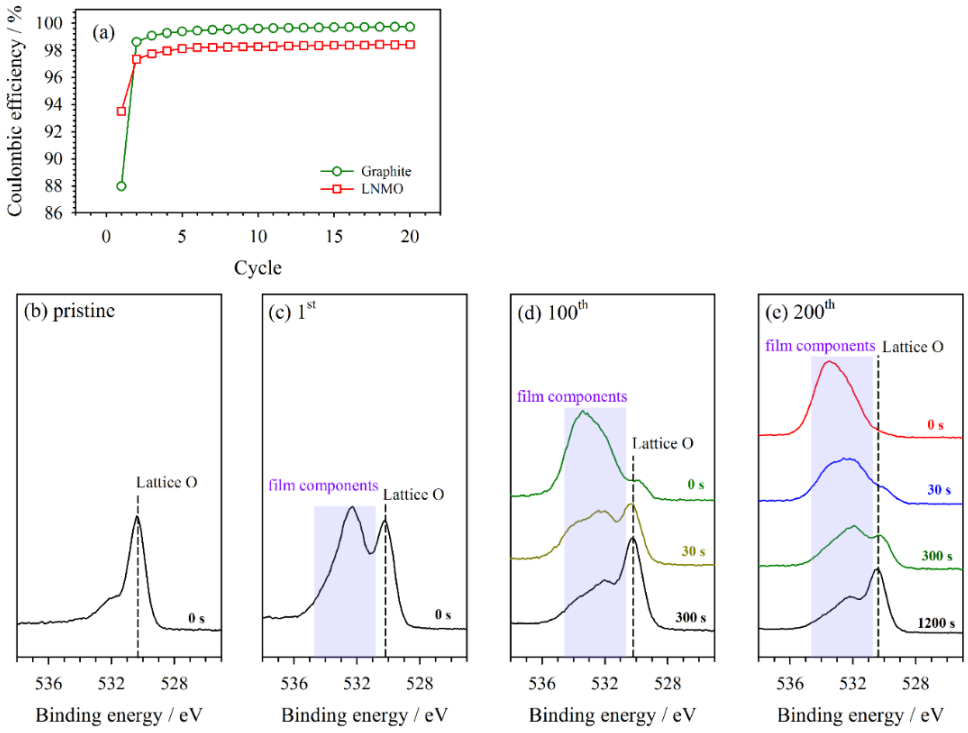

Figure 31. Coulombic efficiency of active materials and films growth of LNMO electrode. (a) Coulombic efficiency of graphite, LCO, and LNMO electrodes at 25℃. (b) (c) (d) (f); films growth of the LNMO electrodes during cycling at 25℃. The cycle numbers are in the inset.

200th cycle (Fig. 31e). It is thus be ascertained that the initially deposited-films are loosely deposited on LNMO electrode to allow permeablity unlike compact SEI on graphite electrodes.

4.1.4. Li^+ transport properties in SPI

Li^+ ion transport property of SPI is also not free from this permeability. In order to examine this influence, ac impedance experiments were conducted by changing ionic conductivity of wetting electrolytes for the two surface films. Generally, ionic conductivity of electrolyte solution is determined free ion concentration and ion mobility: $\kappa = F\sum_i |z_i| C_i u_i$ (F; Faraday constant, z_i; charge of free ion, C_i; concentration of free ion, u_i; mobility of free ion), and the ion mobility (u) suffers from frictional drag force by viscosity of the solutions: $u_i = \frac{|z_i|e}{6\pi\eta r}$ (η; viscosity, r; ion radius).[31] In detail, ionic conductivity is optimized at 1.0 *M* of $LiPF_6$ in EC:DMC = 5:5 (*v/v*) solvent composition;[82] lower free ion concentration cause it in decrease below 1.0 *M*, and viscosity increment lead to it low beyond 1.0 *M*. These tendencies are described in Fig. 32g. In this experiment, it is tested that this behaviors are reflected to film resistances for the two surface films. First, after two surface films were charged fully and discharged to SOC 50 on both graphite and LNMO electrodes with 1.3 *M* $LiPF_6$ in EC:EMC:DEC = 3:2:5 (*v/v/v*), the films-

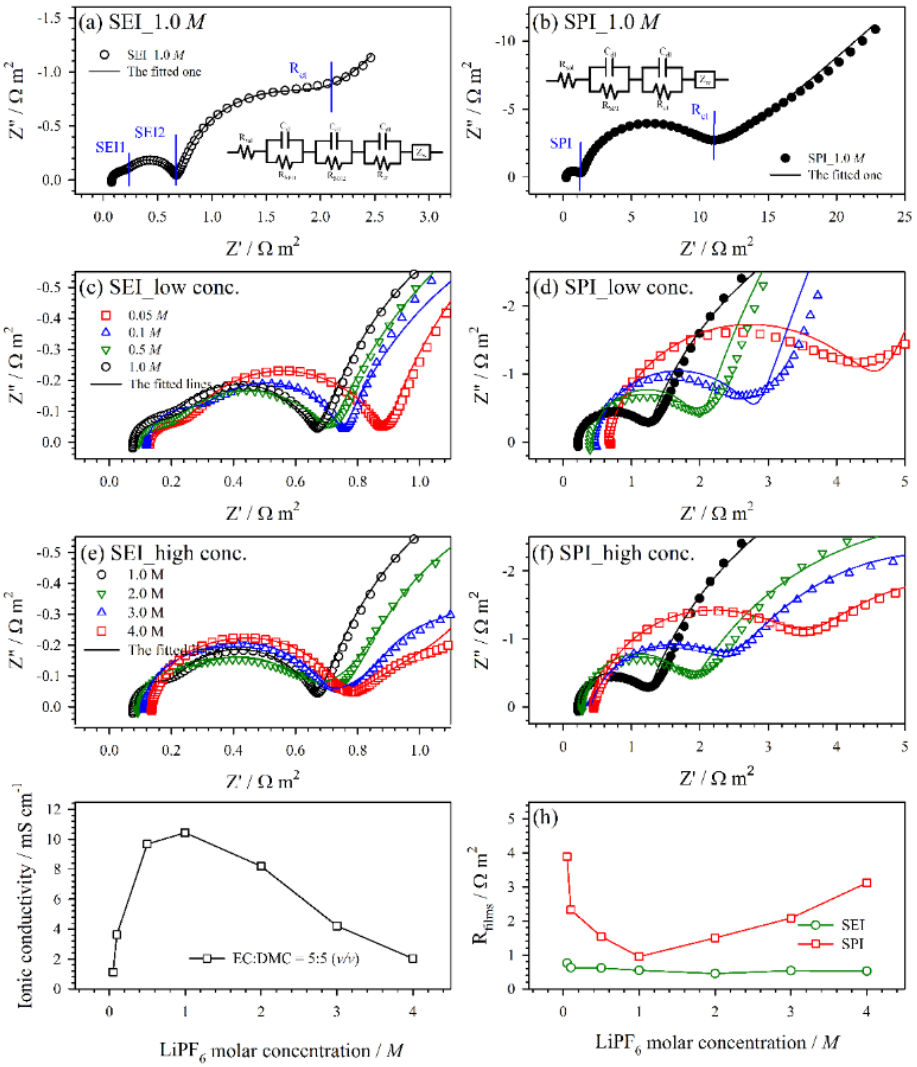

Figure 32. Ac impedance spectra and their fitting results for the SEI and SPI obtained as a function of $LiPF_6$ concentration in the electrolyte solution. (a), (c), and (e); Nyquist plots for SEI on graphite electrodes, (b), (d), and (f); Nyquist plots for SPI on LNMO electrodes. (g); Ionic conductivities of the electrolyte solutions as a function of $LiPF_6$ concentration in EC:DMC = 5:5 (*v/v*). (h); The film resistances for SEI and SPI as a function of $LiPF_6$ concentration in EC:DMC = 5:5 (*v/v*).

deposited electrodes were washed with DEC and followed to be re-assembled with various $LiPF_6$ concentrations in fixed solvents composition (EC:DMC = 5:5 (*v/v*)). The observed semi-circles in each panel of Fig.32 have their usual meaning (Fig. 32ab).[80,86,87], and notably, SEI layers could be fitted separately in several semi-circles due to its multilayer components (Fig. 32a).[80,81] As is seen in Fig. 32c and 32e, SEI resistances are constantly preserved regardless of ionic conductivities of the wetting electrolytes. This ascertains that ion concentration and the ion mobility of Li^+ ion are fixed, once SEI is generated. It can be accounted for the compactness and solid Li^+-conduction for the SEI solid matrix. In contrast, SPI resistances depend on the ionic conductivities of the wetting electrolytes. When the pre-generated SPI is wetted below or over 1.0 *M* of $LiPF_6$ in EC:DMC = 5:5 (*v/v*) composition, the film resistances become larger. Li^+ ions are immersed in SPI in a form of solvated state by EC (Fig. 28), free ion concentration and ion mobility of electrolytes have an effect to the film resistances. It should be reminded that ionic conductivity of solution is observed in resistance by the following expression: $R = l/\kappa A$, where l; distance between electrodes, κ; ionic conductivity, and *A;* electrode area,[45] and thus the solution resistance is inversely proportional to its own ionic conductivity. All the fitted results are summarized in Fig. 32h. The SPI resistances are an inverse form to the ionic conductivity of the wetting

electrolytes. This ascertains that free ion concentration and ion mobility of electrolytes influences Li^+ transport behavior of SPI on LNMO electrodes. All the two features, the previous low Coulombic efficiency and this Li^+-transporting behavior, are significantly correlated with permeable property of surface film generated on LNMO electrodes.

4. RESULTS AND DISCUSSION

4.2. Charge Transfer Kinetics at Electrode Interface

4.2.1. Li^+ concentration and charge transfer resistance

Ionic conductivity of an electrolyte medium is determined by free ion concentration and ion mobility: $\kappa = F\sum_i |z_i| C_i u_i$ (F; Faraday constant, z_i; charge of free ion, C_i; concentration of free ion, u_i; mobility of free ion).[31] SPI is filled with liquid electrolytes, it is thus assumed that ionic conductivity of SPI is much larger than that of SEI due to its fast ion mobility of liquid electrolyte (u_i). The result was the opposite. As is seen in Fig. 1, SPI resistance is larger than the SEI one. Furthermore, if we consider the two surface film thickness: SPI thickness on LNMO electrode is estimated to 15 nm while SEI thickness on graphite electrode is done to 100 ~ 125 nm from TEM (Fig. 20), it is supported that the Li^+ ion delivery ability of SPI is much poorer than that of SEI. Based on this observation, we could assume that population of free ion in SPI is much less than that in SEI. In order to quantify the Li^+ ion

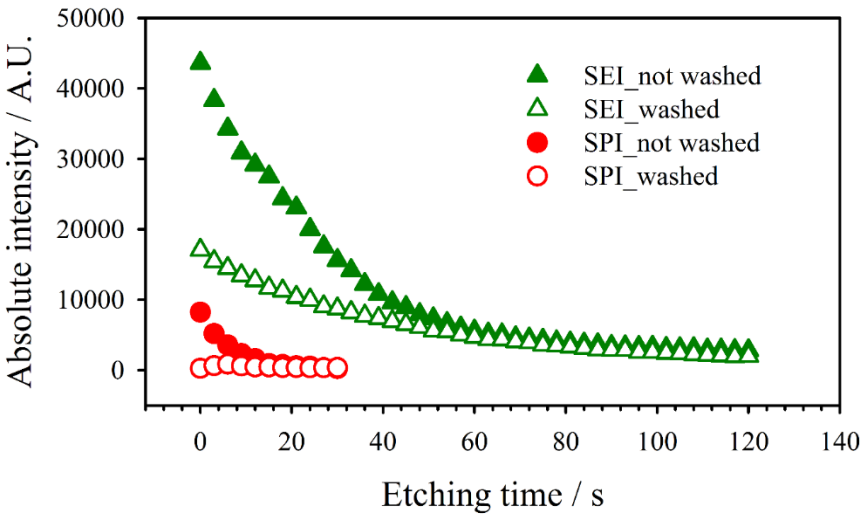

Figure 33. The $^{6}Li^{+}$ intensities for the two surface films. The SPI is generated on LNMO electrode to 4.9 V, and the SEI is formed on graphite electrode to 0.005 V by galvanostatic charging.

concentration, the $^{6}Li^{+}$ ion intensity was investigated by time of flight-secondary ion mass spectrometry (TOF-SIMS). Note that $^{6}Li^{+}$ ion (7.6 %) intensity was displayed instead of $^{7}Li^{+}$ (92.4%), more populated natural isotope, which was saturated to the maximum intensity of the instrument not to discriminate the $^{7}Li^{+}$ intensity between samples. Fig. 33 exhibits the Li intensity difference between SEI and SPI. SPI is generated on LNMO electrode to 4.9 V, and the SI is formed on graphite electrode to 0.005 V by galvanostatic charging. Even though the SPI-deposited LNMO electrode is not washed by DEC, the Li^{+} population in SPI is much lower than that in SEI. Li^{+} ions are strongly embedded in SEI, which is because they are still richly observed after washing by DEC.

In order to obtain Li^{+} ion concentration per unit thickness, some inert planar metal electrode was employed. In detail, to determine Li^{+} concentrations across the film depth, surface films were deposited on inert planar metal electrodes (a Cu plate for SEI and a Pt plate for SPI) of the same surface area ($\pi \times 0.3^{2}$ cm^{2}). The surface films were generated by linear potential sweeping (from the OCV (~3.0 V) to 0.005 V for the SEI, or 5.2 V for the SPI) at a scan rate of 1.0 mV s^{-1}, and Li^{+} ion concentrations were analyzed by depth-profiling using TOF-SIMS. Fig. 34 depicts the $^{6}Li^{+}$ (natural abundance, 7.6 %) concentration profiles across the film depths. Several features are immediately apparent. Firstly,

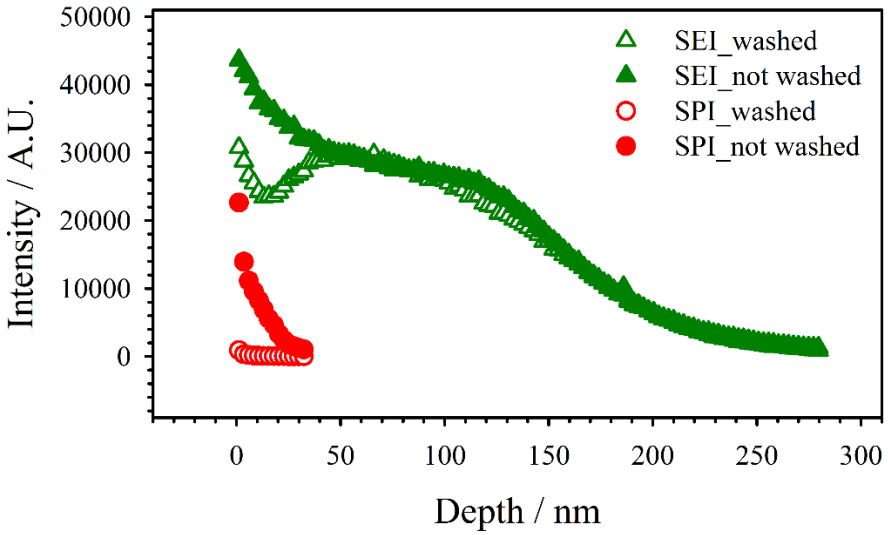

Figure 34. TOF-SIMS depth-profiling data for $^{6}Li^{+}$ ions in the SEI on a Cu electrode, and the SPI on a Pt electrode.

Table 8. Li^+ ion concentration per thickness for the two surface films.

	SEI	**SPI**
Thickness / nm	280	33
Integration of ^6Li / A.U.	4.9×10^7	2.3×10^5
Total Li / A.U.	6.5×10^8	3.1×10^6
Li per thickness / nm^{-1}	2.3×10^6	9.3×10^4

the SPI is much thinner than the SEI. Specifically, given that $^{6}Li^{+}$ ions are not populated inside the Cu and Pt electrodes, but Li^{+} ions are only present inside the surface films, one can recognize that the SPI on Pt electrode is thinner than the SEI (Fig. 34). Secondly, Li^{+} ions in the SPI are easily removed by washing, whereas such leaching occurs only from the top-most surface region of the SEI. These two features have already been discussed above. Thirdly, the concentration of Li^{+} ions, which are among the charge carriers for ion conduction, is much smaller for the SPI. In particular, to quantify the Li^{+} concentrations in the SPI and SEI layers, the $^{6}Li^{+}$ signals were integrated and calibrated using the natural isotope ratio, resulting in the Li^{+} concentrations (sum of $^{7}Li^{+}$ and $^{6}Li^{+}$) per unit thickness that are listed in Table 8. As can be seen, the Li^{+} concentration per unit thickness is much smaller for the SPI, supporting that the poorer ionic conductivity (Fig. 19 and 21) of the SPI results from fewer charge carriers (free ions) inside the SPI layer.

This could accounted for by electrochemical charging situation as in Fig. 23. Either SEI or SPI, the two surface films are significantly generated during charging, in which electrolytes consume electrons from electrodes. When electrochemical charging, anions are generated at the graphite electrode, and thus Li^{+} ions are embedded in SEI by ionic interaction. In contrast, carbonates cations evolved at LNMO electrode, and thus salt anion such as PF_6^{-} combines the cation, and Li^{+} ions are

not embedded in SPI on LNMO electrode. As a result, the surface film, anion-contained cationic organic layer, could prevent Li^+ ions to be densely deposited on the LNMO electrode.

The low Li^+ ion concentration in SPI also cause charge transfer resistance larger as well as the film resistance. The charge transfer resistance is responsible for a significant energy barrier between electrolytes and electrodes, as depicted in Fig.35: for example, 50 ~ 70 kJ mol^{-1} for graphite electrodes.[18,102] Generally, electron charge transfer rate depends on the concentration of redox species in electrolyte: $O + e^- \rightarrow R$ (at electrode), $\text{rate} = k(T)C(o,t)$ in which d=0, distance from electrode.[31] Such as the redox species in electrolyte, in lithium-ion batteries (LIBs), charge transfer reaction also occurs at electrolyte/electrode surfaces; Li^+ ions are inserted into electrodes with receiving electron from electrode. Therefore, it raises suspicion whether Li^+ ion concentration at surface film/electrodes interface causes the charge transfer resistance for LNMO electrode larger than graphite electrode. In order to ascertain effect of Li^+ ion concentrations at the SPI/LNMO electrode interface, the lower and higher concentrated electrolytes were introduced to confirm whether the Li^+ concentration could influence charge transfer resistances. Note that SPI is permeable, and it is thus assumed that Li^+ concentration of electrolytes could determine population of Li^+ ion at the surface film/LNMO electrode. Fig.

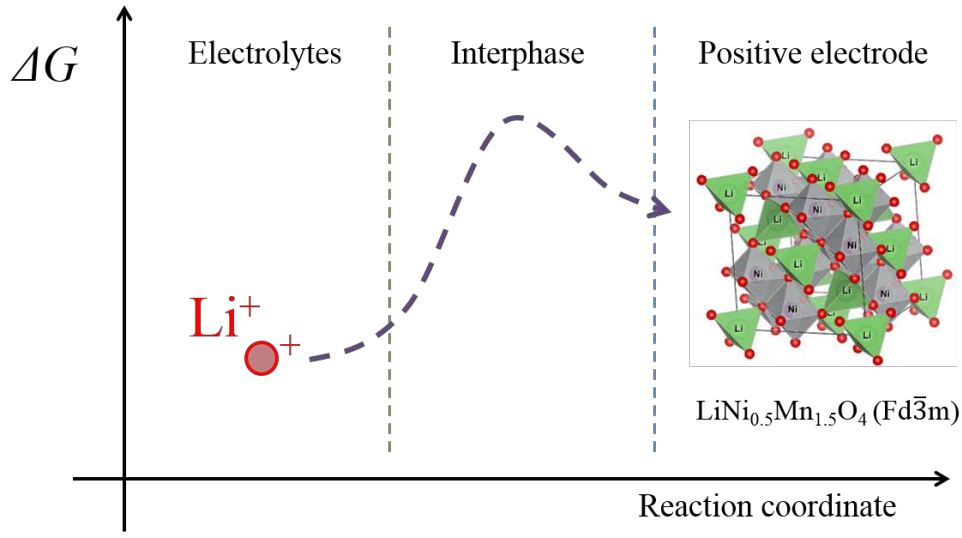

Figure 35. Diagram of energy barrier for charge transfer reaction into LNMO electrodes.

36 shows the changes in charge transfer resistances with Li salt concentrations. After charging to 4.9 V to generate SPI on LNMO electrode and discharging to SOC 50 (Quasi-open circuit voltage; QOCV 4.71 V) with 1.3 *M* $LiPF_6$ in EC:EMC:DEC = 3:2:5 (*v/v/v*), the SPI-deposited LNMO electrodes were washed with DEC and followed to be rewetted with $LiPF_6$ concentration in the fixed solvent composition EC:DMC = 5:5 (*v/v*). As is seen in Fig. 36b and 36c, from low concentrations to high concentrations, it is observed that the second semi-circles continually decrease. The second semi-circle, which is meaning for the charge transfer resistance,[80,86,87] which are all fitted and summarized in Fig. 36d. This ascertains that Li^+ ion population at electrode surface is one of factors to affect charge transfer reaction, and implies that a highly concentration improves charge transfer resistance for the LNMO electrode.

This advantageous feature of a highly concentrated electrolyte, however, are offset by increase of surface film and solution resistances. Fig. 36c shows that Li^+ concentrated electrolyte lead solution and film resistances for the LNMO to increase, which would be influenced by lower ionic conductivites than 1.0 *M* of electrolyte. Usually in EC-mixed composition, for example, EC:DMC = 5:5 or 3:7 (*v/v*), the higher concentrations than 1.0 *M* suffers from frictional drag force by viscosity increase of electrolyte: $u_i = \frac{|z_i|e}{6\pi\eta r}$ (η; viscosity, r; ion radius).[31] This

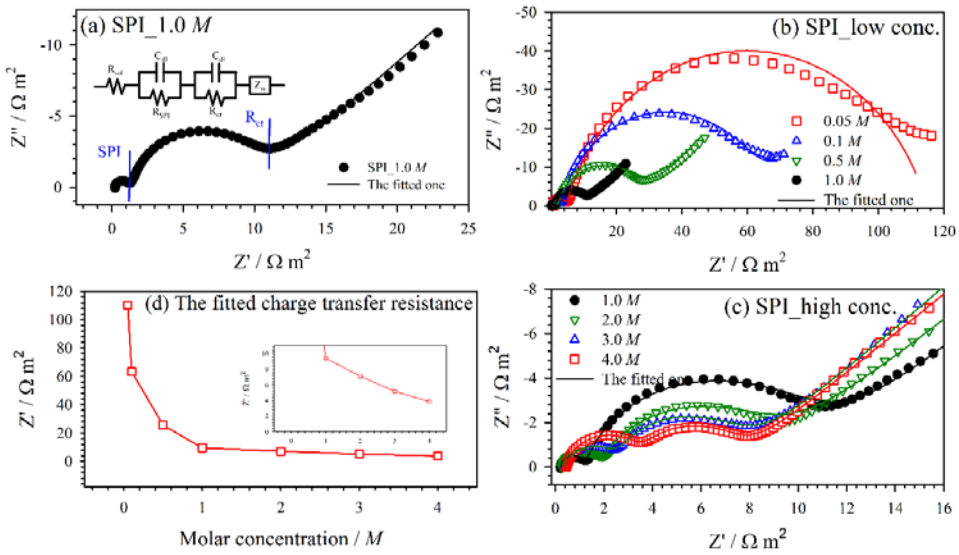

Figure 36. The ac impedance spectra for the SPI-generated LNMO electrode with $LiPF_6$ concentrations. After charging to 4.9 V and discharging to SOC 50 (QOCV 4.71 V), the SPI-deposited LNMO electrodes washed with DEC and followed to be re-assembled with various $LiPF_6$ concentrations in EC:DMC = 5:5 (*v/v*). The wetted electrolytes are 1.0 *M*; (a), low concentration; (b), high concentration; (c), and the fitted charge transfer resistances; (d).

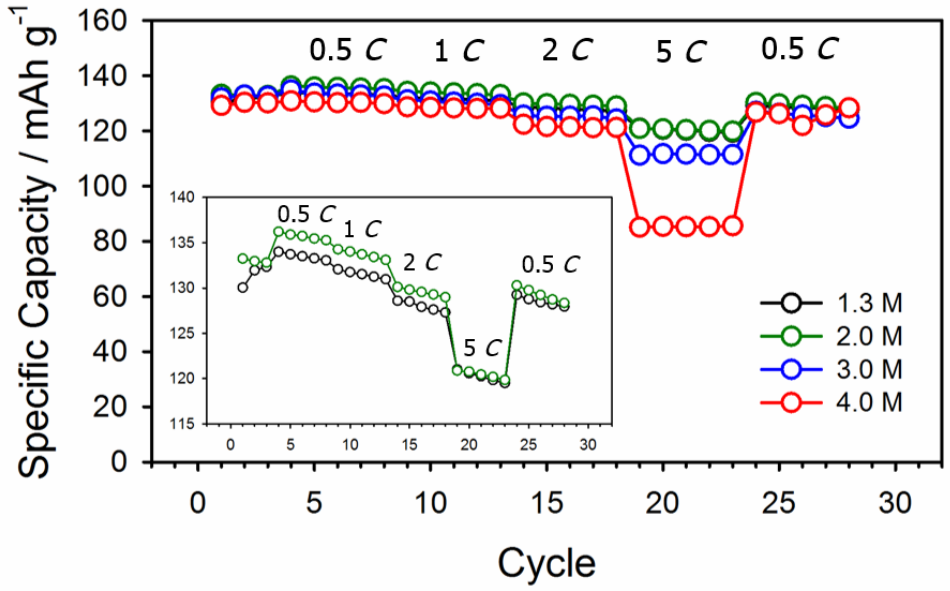

Figure 37. The rate performances of LNMO electrode for the $LiPF_6$-highly concentrated electrolytes in EC:DMC = 5:5 (*v/v*).

viscosity increment in highly concentrated compositions induces ionic conductivity of electrolytes to lower and the film resistance to larger for the SPI on LNMO electrode due to its permeable property. Hence, the simply concentrated electrolyte: e.g, 2.0 M $LiPF_6$ in EC:DMC = 5:5 (*v/v*), does not improve rate performance for the LNMO electrode. Fig. 37 shows these aspects. The 2.0, 3.0, or 4.0 *M* in EC:DMC = 5:5 (*v/v*) does not show much improved rate performances. It very seems likely that viscosity increase in the simply concentrated compositions offsets the favorable charge transfer reaction by increase of the solution and film resistances. Therefore, a highly concentrated electrolyte should be organized with considering this viscosity upsurge issue.

4.2.2. Highly Li^+-concentrated electrolyte design

In order to organize a competitive highly Li^+ concentration electrolytes, it is first investigated how ionic conductivity changes in regard to lithium hexafluorophophate ($LiPF_6$) concentration in carbonates solvents compositions. Usually in cyclic and linear carbonates-mixed compositions in 5:5 or 3:7 (*v/v*), maximum ionic conductivities are observed between a range of 1.0 and 1.3 *M* as is seen in Fig. 38b.[82] If $LiPF_6$ concentration is lower than 1.0 M in the cyclic and linear carbonates-mixed compositions, poor free Li^+ ions are responsible for

Table 9. The physical properties for the carbonates solvents. [36,103]

	PC	**EC**	**DMC**	**EMC**	**DEC**
Viscosity	2.53	1.90 (40 ℃)	0.59	0.65	0.75
Dielectric constant	64.92	89.78 (40 ℃)	3.11	2.96	2.81

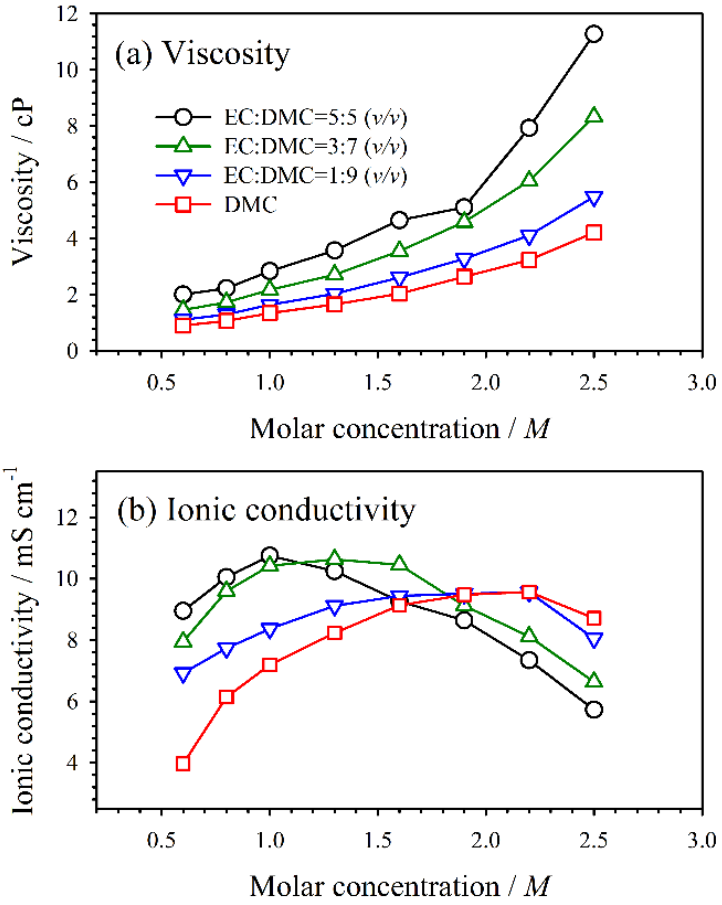

Figure 38. (a) Viscosity and (b) ionic conductivity for electrolyte compositions according to ratio of carbonates solvents and lithium hexafluorophosphate ($LiPF_6$) salt.

the low ionic conductivity than 1.0 *M* of one. With being concentrated, free ion increase, and thus ionic conductivity is optimized to the maximum values. When $LiPF_6$ concentration is over 1.0 *M* in the mixed compositions, even if Li^+ ion quantity becomes larger, the viscosity increases to cause ionic conductivity too low (Fig. 38ab). It should be reminded that ionic conductivity of electrolytes are determined by the equation: ionic conductivity $\kappa = F\sum_j|z_j|c_j u_j$ (F; Faraday constant, z_j; ion charge, c_j; free ion concentration, u_j; ion mobility) and ion mobility (u) suffers from frictional drag force by viscosity of the solutions: $u_i = \frac{|z_i|e}{6\pi\eta r}$ (η; viscosity, r; ion radius).[31] That is to say, ion transport of electrolytes depends on viscosity of the solution as well as ion concentration. Such a viscosity problem could be mitigated by adding more less-viscous linear carbonates at the expense of the more-viscous cyclic carbonates. Usually, linear carbonates exhibit much lower viscosity than cyclic carbonates; viscosities: EC; 1.90 (at 40 ℃), PC (propylene carbonate); 2.53, DMC; 0.59, EMC (ethyl methyl carbonate); 0.65, DEC (diethyl carbonate); 0.75 at 25 ℃.[36,103] Among these linear carbonates, the viscosity of DMC is lower than other linear carbonates (EMC and DEC), and thus DMC was employed to minimize viscosity increase in this study. In the DMC-rich compositions (Fig. 38ab), over at 1.5 *M* concentrations, viscosity increase slows down and

ionic conductivity is optimized to maximum values as $LiPF_6$ is concentrated. The less-viscous linear carbonate DMC, however, has much less-dielectric constant (ε) then cyclic carbonates such as EC: EC; 89.78, PC; 64.92, DMC; 3.107, EMC; 2.958, DEC; 2.805.[36] The information about all dielectric constant and viscosity is summarized in table 10. It should be also noted that ionic conductivity is expressed in total concentration times molar conductivity: $\kappa = C\Lambda$ (C; total concentration, Λ; molar conductivity), and the molar ionic conductivity (Λ) is lowered in more less dissociable medium by the following equation: $\Lambda = \Lambda^0 - (A + B\Lambda^0)\sqrt{C}$, $A \propto \varepsilon^{-1/2}$, $B \propto \varepsilon^{-3/2}$.[32] The DMC-rich compositions such as EC:DMC = 1:9 (*v/v*) or DMC alone generate smaller free ions than the EC-rich compositions (EC:DMC = 5:5 or 3:7 (*v/v*)), and thus exhibit less ionic conductivities about at a range of 1.0 *M*. When adding Li salts continually more over 1.0 *M*, absolute free ion concentrations increase, and the resulting ionic conductivities were optimized over at 2.0 *M* (Fig. 38b). It is ascertained that ionic conductivities are reached over at 9.0 mS cm^{-1} even for the EC-less or EC-free compositions, which are close values with 11.5 mS cm^{-1} for EC-rich compositions. It is thus expected that 2.0 *M* or more $LiPF_6$ in DMC alone would be appropriate for a highly concentrated electrolyte composition without declining ionic conductivity too low.

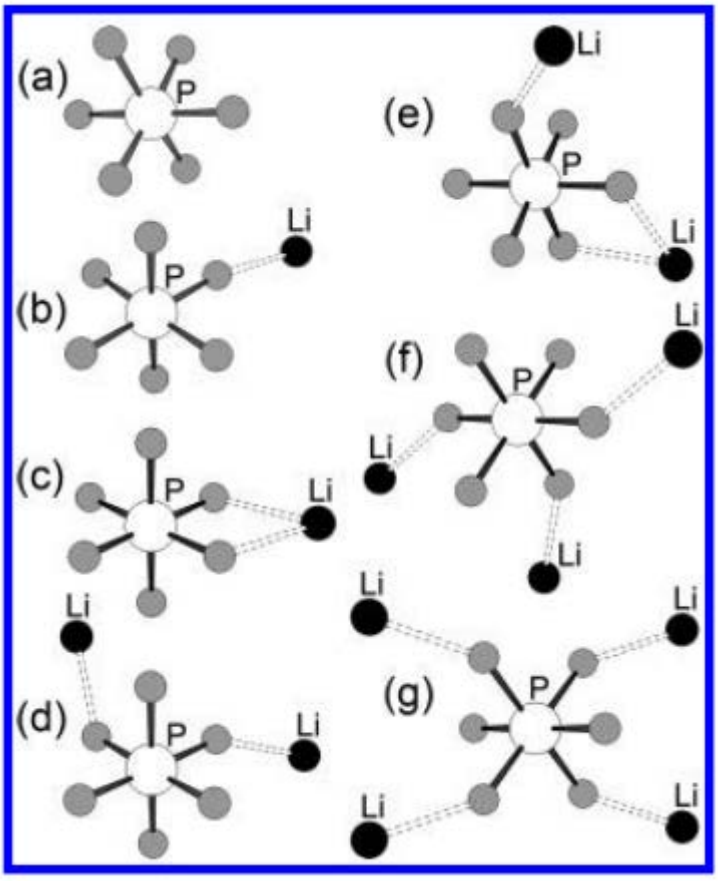

Figure 39. Examples of coordinations for Li^+ and PF_6^- ion. (a) free ion, (b) CIP (contact ion pair)-Ⅰ, (c) CIP-Ⅱ, (d) AGG (aggregate)-Ⅰa (triple ion), (e) AGG-Ⅰb, (f) AGG-Ⅱ, and (g) AGG-Ⅲ.[104]

In the low ion-dissociable DMC alone medium, it was ascertained how the conductive Li^+ ions are generated beyond 1.0 *M*. Generally, non-aqueous solvents with dielectric constant below about 15, such as DMC (ε; 3.107), generate ion pair: $Li^+ \cdots PF_6^-$ and aggregates over ion triplets: $Li^+ \cdots PF_6^- \cdots Li^+$ as well as free ion: Li^+ as is seen in Fig. 40.[32,104,105] Depending on the degree of coordination, various solvation states are coordinating ratio with one to one, if the Li^+ ion is coordinated with F atom with one or two, the CIP is re-classified in CIP-Ⅰa and CIP-Ⅰb. The same manner is also applied in AGG-Ⅰ. The coordination ratio of Li^+:PF_6^- with 2:1 is referred to AGG-Ⅰ (ion triplet), with 3:1 is called to AGG-Ⅱ, and with 4:1 is named to AGG-Ⅲ. Solvation state for $LiPF_6$ in DMC alone is ascertained from raman spectroscopy (Fig. 40). Usually, solvation states of electrolytes are ascertained by solvent or anion raman vibration instead of Li^+ ion, which is because that they has their own chemical bonds variable with regard to solvation states. The raman active vibration modes are summarized in table 10.[104-107]

A highly dielectric solution medium such as EC-rich mixed composition, lithium salt completely dissociated to generate mostly free ion in the solution (Fig. 40a). This is confirmed by the P-F stretching mode of PF_6^-,[104,105] the the P-F stretching vibration moves from 745 to 736 cm^{-1} (free PF_6^-) in the medium. Such in a highly dissociable

Table 10. Vibration modes of electrolyte components for the raman spectra.[104-107]

Vibration mode	Wavenumber / cm^{-1}
EC ring bending	714
P-F stretching of PF_6^-	745
[a]Free PF_6^-	736
[a]CIP-I	712
[a]AGG-Ia	745

[a]:experimentally determined in this work, based on the tendencies of [104]

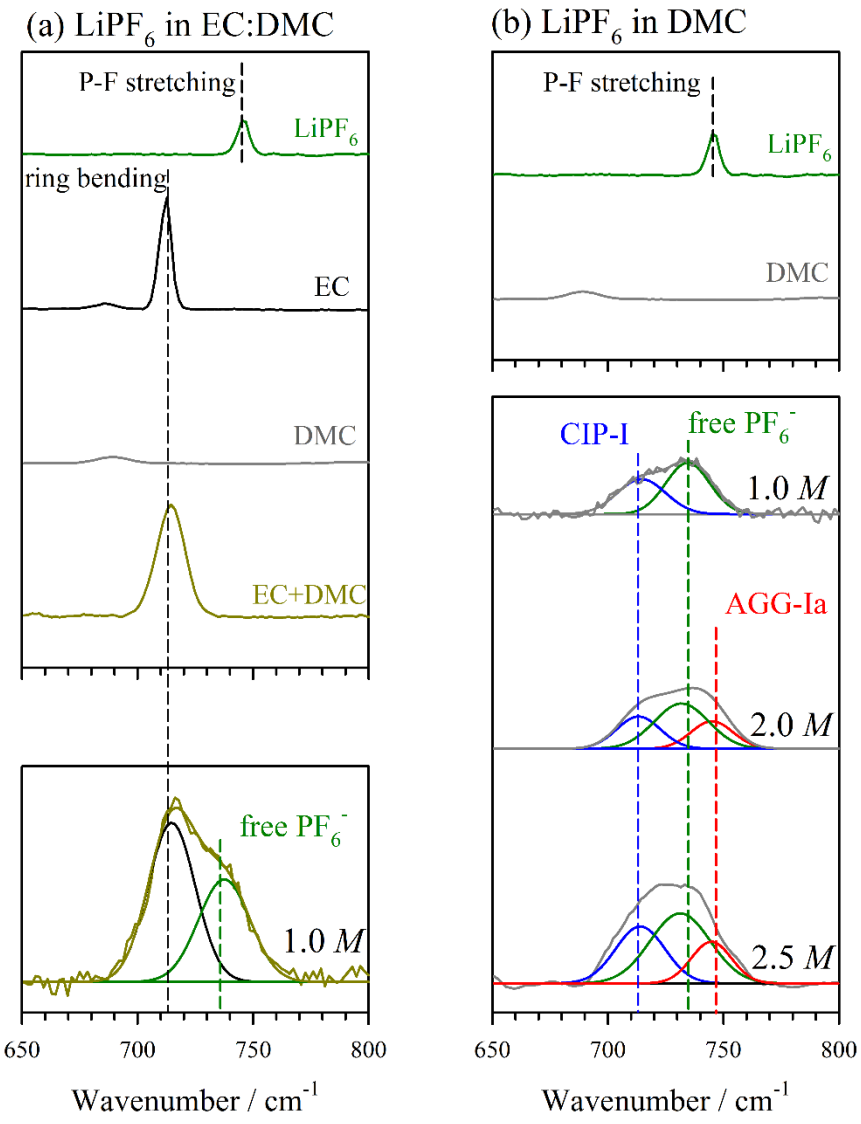

Figure 40. Raman spectra for solvation states with various electrolytes compositions. (a); 1.0 *M* $LiPF_6$ in EC:DMC = 5:5 (*v/v*), and (b); $LiPF_6$ in DMC. The detailed vibration modes are described in the inset.

medium, each Li^+ ion and PF_6^- anion are fully solvated by the solvents to be completely spaced each. The usual composition, the mixed composition of cyclic carbonate and linear carbonate such as 1.0 *M* $LiPF_6$ in EC:DMC = 5:5 (*v/v*), most of ions are in solvent-separated ion pair (SSIP or free ion) due to EC with high dielectric constant. On the other hand, in a low ion-dissociable medium such as DMC alone of composition, the PF_6^- anion generates CIP-Ⅰ and AGG-Ⅰa as well as free PF_6^- in the low ion-dissociable medium. When $LiPF_6$ is added to 1.0 *M* in DMC, the free PF_6^- (736 cm^{-1}) and CIP-Ⅰ anion (712 cm^{-1}) are observed. When $LiPF_6$ lithium salt dissolves in DMC over at 2.0 *M*, AGG-Ⅰa (745 cm^{-1}) anion begins to evolve. Over at 2.0 *M* of composition, ion triplet (AGG-Ⅰa) are additionally generated, and thus the ion triplet (AGG-Ⅰa) contributes the increase of ionic conductivity in DMC alone composition beyond 1.0 *M* (Fig. 1b). As the previous literature, this ion triplet as well as free ion responds to Coulombic force to contributes ionic conductivity of electrolyte solution.[32] The final optimized composition was determined to 2.5 *M* $LiPF_6$ in DMC; free ion and ion triplet (AGG-Ⅰa) intensities a little more increase from 2.0 to 2.5 *M* (Fig. 2), while ionic conductivity slightly decrease from 2.2 to 2.5 *M* (Fig. 39b). Hence, usually, a highly Li^+ concentrated electrolytes are organized beyond the concentration region, in which ion triplets are generated.[108-112]

In addition, solubility for $LiPF_6$ in DMC was also examined via ICP-AES method. After pouring the 2.5 *M* $LiPF_6$ in DMC into syringe filter with 0.45 μm of pore size, the filtrated electrolyte was delivered to ICP-AES instrument. Instead of Li, which is not able to analyzed by ICP, phosphorous (P) was measured by this technique. Note that P corresponds to Li by one to one molar ratio for $LiPF_6$. The obtained P concentration was 2.21 *M*, which certainly ascertains that $LiPF_6$ dissolves in DMC over at 2.0 *M*.

4.2.3. Charge transfer reactions and Li^+ insertion rates

It was examined by TOF-SIMS technique, whether this highly concentrated electrolyte provides more Li^+ ion than the usual 1.0 *M* of one at the electrolytes/LNMO interfaces. Fig. 41 shows the Li^+ quantities on LNMO electrolytes after first charging to 4.9 V according to the two electrolytes. The signals for the 2.5 *M* of one are observed more higher than the usual 1.0 *M* of one. This supports that this highly concentrated electrolyte provides more high Li^+ concentration at electrolytes/electrodes surface. This is due that the surface film on LNMO electrode is permeable, and thus electrolytes could give more Li^+ ion, as Li^+ ions are concentrated even in the less dissociable medium involving free ion, ion pair, and aggregates.

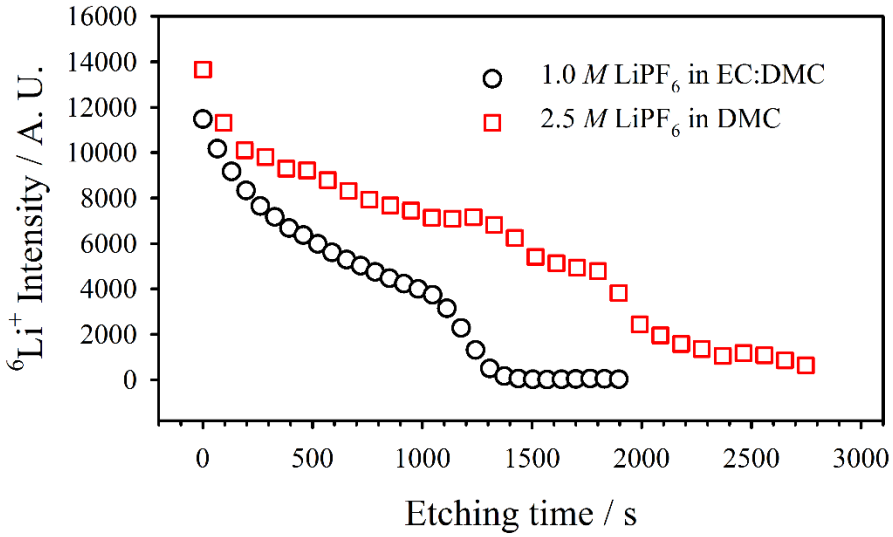

Figure 41. $^6Li^+$ intensities on Al plate electrode after wetting for 24 hour with the two electrolytes.

It was examined, if this highly concentrated electrolyte can improve charge transfer reaction. Electrolytes are associated with the following resistances; solution itself, film on electrodes, and charge transfer into electrodes. In order to examine these resistances, ac impedance was introduced to discriminate each contribution (Fig. 42). When comparing the two compositions, 1.0 *M* in EC:DMC = 5:5 (*v/v*) and 2.5 *M* in DMC, there are disparities for their concentration and solvent composition, the 1.0 *M* in DMC composition is thus additionally employed to ascertain the two contributions. The semi-circles in Nyquist plot have their usual meaning.[80,86,87] After the first charging to 4.9 V (SOC 100), ac impedances were measured for the LNMO electrodes (Fig. 42). As is seen in the Nyquist plot, the second semi-circles, which is charge transfer reaction into electrodes, are noticeably discriminated than other resistances according to electrolyte compositions. Even with the same 1.0 *M*, charge transfer reaction for in DMC alone is more favorable than that for in EC-DMC mixed composition. It is likely that DMC is less coordinating towards to Li^+ ion than EC, and this serves favorable desolvation from electrolyte. It could be inferred from ab initio calculation that binding energies for Li^+/solvents decrease when solvent compositions changes from EC-rich/DMC-poor solvation states to EC-poor/DMC-rich solvation states.[113] In detail, it was reported that Li^+ ion is usually four-coordinated by EC in EC-mixed compositions. The

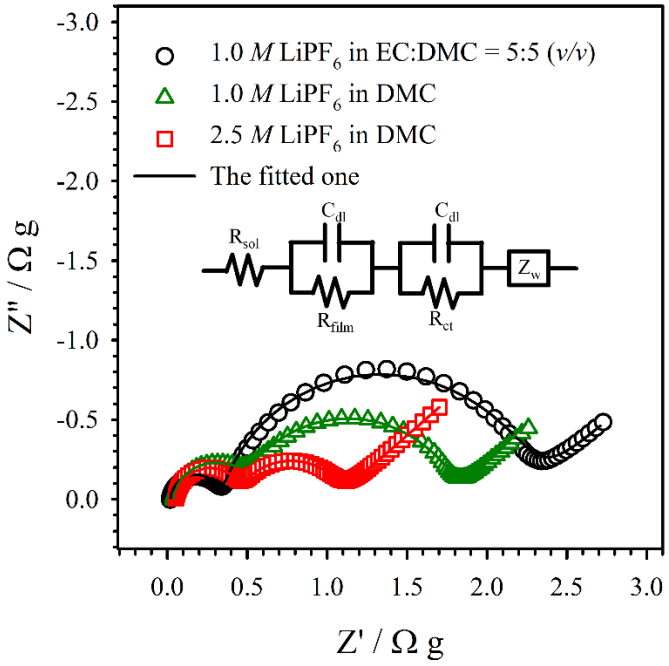

Figure 42. Nyquist plot (ac impedance) for symmetric LNMO/LNMO electrodes cells, assembled with a conventional electrolyte (1.0 *M* $LiPF_6$ in EC:DMC = 5:5 (*v/v*)), 1.0 *M* $LiPF_6$ in DMC, and the highly concentrated electrolyte (2.5 *M* $LiPF_6$ in DMC). The LNMO electrodes were charged to SOC 100 (QOCV; 4.73 V *vs.* Li/Li^+). Each equivalent circuit is indicated in the inset.

Table 11. The fitted resistances for the LNMO electrodes.

	LNMO			
	R_{sol}	R_{film}	R_{ct}	R_{total}
1.0 *M* in EC:DMC	0.02	0.31	1.89	2.22
1.0 *M* in DMC	0.06	0.40	1.34	1.80
2.5 *M* in DMC	0.05	0.39	0.61	1.05

binding energy for the four coordinated by EC is calculated to -145.3 kcal mol^{-1}, while the binding energies for the same one by DMC is done to -137.8 (trans DMC) ~ -134.7 (cis DMC) kcal mol^{-1}; the ranges depends on cis/trans conformation of DMC conformation. That is to say, the energy state by DMC solvation is a little higher than that by EC solvation. In addition, the Li^+ binding energy by one EC is calculated to -53.8 kcal mol^{-1}, however, that by one DMC is done to -50.2 (trans DMC) ~ -46.3 (cis DMC). "A solvent ⋯ Li^+ ⋯ NMO (delithiated LNMO)" must be the transition states for the Li^+ insertion, which could be thus assumed that "a solvent ⋯ Li^+" binding energy is a major factor for the desolvation process. This computational calculation results strongly supports that DMC-rich solvation would lead to favorable desolvation than the EC-rich solvation. As Li^+ ions are further concentrated in DMC, additionally more favorable charge transfer kinetics are observed (Fig. 42). The fundamental electrochemical charge transfer reaction rate depends on the surface concentration of redox species reactant in electrolytes: $v = kC(0,t)$,[31] and thus the additional charge transfer reaction in decrease is responsible for this high population of reactant, Li^+ ions, for the LNMO electrode. Obviously, the increased Li^+ ions in electrolytes provide high surface Li^+ ion concentration for the LNMO electrode due to permeability of its own surface film and resultantly improve the charge transfer reaction. The DMC alone and Li^+

concentrated composition also show favorable charge transfer into LNMO electrodes. All the impedance results were fitted and the resulting calculated resistances values are summarized in table 11. While this highly concentrated $LiPF_6$ in DMC alone loses solution or film resistances a little, it gains much more improved charge transfer resistance to lead to total resistance in decrease. Weak coordinating of solvent toward to Li^+ ion and more Li^+ ions at electrode interfaces drive favorable charge transfer into electrodes.

The 2.5 *M* $LiPF_6$ in DMC composition was examined, if it can improve rate performance due to decrease of total resistance by the favorable charge transfer reaction. The above-three electrolyte compositions are all tested in Li half-cell to confirm each contribution: degree of solvent coordination and high population of Li^+ ions. Before inserting Li^+ ion, all electrodes were delithiated (SOC 100) by maintaining constant voltages for 1 h at the cut-off voltage (4.9 V) after applying at 0.5 *C* of delithiation current. A significant contrast is seen between the commercial electrolyte and the highly concentrated electrolyte (Fig. 43). As is seen in the galvanostatic lithiation voltage profiles of Fig. 43, when increasing lithiation rates, polarization is conspicuous in the conventional composition (Fig. 43a), and thus which cause to deliver just 60 mA h g^{-1}, about half of the LNMO usual capacity, at 20 *C* of lithiation rate. In contrast, 1.0 *M* $LiPF_6$ in DMC composition exhibits

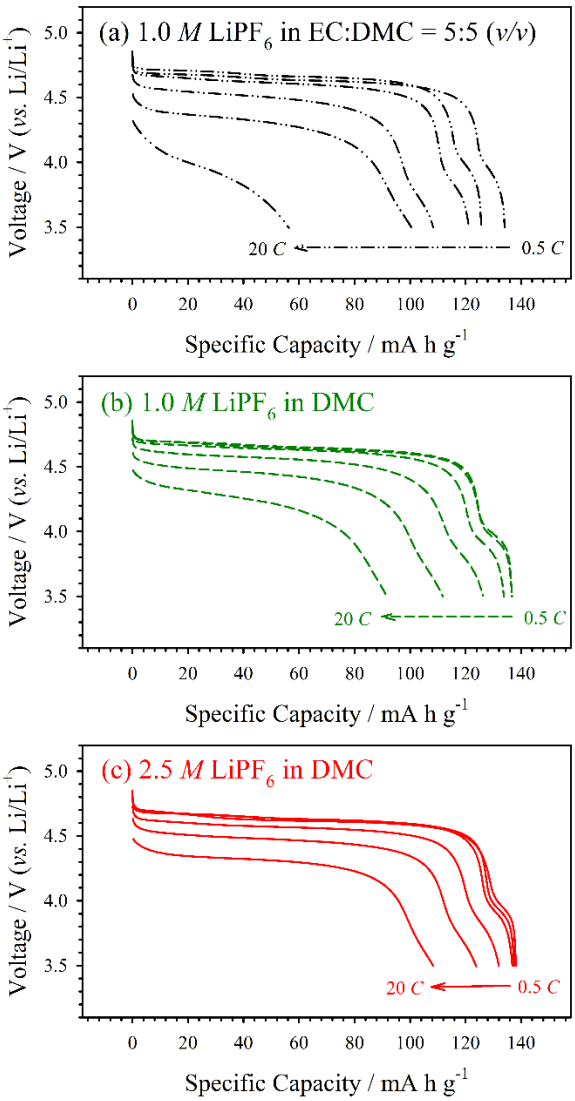

Figure 43. The galvanostatic lithiation voltage profiles for LNMO electrodes with electrolytes compositions. (a); a conventional composition (1.0 *M* $LiPF_6$ in EC:DMC = 5:5 (*v/v*)), (b); 1.0 M LiPF6 in DMC, and (c); the highly concentrated electrolyte (2.5 *M* $LiPF_6$ in DMC). Electrodes were completely Li^+-extracted before testing lithiation rates.

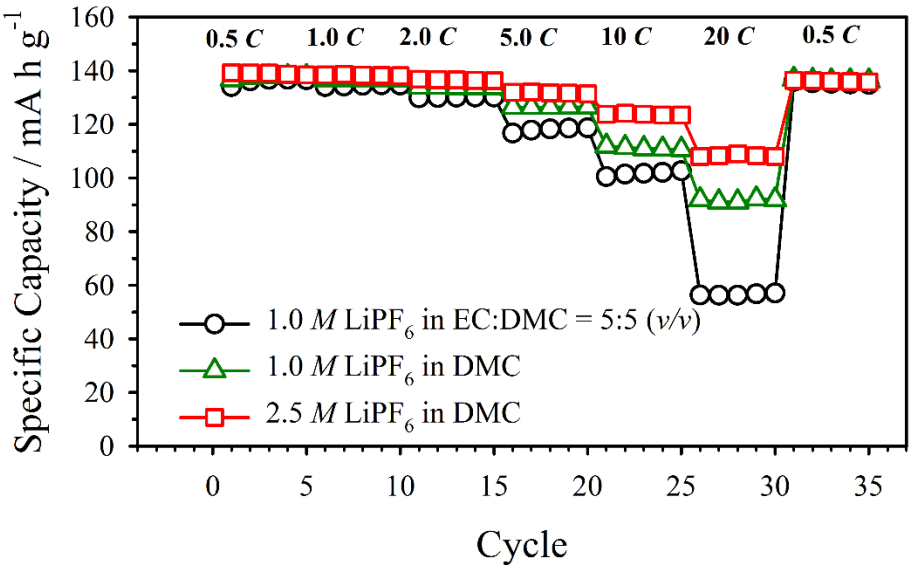

Figure 44. Rate performances of LNMO electrode for the 1.0 *M* $LiPF_6$ in EC:DMC = 5:5 (*v/v*)), 1.0 *M* $LiPF_6$ in DMC, and the highly concentrated electrolyte (2.5 *M* $LiPF_6$ in DMC). All Li^+ ions are extracted before testing lithiation rates.

less polarization than the EC-mixed composition, and the more concentrated 2.5 *M* $LiPF_6$ in DMC shows further mitigated polarization even at 20 *C* of lithiation rate. The two electrolytes, 1.0 *M* $LiPF_6$ in DMC, and 2.5 *M* $LiPF_6$ in DMC, exhibits total resistance in decrease by the much favorable charge transfer reaction, which also shows less polarization for galvanostatic lithiation of LNMO electrode. The resulting rate performances are demonstrated in Fig. 44. The 1.0 *M* $LiPF_6$ in DMC composition delivers about 90 mA h g^{-1}, and the 2.5 *M* $LiPF_6$ in DMC composition develops over 100 mA h g^{-1} during lithiation even at 20 *C* of rate. Beyond the rate of 5 *C*, the 1.0 *M* composition does not deliver capacity properly. Briefly, the much improved charge transfer reaction by the low coordinating DMC solvent and high population of reactant Li^+ ion, which lead less polarization during galvanostatic lithiation to improve lithiation rate property for the LNMO electrode.

The fast Li^+ insertion kinetics by favorable charge transfer reaction could be accounted for by charge transfer activation energy and population of reactants. The charge transfer reaction occurs by that the solvated Li^+ ions are desolvated from solvent compositions, and followed to get into electrodes beyond activation energy barriers for transition state. If the reaction linearly depends on temperature, the activation energy and the corresponding rate constant could be estimated by Arrhenius plot. T. Abe et. al confirmed that charge transfer reaction

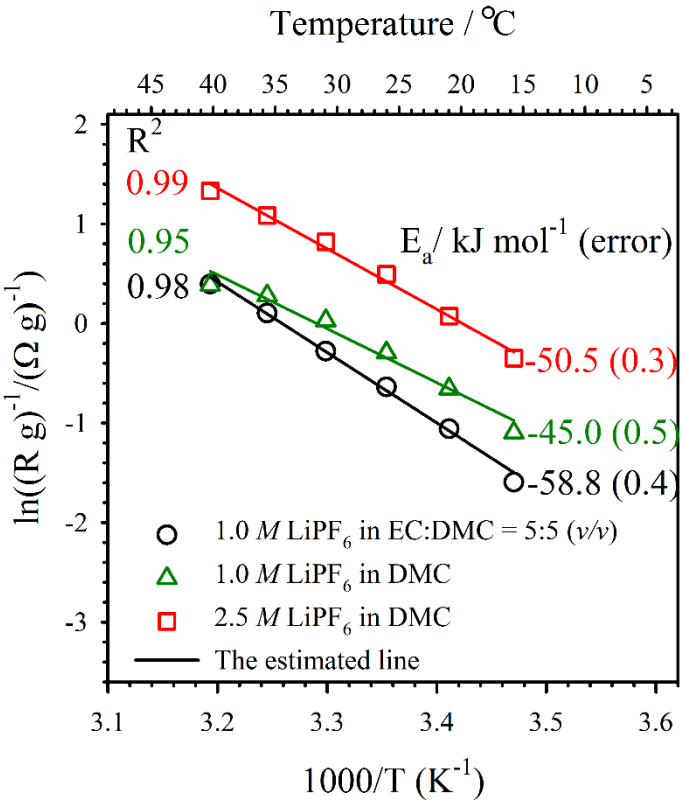

Figure 45. Arrhenius plots for LNMO electrode (LNMO/LNMO symmetric cell) derived from the fitted charge transfer resistances of Ac impedances with temperatures. The correlation between the log scale of the reciprocal charge transfer resistances and the inverse form of temperature are estimated by a linear equation. The used electrolytes, and their corresponding activation energies are indicated in the inset.

in LIBs also shows Arrhenius behavior.[68,114-116] In their method, the log form of the inverse charge transfer resistances is plotted with the reciprocal form of temperatures, and which were estimated by linear equations. Their plotting method was also adopted in this work to ascertain how electrolyte compositions affect charge transfer kinetics. The previous Ac impedances (Fig. 42) were performed with temperatures, and the resulting Arrhenius plots were displayed in Fig. 45. As is seen in these plots, the differences for slopes and y-intercepts are noticeable between the three electrolyte compositions. First, the slopes in Arrhenius plot are correlated with activation energy in Arrhenius equation: $\ln k = -\frac{E_a}{R} \cdot \frac{1}{T} + \ln A$, log scale of rate constant from Arrhenius equation. At 1.0 *M* of concentration, the charge transfer activation energies for DMC alone composition (45.0 kJ mol^{-1}) are smaller than that for EC-mixed composition (58.0 kJ mol^{-1}). Because they are the same 1.0 *M* of $LiPF_6$ concentration and just different in solvent composition, it could be accounted for by that solvation energy state predominantly influences the desolvation activation energies of Li^+ ions. As explained in the above paragraph, Oleg Borodin's computational calculation strongly supports this calculation.[113] Even though solvation energy state for DMC composition is a little higher than that for EC-mixed composition, which rather decrease desolvation activation energies, and thus which lead to favorable Li^+ charge transfer

reaction into electrodes. Although DMC composition contains low free ions than EC-mixed one at 1.0 *M* from the previous raman spectra (Fig. 40), its averaged activation energy for desolvation from free ion and ion pair per mol becomes lower by this solvation effect. When Li^+ ions are more concentrated, the charge transfer activation energies (50.5 kJ mol^{-1}) for the 2.5 *M* in DMC are about intermediate values between that for 1.0 *M* of ones. The activation energies indicate that the desolvation process of 2.5 *M* in DMC is easier than that of 1.0 *M* in EC-mixed composition, but more difficult than that of 1.0 *M* in DMC composition. This is likely due to increase in ion pair in DMC solution from 1.0 *M* to 2.5 *M* (Fig. 40). Li^+ ions in ion pair additionally suffer Coulombic attraction by the counter PF_6^- more than free ion in solution, which would cause higher activation energy for desolvation.

Second, as Li^+ ions are concentrated, y-intercept shifts upward totally. Even though the charge transfer activation energy for the highly concentrated electrolyte is a little higher than 1.0 *M* in DMC composition, the charge transfer resistance for it is more decreased than that of the 1.0 *M* in DMC. The y values shift in Arrhenius plot is associated with pre-exponential factor, A, in the Arrhenius equation. The pre-exponential factor (A) means collision frequency for Avogadro's number of molecules by based on collision theory for reactants: $A = \sigma \bar{v}_r N_A^2$, in which σ; cross section for collision, $\bar{v}_r$; relative velocity for

reactants, N_A ; Avogadro's number,[117-119] which should be considered; the charge transfer reaction occurs through contact of Li^+ ions and electrode materials at electrolytes/electrodes interfaces. The 2.5 times higher concentration from 1.0 *M* to 2.5 *M*, means that the Avogadro's number of molecules become 2.5 times in solution. Hence, the charge transfer improvement by molar concentration should be described by introducing additional concentration term in the equation for the Arrhenius plot of charge transfer reaction. The charge transfer resistance is re-described with this contribution of concentration.

$$\ln\left(\frac{1}{R_{ct}}\right) \propto -\frac{E_a}{R}\cdot\frac{1}{T} + \ln A + \ln[Li^+]$$

$$Li^+ \text{ insertion rate } \propto \frac{1}{R_{ct}} \propto Ae^{-\frac{E_a}{RT}}[Li^+] = k[Li^+]$$

This is similar with that charge transfer reaction rate depends on rate constant and electrode surface reactant in electrolyte: rate=kC(0,t).[31] The charge transfer reaction rate could be described by collision frequency for Li^+ and active material (pre-exponential factor: A), the activation energy (E_a) needed to desolvation process, and the concentration of Li^+ reactant. In conclusion, the favorable charge transfer reaction or Li^+ insertion rate for the highly concentrated electrolyte are driven from higher population of Li^+ reactant above activation energy required for desolvation than the 1.0 *M* of

compositions. From the previous raman spectra (Fig. 40b), the intensity for the ion triplet (AGG-Ⅰa) newly generates over at 2.0 *M* in DMC solution, which indicates that this the ion triplet (AGG-Ⅰa) participates in Li^+ charge transfer reaction. In the previous literature, it was reported that triple ion responds external electric field to contribute conductivity.[32] Hence, charge transfer reaction resistance or rate are improved by Li^+ concentration as well as the corresponding activation energy.

The same behavior is also observed in negative electrodes. The $Li_4Ti_5O_4$ (LTO) electrodes have an advantage for this study that they operate within electrochemical stability windows of carbonates-based electrolytes,[7] and the resulting film deposition is thus insignificant and electrolytes could contact to the electrode immediately. In order to confirm charge transfer reaction, the LTO electrodes were charged to SOC 10 (QOCV 1.56 V) (Fig. 46). It is noted that in initial cycles, a film resistance could not be observed for LTO electrodes,[68] by above explained insignificant film deposition.[7] Therefore, the one semi-circle is obviously charge transfer resistance for LTO electrode, which is because at 1.56 V. The charge transfer resistance is observed in decrease, as same for the previous LNMO electrode. Also, for the LTO electrode, the solvent effect and high Li^+ concentration influence the charge transfer reaction. The fitted values are summarized in table 12.

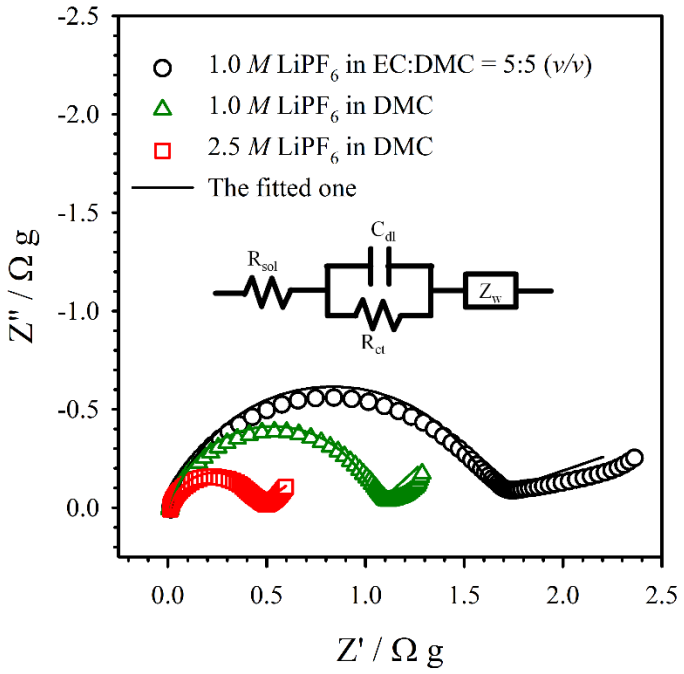

Figure 46. Nyquist plot (ac impedance) for symmetric LTO/LTO electrodes cells, assembled with a conventional electrolyte (1.0 *M* $LiPF_6$ in EC:DMC = 5:5 (*v/v*)), 1.0 *M* $LiPF_6$ in DMC, and the highly concentrated electrolyte (2.5 *M* $LiPF_6$ in DMC). The LTO electrodes were charged to SOC 10 (QOCV; 1.56 V). Each equivalent circuit is indicated in the inset.

Table 12. The fitted resistances for LTO electrodes.

	LTO		
	R_{sol}	R_{ct}	R_{total}
1.0 *M* in EC:DMC	0.011	1.608	1.619
1.0 *M* in DMC	0.014	1.032	1.046
2.5 *M* in DMC	0.013	0.435	0.448

As is seen in the galvanostatic lithiation voltage profiles of Fig. 47a, when increasing lithiation rates, polarization is conspicuous in the conventional composition, and thus which cause to deliver just below 20 mA h g^{-1} at 20 *C* of lithiation rate. In contrast, the 1.0 *M* and 2.5 *M* $LiPF_6$ in DMC less suffers from polarization to deliver close to each 100 and 140 mA h g^{-1} even at 20 *C* of high lithiation rate (Fig. 47b and 47c). The low coordination effect of DMC and high population of Li^+ ions mitigate polarization during high Li^+-insertion rate. The resulting rate characteristics are displayed in Fig. 48. This supports that the DMC solvent has less coordinating ability toward to Li^+ ion to allow preferential desolvation than EC, and the highly concentrated electrolyte has much more total Li^+ ions, involving free ion, ion pair, and aggregates than a 1.0 *M* composition. The high Li^+ population in electrolytes provides higher surface Li^+ ion reactant concentration during lithiation for the two electrodes as seen in Fig. 49. Fig. 50 of Arrhenius plot confirms that DMC alone of composition shows more favorable activation energy (low slope) for desolvation, and high population of Li^+ reactant shift charge transfer resistance upward totally: y-intercept moves upper direction. The favorable desolvation process by solvent composition and high population of Li^+ ions, which is responsible for the favorable charge transfer reaction and fast Li^+ insertion rate for LTO electrode as same as that for LNMO electrodes (Fig. 45). Considering

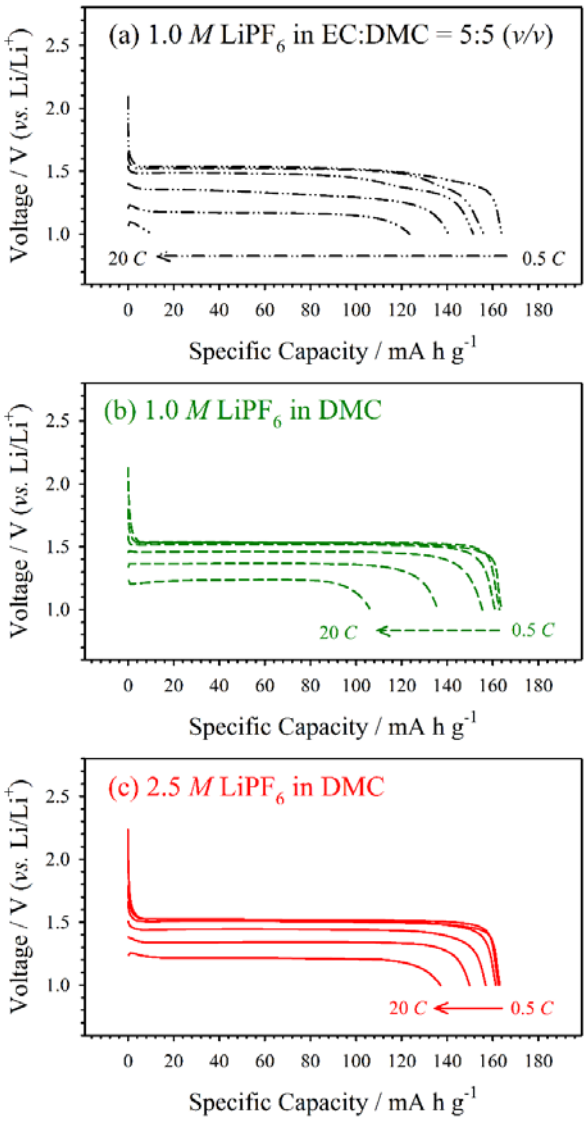

Figure 47. The galvanostatic lithiation voltage profiles for LTO electrodes with electrolytes compositions. (a); a conventional composition (1.0 *M* $LiPF_6$ in EC:DMC = 5:5 (*v/v*)), (b); 1.0 *M* $LiPF_6$ in DMC, and (c); the highly concentrated electrolyte (2.5 *M* $LiPF_6$ in DMC). Electrodes were completely Li^+-extracted before testing lithiation rates.

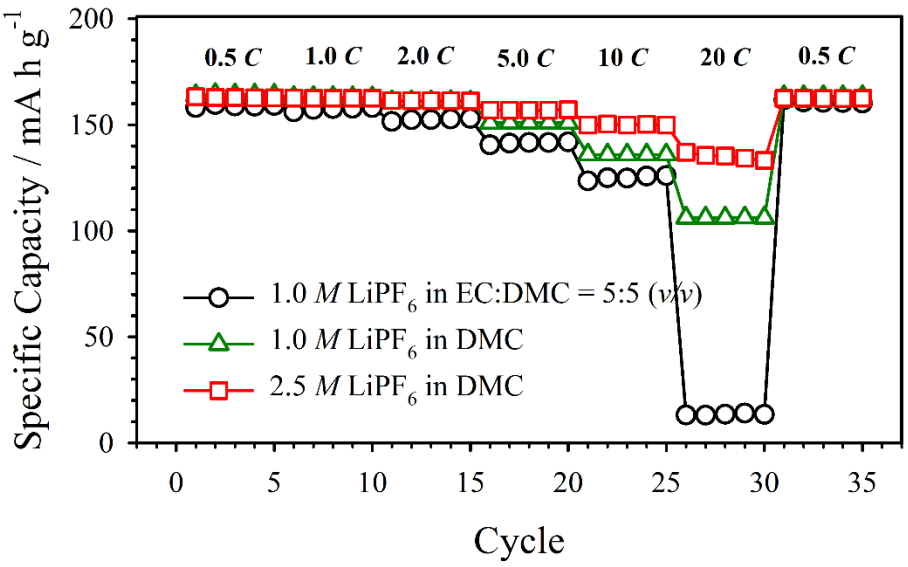

Figure 48. Rate performances of LTO electrode for the 1.0 *M* $LiPF_6$ in EC:DMC = 5:5 (*v*/*v*)), 1.0 *M* $LiPF_6$ in DMC, and the highly concentrated electrolyte (2.5 *M* $LiPF_6$ in DMC). All Li^+ ions are extracted before testing lithiation rates.

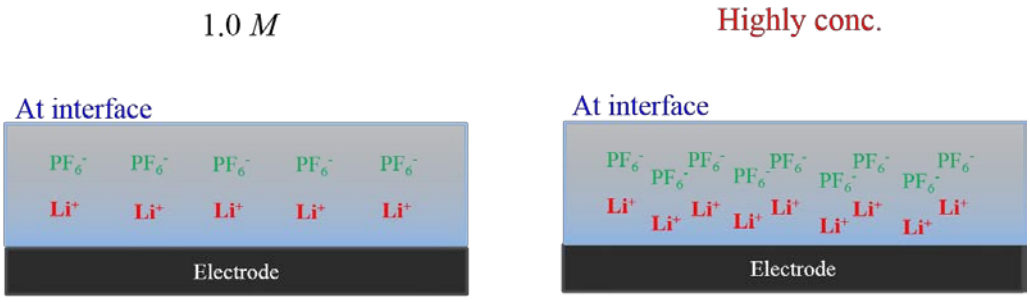

Figure 49. Diagram of the usual 1.0 *M* of composition and a highly concentrated electrolyte.

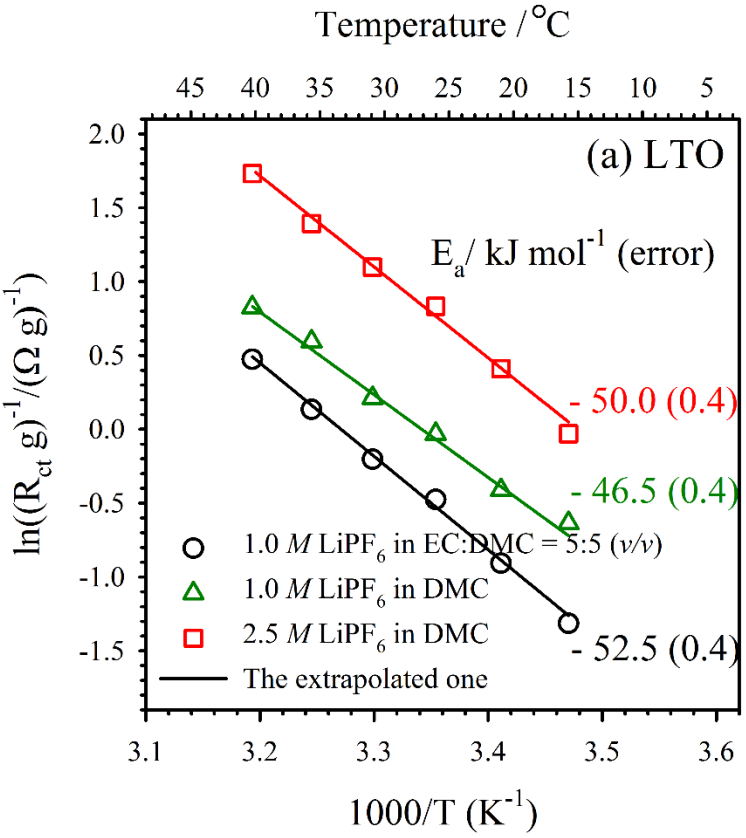

Figure 50. Arrhenius plots for LTO electrode (LTO/LTO symmetric cell) derived from the fitted charge transfer resistances of Ac impedances with temperatures. The correlation between the log scale of the reciprocal charge transfer resistances and the inverse form of temperature are estimated by a linear equation. The used electrolytes, and their corresponding activation energies are indicated in the inset.

this highly concentrated electrolyte effect with the case in LNMO electrode, this highly concentrated electrolyte shows less polarization for Li^+ insertion into any electrodes, it thus improves charging rate for negative electrodes and discharging rate for positive electrodes.

4.2.4. Delithiation rates

During delithiation, however, less polarization is not observed by this highly electrolyte (Fig. 51). This could be accounted for that Li^+ ions in electrolytes are products rather than reactants during delithiation, and thus products Li^+ ions does not lead to the delithiation reaction for the LNMO, and LTO electrodes. As explained above in the previous paragraph, electrochemical reaction rate depends on surface concentration of reactant. The resulting rate performances are exhibited in Fig. 52. Unlike Li^+ ion insertion, delithiation rates are similar regardless of any of the three electrolytes. Comparing Fig. 52a and 52b, delithiation is more influenced by Li^+-inserted electrodes, which are reactants during delithiation, than by the lithium ion concentration of electrolytes (reaction product). Even for the same spinel structure, Li^+ ions are easily extracted from the LTO electrode (Fig. 52b), but difficult to be done from the LNMO electrode (Fig. 52a). Fast discharging is possible in LTO electrodes by using any electrolytes, however, fast

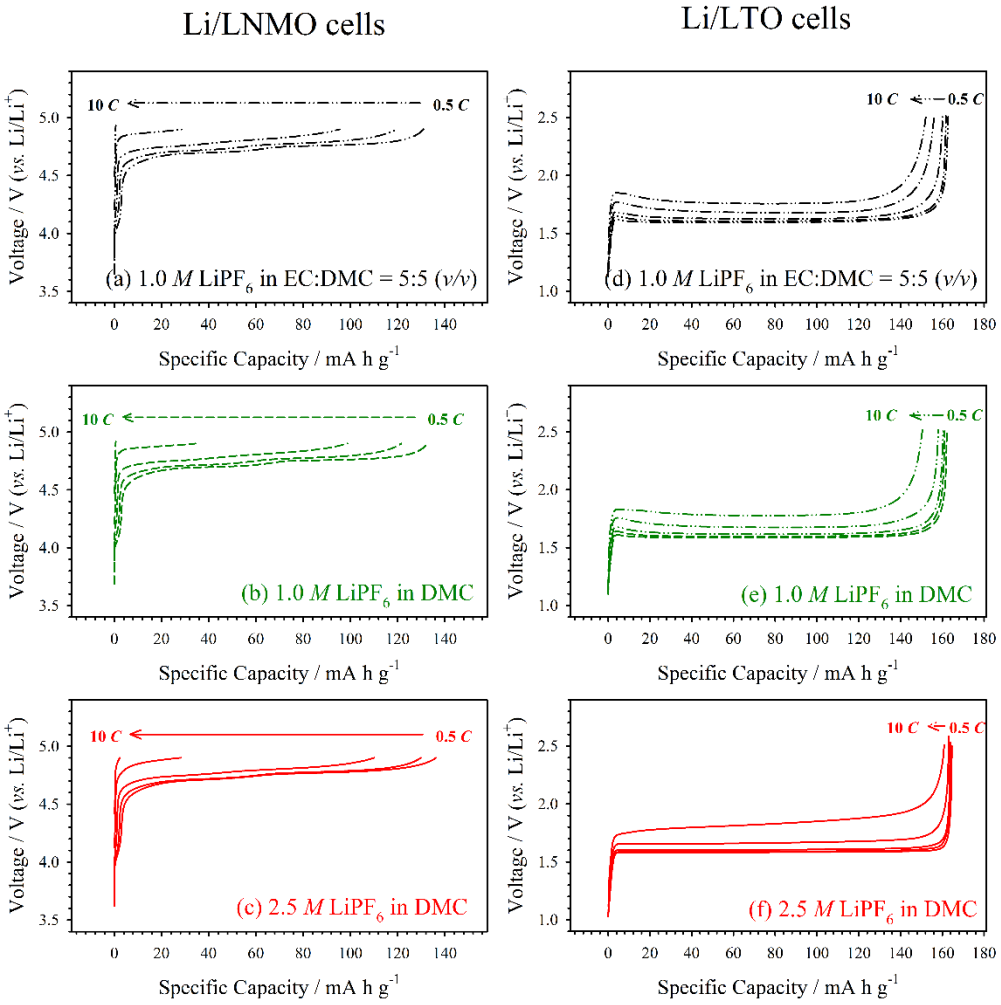

Figure 51. The galvanostatic delithiation voltage profiles for Li/LNMO and Li/LTO cells with electrolytes compositions. (a) (b); a conventional composition (1.0 *M* $LiPF_6$ in EC:DMC = 5:5 (*v*/*v*)), (c) (d); 1.0 *M* $LiPF_6$ in DMC, and (e) (f); the highly concentrated electrolyte (2.5 *M* $LiPF_6$ in DMC). Electrodes were completely Li^+-inserted before testing delithiation rates. The left data are for the Li/LNMO cells and the right one are for the Li/LTO cells.

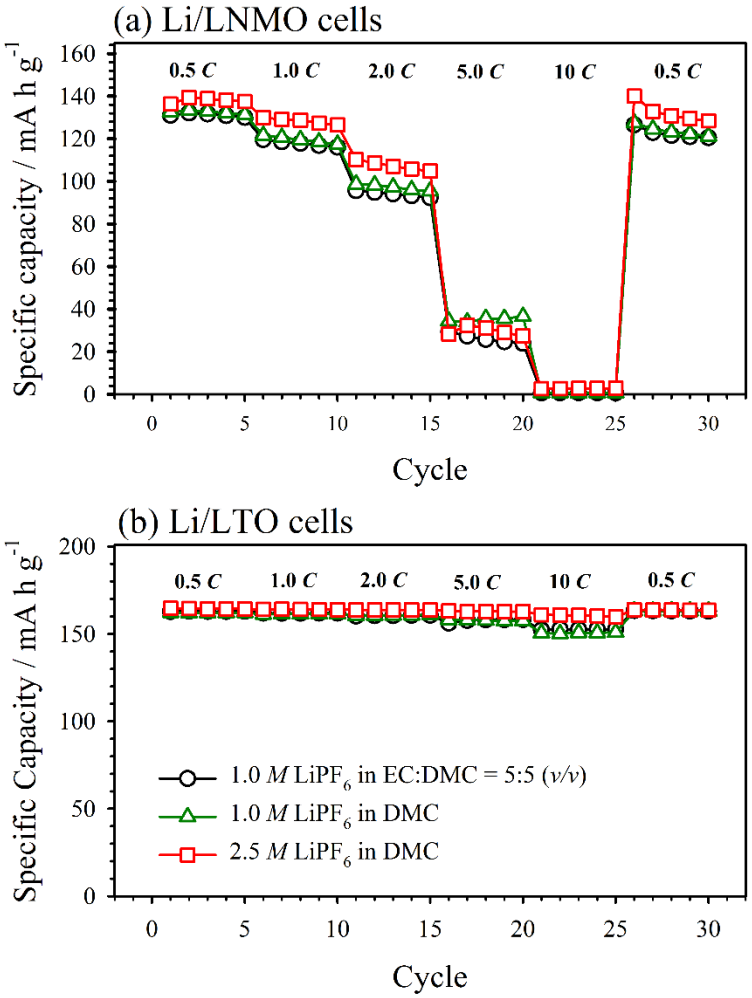

Figure 52. Rate performances of Li/LNMO and Li/LTO cells for the 1.0 *M* $LiPF_6$ in EC:DMC = 5:5 (*v/v*)), 1.0 *M* $LiPF_6$ in DMC, and the highly concentrated electrolyte (2.5 *M* $LiPF_6$ in DMC). All Li^+ ions are inserted before testing delithiation rates. (a); Li/LNMO cells, (b); Li/LTO cells.

charging is not allowed in LNMO electrodes. This would be due to the binding energy difference of lithium toward to oxygen and transition metal for the LNMO and LTO electrodes in the spinel structure.

4.2.5. Fast discharging in full-cell

Finally, we examined fast charging/discharging rates in a real full-cell (Fig. 53). During charging, Li^+ ions are extracted from positive electrodes and inserted into negative electrodes. As above-explained in Fig. 48 and 52a, Li^+ ions are fast inserted into LTO electrode, however, difficult to be extracted from LNMO positive electrode, and thus which indicates that this highly concentrated electrolyte would not improve charging rate in LTO/LNMO full-cells (Fig. 53ab). The LNMO electrodes limits to realize fast charging in a real full-cell (Fig. 52a). In contrast, fast discharging is accomplished by using this highly concentrated electrolyte. As above-explained in Fig. 44 and 52b, a highly concentrated electrolyte enables fast lithiation into LNMO electrode, and Li^+ ions are easily extracted from the spinel-type of LTO electrodes regardless of electrolyte compositions. This supports that LTO electrode is appropriate for the counter electrode of the LNMO positive electrode for fast discharging in a real full-cell. Due to the easy delithiation characteristic of LTO electrode, the highly concentrated

electrolyte delivers 100 mA h g^{-1} (calculated from LNMO) of capacity even at 10 *C* of rate in the LTO/LNMO full-cell. The 2.5 *M* $LiPF_6$ in DMC composition preserves polarization increment at high *C*-rate during discharging (Fig. 53cd), as long as Li^+ ion extraction is not limited from the counter negative electrode (Fig. 52b). It is thus that this highly concentrated electrolyte can be applied to high-power applications need for fast discharging: for example, EVs. In addition, if we find and use a positive electrode capable of easy Li^+ extraction, fast charging could also be achieved by this highly concentrated electrolyte in a real full-cell.

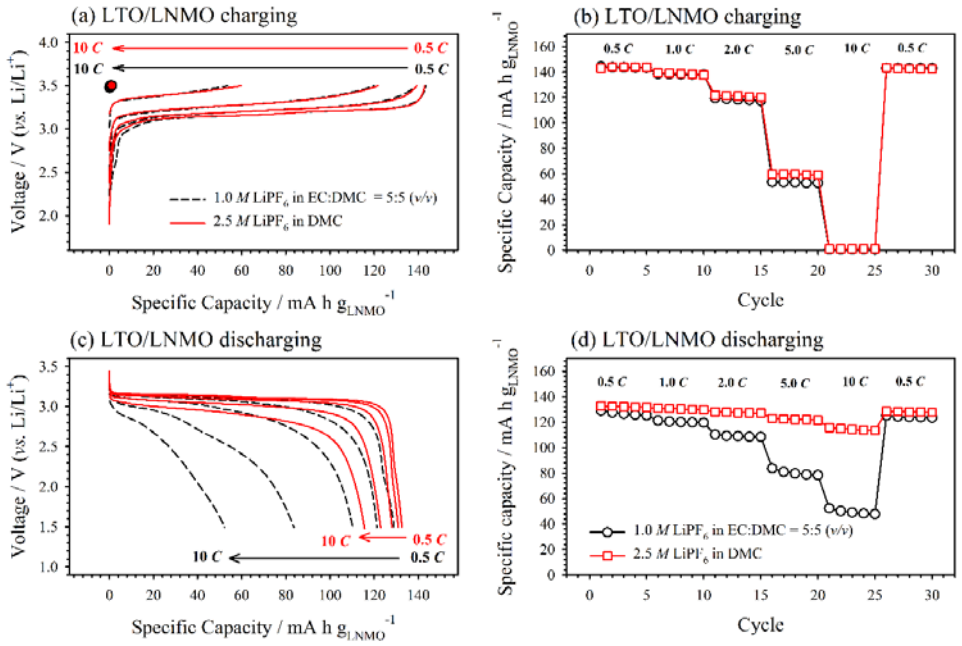

Figure 53. The charging and discharging voltage profiles and its resulting rate performances for LTO/LNMO full-cells with 1.0 *M* $LiPF_6$ in EC:DMC = 5:5 (*v/v*) and 2.5 *M* $LiPF_6$ in DMC. Before testing rate performances, SOC of each full-cell was controlled to 0 (a, b) or 100 (c, d).

5. CONCLUSIONS

The ultimate objectives of my Ph. D course are identification for the ion transport properties of the surface film on a high-voltage positive electrode (e.g, LNMO) and improvement for a series of resistances correlated with the interfaces by being based on the observed properties. During these works, it was found that the surface film on LNMO electrode is permeable and has low Li^+ ion concentration, while the SEI on graphite electrode is highly passivating and has rich Li^+ ion concentration. Based on these findings, a highly concentrated electrolyte is employed to overcome resistances at interfaces. The remarkable features are found and obtained as follows:

Ⅰ. The surface film on positive electrodes are deposited much thinner than SEI on negative electrodes when lithium-ion cells are charged, however, ionic conductivity of films is much poorer than that of SEI. The poorer ionic conductivity per unit thickness of films indicates that their components are different from that of SEI, and thus the resulting Li^+ ion transport properties are different between films and SEI.

Ⅱ. When electrochemical charging, carbonates solvents are electro-oxidatively decomposed to generate cations, which are further polymerized to a some degrees and contain salt anion due to charge balance. Resultantly, the salt anion-contained organic layer is formed on the LNMO electrode. In contrast, carbonates solvents

and salt anion are electro-reductively decomposed to generate anions, which are precipitated with Li^+ ion by ionic interaction. As a result, SEI consists of the bilayers, which are the upper porous organic layer and the bottom compact inorganic layer. The surface film on LNMO is similar with the upper porous organic layer in SEI except for the terminal position: the surface film on LNMO electrode; salt anion, SEI; Li^+ ion

Ⅲ. The electrolyte components are immersed just the upper organic layer in SEI, however, they soak totally the organic layer on LNMO electrode. All electrolyte components involving ions and solvents pass into this organic layer on positive electrodes. Due to this feature, the surface film could be named to “Solid Permeable Interface (SPI)”, which is previously referred by Kristina Edstr ò m and her colleagues. The redox probe, nickel (Ⅱ)-cyclam, approaches the nearest region onto the LNMO surface, where electron tunneling is appreciable. This easy accessible property of electrolyte to the LNMO electrode explains that the continual electrolyte oxidation and its concomitant SPI deposition are one of the major deteriorations for the high-voltage LNMO positive electrodes.

Ⅳ. Ion transport properties for the surface film on LNMO electrode are also influenced by this permeability. Ionic conductivity of a solution medium is determined by free ion concentration and ion mobility. When free ion concentration and ion mobility of electrolytes change, the ionic conductivity of the SPI also changes with the solution conductivity, even though the same surface film

components are deposited on the LNMO electrode. Ion transport of the SPI is influenced by the ion transport of the co-assembled electrolytes.

Ⅴ. The poor ionic conductivity of the SPI than that of SEI, which is accounted for by the less population of Li^+ ion in the solid structure. The less accumulation of Li^+ ions is also responsible for the large charge transfer reaction for the SPI/LNMO interface as well as the surface film conductivity. Considering with the permeable property, highly Li^+-concentrated electrolytes lead to decrease charge transfer resistance into the LNMO electrode. However, the simply concentrated electrolyte cause much poor ionic conductivity by its viscosity increase, and to concomitant larger surface film resistance in the SPI.

Ⅵ. In order to solve the viscosity issue, a highly concentrated electrolyte is organized in a less viscous carbonate solvent. For example, even though the DMC solvent is much less dissociable medium than the EC-mixed composition, the Li^+-concentrated DMC involves larger Li^+ ions involving free ion, ion pair, and aggregates than the usual 1.0 M of the EC-mixed composition. This leads to much favorable charge transfer reaction rate by increasing reactant: Li^+ ion. Additionally, DMC solvent exhibits less coordinating toward to Li^+ ion than EC, which additionally help to desolvation process from electrolytes to electrodes. This much improved charge transfer reaction exhibits fast Li^+ insertion rates during galvanostatic lithiation for the LNMO electrode.

Ⅶ. Combining with LTO electrode, which enables fast Li^+ extraction, this highly concentrated electrolyte also accomplishes fast Li^+-insertion into LNMO electrode. This highly concentrated electrolyte realizes fast discharging in a LTO/LNMO real-full cell. This could be applied to high-power application such as EVs.

REFERENCES

[1] J.B. Goodenough, K.-S. Park, Journal of the American Chemical Society, 135 (2013) 1167-1176.

[2] C.M. Julien, A. Mauger, Ionics, 19 (2013) 951-988.

[3] S. Patoux, L. Daniel, C. Bourbon, H. Lignier, C. Pagano, F. Le Cras, S. Jouanneau, S. Martinet, Journal of Power Sources, 189 (2009) 344-352.

[4] R. Santhanam, B. Rambabu, Journal of Power Sources, 195 (2010) 5442-5451.

[5] A. Kraytsberg, Y. Ein-Eli, Advanced Energy Materials, 2 (2012) 922-939.

[6] Y. Wei, K.-B. Kim, G. Chen, Electrochimica Acta, 51 (2006) 3365-3373.

[7] J.B. Goodenough, Y. Kim, Journal of Power Sources, 196 (2011) 6688-6694.

[8] L. Yang, B. Ravdel, B.L. Lucht, Electrochemical and Solid-State Letters, 13 (2010) A95-A97.

[9] T. Yoon, D. Kim, K.H. Park, H. Park, S. Jurng, J. Jang, J.H. Ryu, J.J. Kim, S.M. Oh, Journal of The Electrochemical Society, 161 (2014) A519-A523.

[10] V.S. Bryantsev, M. Blanco, The Journal of Physical Chemistry Letters, 2 (2011) 379-383.

[11] M. Gauthier, T.J. Carney, A. Grimaud, L. Giordano, N. Pour, H.-H. Chang, D.P. Fenning, S.F. Lux, O. Paschos, C. Bauer, F. Maglia, S. Lupart, P. Lamp, Y. Shao-Horn, The Journal of Physical Chemistry Letters, 6 (2015) 4653-4672.

[12] D. Aurbach, K. Gamolsky, B. Markovsky, G. Salitra, Y. Gofer, U. Heider, R. Oesten,

M. Schmidt, Journal of The Electrochemical Society, 147 (2000) 1322-1331.

[13] M. Moshkovich, M. Cojocaru, H.E. Gottlieb, D. Aurbach, Journal of Electroanalytical Chemistry, 497 (2001) 84-96.

[14] J. Vetter, P. Novák, M.R. Wagner, C. Veit, K.C. Möller, J.O. Besenhard, M. Winter, M. Wohlfahrt-Mehrens, C. Vogler, A. Hammouche, Journal of Power Sources, 147 (2005) 269-281.

[15] S.F. Lux, I.T. Lucas, E. Pollak, S. Passerini, M. Winter, R. Kostecki, Electrochemistry Communications, 14 (2012) 47-50.

[16] D. Becker, G. Cherkashinin, R. Hausbrand, W. Jaegermann, The Journal of Physical Chemistry C, 118 (2014) 962-967.

[17] R. Hausbrand, D. Becker, W. Jaegermann, Progress in Solid State Chemistry, 42 (2014) 175-183.

[18] K. Xu, A. von Cresce, Journal of Materials Chemistry, 21 (2011) 9849-9864.

[19] J.R. Dahn, Physical Review B, 44 (1991) 9170-9177.

[20] Z.X. Shu, R.S. McMillan, J.J. Murray, Journal of The Electrochemical Society, 140 (1993) 922-927.

[21] R. Imhof, P. Novák, Journal of The Electrochemical Society, 145 (1998) 1081-1087.

[22] E. Peled, Journal of The Electrochemical Society, 126 (1979) 2047-2051.

[23] E. Peled, D. Golodnitsky, G. Ardel, Journal of The Electrochemical Society, 144 (1997) L208-L210.

[24] K. Edström, M. Herstedt, D.P. Abraham, Journal of Power Sources, 153 (2006) 380-384.

[25] A.v. Cresce, S.M. Russell, D.R. Baker, K.J. Gaskell, K. Xu, Nano Letters, 14 (2014) 1405-1412.

[26] P. Lu, S.J. Harris, Electrochemistry Communications, 13 (2011) 1035-1037.

[27] S. Shi, P. Lu, Z. Liu, Y. Qi, L.G. Hector, H. Li, S.J. Harris, Journal of the American Chemical Society, 134 (2012) 15476-15487.

[28] K. Edström, T. Gustafsson, J.O. Thomas, Electrochimica Acta, 50 (2004) 397-403.

[29] S. Malmgren, K. Ciosek, M. Hahlin, T. Gustafsson, M. Gorgoi, H. Rensmo, K. Edström, Electrochimica Acta, 97 (2013) 23-32.

[30] 오승모, 전기화학, 2판 ed., 자유아카데미, 경기도 파주, 2010.

[31] A.J. Bard, L.R. Faulkner, Electrochemical Methode: Fundamentals and Application, 2nd edition ed., John Wiley & Sons, Inc., 2001.

[32] J.O.M. Bockris, A.K.N. Reddy, Modern Electrochemistry, second ed., Plenum Press, 1998.

[33] Y. Marcus, Ion solvation, JOHN WILEY & SONS LIMITED, Britain, 1985.

[34] G.A. Mabbott, Journal of Chemical Education, 60 (1983) 697.

[35] T.R. Jow, K. Xu, O. Borodin, M. Ue, Electrolytes for Lithium and Lithium-Ion Batteries, Springer, 2014.

[36] K. Xu, Chemical Reviews, 104 (2004) 4303-4418.

[37] 박정기, 강기석, 김동원, 김성수, 김재국, 도칠훈, 박홍규, 송승완, 이상영, 이성만, 이영기, 이용민, 이창우, 한규승, 홍영식, Principles and applications of Lithium secondary batteries, 홍릉과학출판사, 2010.

[38] G.H. Newman, R.W. Francis, L.H. Gaines, B.M.L. Rao, Journal of The

Electrochemical Society, 127 (1980) 2025-2027.

[39] J. Kim, J.G. Lee, H.-s. Kim, T.J. Lee, H. Park, J.H. Ryu, S.M. Oh, Journal of The Electrochemical Society, 164 (2017) A2418-A2425.

[40] J.T. Dudley, D.P. Wilkinson, G. Thomas, R. LeVae, S. Woo, H. Blom, C. Horvath, M.W. Juzkow, B. Denis, P. Juric, P. Aghakian, J.R. Dahn, Journal of Power Sources, 35 (1991) 59-82.

[41] H. Yang, K. Kwon, T.M. Devine, J.W. Evans, Journal of The Electrochemical Society, 147 (2000) 4399-4407.

[42] H. Arai, K. Sato, Y. Orikasa, H. Murayama, I. Takahashi, Y. Koyama, Y. Uchimoto, Z. Ogumi, Journal of Materials Chemistry A, 1 (2013) 10442-10449.

[43] T.J. Lee, J.B. Lee, T. Yoon, D. Kim, O.B. Chae, J. Jung, J. Soon, J.H. Ryu, J.J. Kim, S.M. Oh, Journal of The Electrochemical Society, 163 (2016) A898-A903.

[44] T. Yoon, S. Park, J. Mun, J.H. Ryu, W. Choi, Y.-S. Kang, J.-H. Park, S.M. Oh, Journal of Power Sources, 215 (2012) 312-316.

[45] J. Soon, T.J. Lee, H.-s. Kim, J. Jung, J.H. Ryu, S.M. Oh, Journal of The Electrochemical Society, 164 (2017) A2677-A2682.

[46] J. Mun, T. Yim, K. Park, J.H. Ryu, Y.G. Kim, S.M. Oh, Journal of The Electrochemical Society, 158 (2011) A453-A457.

[47] K. Takahashi, M. Saitoh, M. Sano, M. Fujita, K. Kifune, Journal of The Electrochemical Society, 151 (2004) A173-A177.

[48] J. Cabana, M. Casas-Cabanas, F.O. Omenya, N.A. Chernova, D.L. Zeng, M.S. Whittingham, C.P. Grey, Chemistry of Materials, 24 (2012) 2952-2964.

[49] J.H. Kim, S.T. Myung, C.S. Yoon, S.G. Kang, Y.K. Sun, Chemistry of Materials, 16 (2004) 906-914.

[50] E.-S. Lee, K.-W. Nam, E. Hu, A. Manthiram, Chemistry of Materials, 24 (2012) 3610-3620.

[51] J. Xiao, X. Chen, P.V. Sushko, M.L. Sushko, L. Kovarik, J. Feng, Z. Deng, J. Zheng, G.L. Graff, Z. Nie, D. Choi, J. Liu, J.-G. Zhang, M.S. Whittingham, Advanced Materials, 24 (2012) 2109-2116.

[52] Y. Chen, Y. Sun, X. Huang, Computational Materials Science, 115 (2016) 109-116.

[53] L. Wang, H. Li, X. Huang, E. Baudrin, Solid State Ionics, 193 (2011) 32-38.

[54] J.-H. Kim, A. Huq, M. Chi, N.P.W. Pieczonka, E. Lee, C.A. Bridges, M.M. Tessema, A. Manthiram, K.A. Persson, B.R. Powell, Chemistry of Materials, 26 (2014) 4377-4386.

[55] H. Lipson, A.R. Stokes, Proceedings of The Royal Society A, 181 (1942).

[56] H. Shi, J. Barker, M.Y. Saïdi, R. Koksbang, L. Morris, Journal of Power Sources, 68 (1997) 291-295.

[57] Y. Qi, H. Guo, L.G. Hector, A. Timmons, Journal of The Electrochemical Society, 157 (2010) A558-A566.

[58] T.J. Lee, J.B. Lee, T. Yoon, H. Park, S. Jurng, D. Kim, J. Jung, J. Soon, J.H. Ryu, K.T. Lee, S.M. Oh, Journal of The Electrochemical Society, 164 (2017) A1887-A1892.

[59] S. Jurng, S. Park, T. Yoon, H.-s. Kim, H. Jeong, J.H. Ryu, J.J. Kim, S.M. Oh, Journal of The Electrochemical Society, 163 (2016) A1798-A1804.

[60] S. Jurng, H.-s. Kim, J.G. Lee, J.H. Ryu, S.M. Oh, Journal of The Electrochemical Society, 163 (2016) A223-A228.

[61] S. Chae, J.B. Lee, J.G. Lee, T.-j. Lee, J. Soon, J.H. Ryu, J.S. Lee, S.M. Oh, Journal of Power Sources, 370 (2017) 131-137.

[62] Y. Domi, M. Ochida, S. Tsubouchi, H. Nakagawa, T. Yamanaka, T. Doi, T. Abe, Z. Ogumi, The Journal of Physical Chemistry C, 115 (2011) 25484-25489.

[63] K. Kanamura, S. Shiraishi, H. Takezawa, Z.-i. Takehara, Chemistry of Materials, 9 (1997) 1797-1804.

[64] J. Jung, J. Jang, O.B. Chae, T. Yoon, J.H. Ryu, S.M. Oh, Journal of Power Sources, 287 (2015) 359-362.

[65] L. Aldon, P. Kubiak, M. Womes, J.C. Jumas, J. Olivier-Fourcade, J.L. Tirado, J.I. Corredor, C. Pérez Vicente, Chemistry of Materials, 16 (2004) 5721-5725.

[66] C. Kim, N.S. Norberg, C.T. Alexander, R. Kostecki, J. Cabana, Advanced Functional Materials, 23 (2013) 1214-1222.

[67] M. Kitta, T. Akita, S. Tanaka, M. Kohyama, Journal of Power Sources, 257 (2014) 120-125.

[68] T. Doi, Y. Iriyama, T. Abe, Z. Ogumi, Analytical Chemistry, 77 (2005) 1696-1700.

[69] I.A. Leonidov, O.N. Leonidova, L.A. Perelyaeva, R.F. Samigullina, S.A. Kovyazina, M.V. Patrakeev, Physics of the Solid State, 45 (2003) 2183-2188.

[70] O. Dolotko, A. Senyshyn, M.J. Mühlbauer, H. Boysen, M. Monchak, H. Ehrenberg, Solid State Sciences, 36 (2014) 101-106.

[71] Y.-J. Hao, Q.-Y. Lai, J.-Z. Lu, X.-Y. Ji, Ionics, 13 (2007) 369-373.

[72] J.-F. Colin, V. Godbole, P. Novák, Electrochemistry Communications, 12 (2010) 804-807.

[73] R.A. Huggins, Advanced Batteries: Materials Science Aspects, Springer, Boston, 2009.

[74] D. Li, H. Zhou, Materials Today, 17 (2014) 451-463.

[75] W. Zhu, D. Liu, J. Trottier, P. Hovington, C. Gagnon, A. Guerfi, K. Zaghib, A. Mauger, H. Groult, C.M. Julien, ECS Transactions, 58 (2014) 35-40.

[76] K. Ariyoshi, Y. Iwakoshi, N. Nakayama, T. Ohzuku, Journal of The Electrochemical Society, 151 (2004) A296-A303.

[77] H. Park, T. Yoon, Y. Kim, J.G. Lee, J. Kim, H.-s. Kim, J.H. Ryu, J.J. Kim, S.M. Oh, Journal of The Electrochemical Society, 162 (2015) A892-A896.

[78] H. Park, T. Yoon, J. Mun, J.H. Ryu, J.J. Kim, S.M. Oh, Journal of The Electrochemical Society, 160 (2013) A1539-A1543.

[79] S.S. Zhang, Journal of Power Sources, 162 (2006) 1379-1394.

[80] M.D. Levi, D. Aurbach, The Journal of Physical Chemistry B, 101 (1997) 4630-4640.

[81] C. Wang, A.J. Appleby, F.E. Little, Electrochimica Acta, 46 (2001) 1793-1813.

[82] M.S. Ding, K. Xu, S.S. Zhang, K. Amine, G.L. Henriksen, T.R. Jow, Journal of The Electrochemical Society, 148 (2001) A1196-A1204.

[83] C. Gabrielli, M. Keddam, R. Torresi, Journal of The Electrochemical Society, 138 (1991) 2657-2660.

[84] D.A. Buttry, M.D. Ward, Chemical Reviews, 92 (1992) 1355-1379.

[85] D.S. Viswanath, T.K. Ghosh, D.H.L. Prasad, N.V.K. Dutt, K.Y. Rani, Viscosity of Liquids, Springer, Netherland, 2007.

[86] M.D. Levi, G. Salitra, B. Markovsky, H. Teller, D. Aurbach, U. Heider, L. Heider, Journal of The Electrochemical Society, 146 (1999) 1279-1289.

[87] D. Aurbach, M.D. Levi, E. Levi, Solid State Ionics, 179 (2008) 742-751.

[88] S. Zhang, M.S. Ding, K. Xu, J. Allen, T.R. Jow, Electrochemical and Solid-State Letters, 4 (2001) A206-A208.

[89] C.H. Chen, J. Liu, K. Amine, Journal of Power Sources, 96 (2001) 321-328.

[90] M. Dollé, F. Orsini, A.S. Gozdz, J.-M. Tarascon, Journal of The Electrochemical Society, 148 (2001) A851-A857.

[91] J.F. Browning, L. Baggetto, K.L. Jungjohann, Y. Wang, W.E. Tenhaeff, J.K. Keum, D.L. Wood, G.M. Veith, ACS Applied Materials & Interfaces, 6 (2014) 18569-18576.

[92] P. Lu, C. Li, E.W. Schneider, S.J. Harris, The Journal of Physical Chemistry C, 118 (2014) 896-903.

[93] W.F.S. John F. Moulder, Peter E. Sobol, Kenneth D. Bomben, Handbook of X-ray Photoelectron Spectroscopy, Physical Electronics, Inc., 1995.

[94] A.M. Andersson, A. Henningson, H. Siegbahn, U. Jansson, K. Edström, Journal of Power Sources, 119–121 (2003) 522-527.

[95] R. Dedryvère, S. Laruelle, S. Grugeon, L. Gireaud, J.-M. Tarascon, D. Gonbeau, Journal of The Electrochemical Society, 152 (2005) A689-A696.

[96] P. Niehoff, S. Passerini, M. Winter, Langmuir, 29 (2013) 5806-5816.

[97] R. Dedryvère, L. Gireaud, S. Grugeon, S. Laruelle, J.M. Tarascon, D. Gonbeau, The Journal of Physical Chemistry B, 109 (2005) 15868-15875.

[98] Y.-C. Lu, A.N. Mansour, N. Yabuuchi, Y. Shao-Horn, Chemistry of Materials, 21 (2009) 4408-4424.

[99] S. Ivanova, E. Zhecheva, R. Stoyanova, D. Nihtianova, S. Wegner, P. Tzvetkova, S. Simova, The Journal of Physical Chemistry C, 115 (2011) 25170-25182.

[100] J. Zheng, X. Wu, Y. Yang, Electrochimica Acta, 105 (2013) 200-208.

[101] K. Xu, Y. Lam, S.S. Zhang, T.R. Jow, T.B. Curtis, The Journal of Physical Chemistry C, 111 (2007) 7411-7421.

[102] K. Xu, A. von Cresce, U. Lee, Langmuir, 26 (2010) 11538-11543.

[103] K. Xu, Chemical Reviews, 114 (2014) 11503-11618.

[104] S.-D. Han, S.-H. Yun, O. Borodin, D.M. Seo, R.D. Sommer, V.G. Young, W.A. Henderson, The Journal of Physical Chemistry C, 119 (2015) 8492-8500.

[105] R. Aroca, M. Nazri, G.A. Nazri, A.J. Camargo, M. Trsic, Journal of Solution Chemistry, 29 (2000) 1047-1060.

[106] B. Fortunato, P. Mirone, G. Fini, Spectrochimica Acta Part A: Molecular Spectroscopy, 27 (1971) 1917-1927.

[107] B. Klassen, R. Aroca, M. Nazri, G.A. Nazri, The Journal of Physical Chemistry B, 102 (1998) 4795-4801.

[108] Y. Yamada, K. Furukawa, K. Sodeyama, K. Kikuchi, M. Yaegashi, Y. Tateyama, A. Yamada, Journal of the American Chemical Society, 136 (2014) 5039-5046.

[109] Y. Yamada, C.H. Chiang, K. Sodeyama, J. Wang, Y. Tateyama, A. Yamada,

ChemElectroChem, 2 (2015) 1687-1694.

[110] J. Wang, Y. Yamada, K. Sodeyama, C.H. Chiang, Y. Tateyama, A. Yamada, Nat Commun, 7 (2016).

[111] Y. Yamada, M. Yaegashi, T. Abe, A. Yamada, Chemical Communications, 49 (2013) 11194-11196.

[112] Y. Yamada, A. Yamada, Journal of The Electrochemical Society, 162 (2015) A2406-A2423.

[113] O. Borodin, G.D. Smith, The Journal of Physical Chemistry B, 113 (2009) 1763-1776.

[114] T. Abe, H. Fukuda, Y. Iriyama, Z. Ogumi, Journal of The Electrochemical Society, 151 (2004) A1120-A1123.

[115] T. Abe, M. Ohtsuka, F. Sagane, Y. Iriyama, Z. Ogumi, Journal of The Electrochemical Society, 151 (2004) A1950-A1953.

[116] T. Abe, F. Sagane, M. Ohtsuka, Y. Iriyama, Z. Ogumi, Journal of The Electrochemical Society, 152 (2005) A2151-A2154.

[117] P. Atkins, J.d. Paula, Elements of Physical Chemistry, fifth edition ed., W. H. Freeman and Company New York, 2009.

[118] P. Atkins, L. Jones, Chemical principles, 4th edition ed., W. H. Freeman and Company, 2008.

[119] P.L. Huston, Chemical Kinetics and Reaction Dynamics, International edition ed., McGraw-Hill, 2001

국문 초록

$LiNi_{0.5}Mn_{1.5}O_4$ 양극 피막의 이온 전달 특성

이 태 진

서울대학교 대학원

화학생물공학부

리튬 이차전지 고전압 양극은 에너지 밀도와 출력을 모두 높일 수 있어, 상용화가 검토되고 있다. 그러나, 현재 주로 사용하고 있는 유기 전해질은 고전압 영역에서 전기화학적으로 분해되어 양극 표면에 계면을 형성하여, 높은 저항을 야기시킨다. 전극의 계면은 그 자체로서의 저항 뿐만 아니라, 전극의 가역 반응과 속도를 결정하는 중요한 요소이다. 그렇기 때문에, 양극 계면의 이온 이동 특성을 이해하고, 이를 바탕으로 그 저항 요인을 극복할 수 있는 방법을 연구하는 것은 중요한 가치를 지닌다.

양극 계면의 물리적 특성이 어떠한지에 대해서는 현재까지 많은 연구가 이루어지지 않았다. 반면, 음극 계면은 그 특성에 관하여 비교적 많은 부분이 밝혀

져 있다. 따라서, 이번 연구에서는 음극 계면의 특성을 기준으로, 양극 계면의 특성을 이해하고자 하였다. 음극 계면은 첫 사이클에 보호 능력이 우수한 계면을 형성하고, 리튬 이온만 자신의 고체상을 통해서 활물질까지 전달한다. 그러나, 양극 계면은 음극 계면과 다르게 우수한 보호 능력이 없고, 투과성이 있으며, 따라서, 리튬 이온은 고체상을 통한 전도가 아니라, 액체 전해질의 투과성에 의해 전달된다는 것을 밝혀내게 되었다. 또한, 이 투과성은 양극에 계면이 생성된다 할지라도, 계면의 보호 능력 결함으로 인해 전해질이 전극 표면까지 도달하게 되므로, 고전압에 노출될 때 지속적인 전해질 부반응을 일으키게 되고, 이것이 고전압 양극의 주요 퇴화 원인 중 하나라는 것을 밝혀내었다.

두 번째는 계면/전극 사이에서 전하 전달 저항에 영향을 끼칠 수 있는 원인을 확인하고, 이 저항을 극복할 수 있는 방법에 관하여 연구하였다. 고전압 양극 계면에서는 음극 계면과 다르게 그 표면에 리튬 이온이 조밀하게 집적되지 않는 현상을 관찰하였다. 전극 표면의 산화/환원 종의 농도는 전하 전달 반응 속도를 결정할 수 있는 요인중의 하나인데, 리튬 이차전지 산화/환원 반응의 매개체인 리튬 이온의 농도가 전하 전달 저항에 어떠한 영향을 주는지를 세밀하게 살펴보았다. 전극 표면의 리튬 이온 농도가 전하 전달 저항에 영향을 준다라는 사실을 확인하였고, 이러한 현상과 앞서 투과성을 함께 고려하여 고농도 전해질을 설계하여 전하 전달 반응을 개선시켜보고자 하였다. 저점도 용매

를 사용한 고농도 전해질은 전하 전달 저항을 개선하여, 리튬 삽입 속도를 개선하므로, 고율의 율속 조건에서도 더 많은 리튬 이온을 전해질로부터 전극 활물질까지 전달할 수 있다. 이러한 특성을 실제 완전지에서도 구현해 보고자 하였다. 이 때, 상대 전극의 선정이 중요한 문제로 떠오르는데, 리튬이 빨르게 탈리 될 수 있는 물질로 선정해 주어야, 리튬 삽입시 상대 전극에서 산화 반응이 빠르게 일어나 속도 제한을 만들지 않는다. 이러한 점을 고려하여, 완전지를 설계하고, 고농도 전해질의 고율 특성을 실제 완전지에서도 구현하였다.

키워드: 리튬 이온 전지, Solid electrolyte interphase (SEI), Solid Permeable Interface (SPI), 이온 전도도, 고농도 전해질, 전하 전달 반응

학 번: 2014-30295